Nonlinear unsteady disturbances generated by the interaction of free-stream vorticity with a laminar boundary layer

Elena Marensi

A Thesis submitted for the degree of Doctor of Philosophy

Department of Mechanical Engineering

University of Sheffield

November 2016

CONTENTS

ACKNOWLEDGEMENTS

I would like to thank the Department of Mechanical Engineering at The University of Sheffield and the Institute of High Performance Computing (IHPC) in Singapore for funding this work. This research would have not been possible without the use of the high performance computing facilities of the A*Star Computational Resource Centre.

Undertaking this Ph.D. has been an exciting challenge and life-changing experience for me. This thesis is the result of my full dedication and of the contribution of a number of people who in one way or another have helped me through this difficult journey.

Most of all, I wish to express my special appreciation and gratitude to my supervisor Dr. Pierre Ricco. He has been an unfailing and patient guide, a source of inspiration and motivation, a pillar of strength and an excellent example of a passionate and high-level scientist. Thank you for unwaveringly believing in me and forming me as a researcher, your teachings and advice are a precious baggage that will always accompany me. My heartfelt thanks are reserved to Prof. Xuesong Wu for his constant support during these years and insightful discussions. I am indebted to Xuesong for giving me the opportunity to spend one month in Tianjin University to work with him and some of his colleagues from the fluid mechanics group. I would like to acknowledge the Mechanics department of Tianjin University for the warm hospitality and the financial support. During my attachment period at IHPC in Singapore, I could rely on the continuous help of my advisor Dr. Vinh-Tan who I sincerely thank. I am particularly grateful to

him for providing me a powerful workstation, which greatly facilitated my work in Singapore, and for his crucial suggestions on the computation of the outer flow. I would also like to thank Dr. Daniel Wise for his invaluable help with Latex and Linux, and my Ph.D. fellows Claudia and Eva for interesting discussions on our projects and for the friendship and fun we shared in and outside the office. I wish you all the best with your theses.

I presented part of this thesis at the IUTAM-ABCM 8th Symposium on Laminar Turbulent Transition, Rio de Janeiro, Brazil, in September 2014. The financial support of the University of Sheffield (Learned Societies Fund) and of the IOP Institute of Physics (Research Student Conference Fund and C R Barber Trust) are kindly acknowledged. Further results were recently presented at the 24th International Congress of Applied Mechanics in Montréal, Canada, in August 2016. My contribution to the conference was made possible thanks to the allowance provided by the A*Star-Sheffield Research Attachment Programme (ARAP) and, partly, thanks to the travel grant offered by the congress organization.

This dream of mine would have remained unfulfilled without the encouragement and unconditional support of my parents Elisabetta and Lorenzo, my sister Silvia and Dan, my love.

LIST OF PUBLICATIONS AND CONFERENCES

Publications

2016 Marensi, E., Ricco, P. & Wu, X. Nonlinear unsteady streaks engendered by the interaction of free-stream vorticity with a compressible boundary layer, *Submitted to JFM (revised)*

2015 Marensi, E., Ricco, P. & Wu, X. Nonlinear response of a compressible boundary layer to free-stream vortical disturbances, *Procedia IUTAM* 14, 105–114.

International conferences (oral presentation)

2014 Marensi, E., Ricco, P. & Wu, X. Nonlinear response of a compressible boundary layer to free-stream vortical disturbances, IUTAM-ABCM Symposium on Laminar Turbulent Transition, Rio de Janeiro, 8th-12th Sept.

2016 Marensi, E., Ricco, P. & Wu, X. Effect of medium-intensity free-stream vorticity on a compressible boundary layer, International Congress of Theoretical and Applied Mechanics (ICTAM), Montreal, 21st-26th Aug.

ABSTRACT

As a contribution towards understanding the impact of free-stream perturbations on laminar-to-turbulent boundary layer transition, we calculate the signature of unsteady disturbances engendered by the interaction of free-stream vortical fluctuations with a laminar boundary layer over a flat and a curved plate. We concentrate on low-frequency perturbations which, in the case of a flat plate, induce strong streamwise-elongated components of the boundary-layer signature, known as Klebanoff modes or streaks. In boundary layers over suitably curved concave walls, Klebanoff modes are expected to develop into Görtler vortices. The generation and nonlinear evolution of the induced perturbations, which acquire an $\mathcal{O}(1)$ magnitude, are described on a self-consistent and first-principle basis using the mathematical framework of the nonlinear unsteady boundary-region equations (NUBREs), subject to appropriate upstream and far-field boundary conditions.

The nonlinear response of a compressible flat-plate boundary layer to free-stream vorticity is investigated first. The problem is governed by the compressible NUBREs, which are derived herein for the first time. The free-stream flow is studied by including the boundary-layer displacement effect and the solution is matched asymptotically with the boundary-layer flow. The nonlinear interactions inside the boundary layer drive an unsteady two-dimensional flow of acoustic nature in the outer inviscid region through the displacement effect. Analytical solutions are derived by exploiting the well-known analogy with the flow over a thin oscillating airfoil, which is used herein for the first time to study unsteady boundary layers. In the subsonic regime the perturbation is felt from the plate in all directions, while at supersonic speeds the disturbance only propagates within the dihedron defined by the Mach line. Numerical computations are performed for carefully chosen parameters that characterize three practical applications: turbomachinery systems, supersonic flight conditions and wind-tunnel experiments. The results show that nonlinearity plays a marked stabilizing role on the velocity and temperature streaks, and this is found to be the case for low-disturbance environment such as flight conditions. Increasing the free-stream Mach number inhibits the kinematic fluctuations but enhances the thermal streaks, relative to the free-stream velocity and temperature respectively, and the overall effect of nonlinearity becomes weaker. An abrupt deviation of the nonlinear solution from the linear one is observed in the case pertaining to a supersonic wind tunnel. Large-amplitude thermal streaks and the strong abrupt stabilizing effect of nonlinearity are two new features of supersonic flows.

In the second part of the thesis, the generation and nonlinear development of unsteady Görtler vortices in an incompressible boundary layer over a concave plate is studied. The centrifugal force caused by the concavity of the wall is included in the incompressible NUBREs. The results show that the stabilizing effect on nonlinearity is significantly intensified in the presence of centrifugal forces. Sufficiently downstream the nonlinear vortices generated at different free-stream turbulence levels Tu are stabilized to the same amplitude, suggesting that the initial intensity of the forcing becomes unimportant. At low Tu the perturbation undergoes a quasi-exponential growth with the growth rate being enhanced for lower frequencies and more curved plates. At higher Tu, in the typical range of turbomachinery applications, the Görtler vortices do not exhibit an exponential growth as nonlinearity saturates rapidly, and the wall curvature does not influence the boundary-layer response. Good quantitative agreement with direct numerical simulations and experimental data is obtained.

1. INTRODUCTION

The transition from a laminar to a turbulent state in boundary layers, although studied for over a century, still represents one of the outstanding unsolved problems in fluid mechanics. A thorough understanding of the physics underlying this phenomenon is of great importance from a fundamental as well as from a practical point of view. The wall-shear stress and heat transfer characteristics change dramatically depending on the flow regime being laminar, transitional or turbulent. Therefore, quantitative prediction and control of transition play a decisive role in determining the operating conditions and performance of flows around high-speed airfoils in a variety of industrial applications. Relevant examples are commercial and high-speed aircraft, space capsule re-entry into the atmosphere and flows around turbine stator vanes or rotor blades.

Boundary-layer transition is known to be significantly influenced by disturbances present in the oncoming stream, which penetrate into the boundary layer and eventually lead to the breakdown of the laminar flow. Such perturbations consist of acoustic (pressure), kinematic (vortical) and entropy (temperature) fluctuations, and may exist independently of each other when they are of sufficiently small amplitude. This work focuses on free-stream vortical disturbances (FSVD), which are characterised by the turbulence intensity Tu (i.e. the-root-mean square value of the turbulent velocity fluctuations), turbulence length scales and turbulence spectrum. The influence of the free-stream turbulence intensity on the transition process was first recognized by Dryden (1955) who observed an upstream shift of the transition location above a smooth flat plate with higher

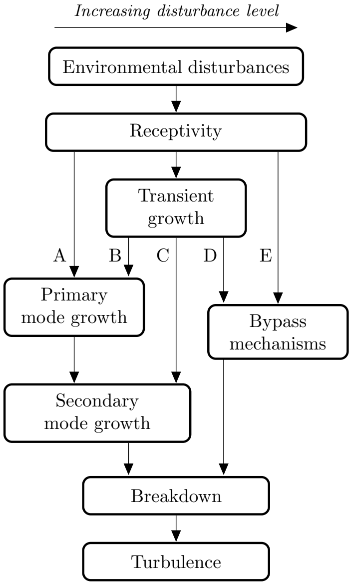

Fig. 1.1: Paths to turbulence in wall layers (Morkovin, 1984).

values of Tu. When Tu is low (Tu<0.1%) transition to turbulence is caused by the growth of viscous instability modes known as Tollmien-Schlichting (T-S) waves. These disturbances are primarily initiated through receptivity, i.e. the mechanism by which external perturbations enter the boundary layer and generate the initial conditions for the laminar breakdown (Reed *et al.*, 2015), slowly grow as they evolve downstream, and may eventually develop strong nonlinear effects causing the breakdown to turbulence through secondary instabilities. This scenario is described by path A of the well-known Morkovin's transition roadmap (Morkovin, 1984) which is reproduced in figure 1.1. For 0.1%<Tu<1%, T-S waves may still be present but, as Tu increases, their characteristics, e.g. wavelength, frequency and grow rate, cannot be predicted by the classical stability theory as they are substantially altered. In boundary layers with free-stream vortical levels of 1% or higher, transition occurs rather early, bypassing the so-called orderly route to turbulence via T-S waves. In this scenario, referred to as bypass transition (paths D and E in figure 1.1), the laminar boundary-layer breakdown is preceded and caused by unsteady streamwise-elongated regions of high and low streamwise velocity. These structures have been referred to as breathing modes (Taylor, 1939) because of their resemblance to a thickening and thinning of the layer, Klebanoff modes (Kendall, 1985) after the experiments of Klebanoff (1971), or laminar streaks.

Another type of boundary-layer disturbance, which may be initiated by free-stream vorticity and may lead to transition, are Görtler vortices. These are counter-rotating longitudinal vortices which arise over a curved surface due to the imbalance between the wall-normal pressure gradient and the centrifugal force. It is well known (see e.g. Liepmann, 1945) that the transition Reynolds number is smaller for concave plates than for flat or convex walls. In the following, the available literature on Klebanoff modes and Görtler vortices will be reviewed.

1.1 Laminar streaks

1.1.1 Experiments and DNS

Experimental works and direct numerical simulations (DNS) have provided an overall picture of bypass transition triggered by free-stream turbulence in the incompressible regime. Detailed measurements of FSVD-induced fluctuations within an incompressible boundary layer were performed, amongst others, by Arnal and Juillen (1978), Kendall (1985), Westin *et al.* (1994), Westin *et al.* (1998), Matsubara and Alfredsson (2001), Fransson *et al.* (2005) and Mandal *et al.* (2010). These experiments confirmed the pioneering findings of Klebanoff (1971) that low-frequency disturbances are dominant in the core of the boundary layer and that the initial growth of the streamwise velocity perturbation is proportional to the laminar boundary-layer thickness. It was also shown in these studies that the streamwise velocity of the induced streaks acquires an amplitude which is much larger than the magnitude of the transverse velocities and

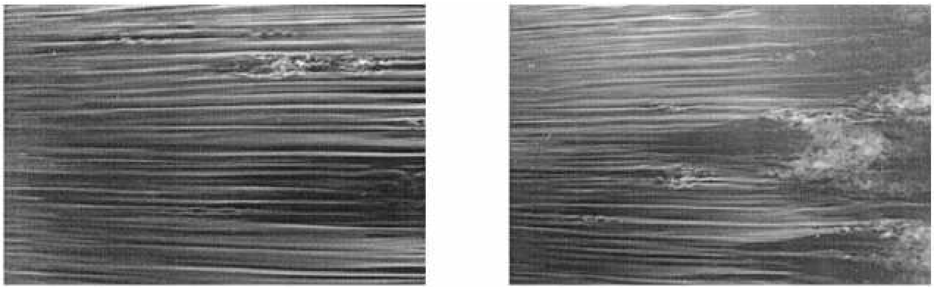

Fig. 1.2: Flow visualisations in the $x - z$ plane of streaks in boundary layers subjected to free-stream disturbances with $Tu = 2.2\%$, $U_\infty = 6$ ms^{-1}(left) and 8 ms^{-1} (right). In the upper part of the left picture, an incipient spot appears, which evolves in a fully developed turbulent spot at the downstream end of the right figure (Matsubara and Alfredsson, 2001).

the intensity of the free-stream perturbations. The smoke flow visualizations of Matsubara and Alfredsson (2001) (figure 1.2) indicate that the streaks undergo a wavy motion of relatively short spanwise wavelength as they grow downstream. This oscillatory meandering motion precedes the breakdown into turbulent spots or patches, which grow in size and merge until the turbulent flow is fully developed. Matsubara and Alfredsson (2001) observed that the spanwise scale of the streaks decreases downstream and approaches the boundary-layer thickness, while the streamwise length scale of the streaky structures increases in the downstream direction.

The experimental observations were complemented by numerical simulations of bypass transition in incompressible boundary layers. The first DNS of transition in a boundary layer subject to free-stream turbulence was carried out by Rai and Moin (1993). The computational inlet was located well upstream of a sharp leading edge to calculate the evolution of grid turbulence impinging on the plate. Other DNS using realistic free-stream disturbances were performed by Nagarajan *et al.* (2007), Ovchinnikov *et al.* (2008) and Brinkerhoff and Yaras (2015). The entire entrainment process of free-stream disturbances into the boundary layer is described correctly in these studies. However, the required extended domain results in extremely long computational times and renders this approach unsuitable for systematic parametric analyses. To avoid these computationally expensive calculations, other DNS studies (e.g. Jacobs and Durbin, 2001; Brandt *et al.*, 2004; Zaki and Durbin, 2005) use inflow conditions synthesized through the continuous modes of the Orr-Sommerfield (O-S) and Squire equations. The validity of this practice will be discussed in the next session. As observed in the experiments, Jacobs and Durbin (2001) showed that the boundary layer act as a filter for broadband free-stream vorticity, thus allowing the low-frequency components of the disturbance to penetrate into the core of the boundary layer while high-frequency fluctuations remain confined in the boundary-layer outer edge (i.e. 'shear sheltering'). Low-speed fluid lifted from the wall form 'backward jets' (Wu *et al.*, 1999) in the upper part of the boundary layer. The jets are distorted and destabilized by high-frequency non-penetrating components and undergo an inflectional type of instability which results in the inception of turbulent spots (Zaki and Durbin, 2005). Brandt *et al.* (2004) confirmed that breakdown into turbulent spots occurs on isolated streaks where strong shear triggers local instabilities. The transition is driven by sinuous-like and varicose-like instabilities, the former being related to the spanwise shear, the latter to the wall-normal shear.

The role of Klebanoff modes in the process of laminar-to-turbulence transition was investigated vis DNS by Fasel (2002). Streaks were generated by artificial volume forces and interacted with a two-dimensional T-S wave forced through a suction/blowing slot at the wall. The low-frequency high-amplitude Klebanoff modes were found to stabilize the seeded two-dimensional T-S wave. The interaction also excited three-dimensional wave packets which were found to undergo an intense downstream amplification and eventually breakdown into turbulent spots.

Despite its importance in high-speed aircraft design and turbomachinery applications, the literature available on bypass transition in compressible flows is more limited than for incompressible flows. Laufer (1954) was among the firsts to carry out experiments on vortical free-stream disturbances in the high-speed regime. He observed that in relatively low-Mach number flows (M_∞<2.5, where M_∞ is the free-stream Mach number) transition is promoted as the amplitude of vortical fluctuations increases, while for M_∞>2.5 the transition Reynolds number is hardly influenced by the amplitude of vortical fluctuations. The author suggested that acoustic disturbances might be dominant in the free stream for high Mach numbers. Hot-wire measurements by Laufer (1961) showed that the sound intensity in the wind tunnel increases approximately as M_∞^4. It was revealed that this intense sound field is radiated by the turbulent shear layers on the wind-tunnel walls.

Other experiments (Pate and Schueler, 1969; Kendall, 1967) confirmed that at high speeds the transition behavior is dominated by the tunnel noise. Transition may occur earlier in laboratory experiments than in flight conditions because of the enhanced level of tunnel noise (Schneider, 2001). This discrepancy prevents the direct use of laboratory data for high-speed vehicle design (Stainback, 1971). Kendall (1975) carried out experiments on supersonic boundary layer subject to high-intensity free-stream fluctuations. For M_∞ ranging from 3 to 5.6 the boundary layer was forced by acoustic disturbances with an increasing degree of correlation between the free-stream fluctuations and those in the boundary layer. Some phenomena were observed, such as the broadband amplification and the influence of free-stream turbulence, which could not be explained with classical linear instability theory (Mack, 1975, 1984). Part of the data showed agreement with Mack's modified stability theory (Mack, 1975) which accounts for the effect of incident sound waves on the boundary layer. In the Mach number range of 1.6 to 2.2, a low degree of correlation between free stream and boundary layer fluctuations was found, thereby suggesting that other types of disturbances, beside the tunnel sound, may be at play. Demetriades (1989) considered a Mach-3 boundary layer for which instability phenomena different from those predicted by the classical linear theory may occur. Transition was found to be driven by disturbances growing at all frequencies well before the departure of the velocity profiles from the Blasius solution was detected.

A Mach-3 boundary layer was also investigated by Graziosi and Brown (2002) whose experiments were carried out with relatively low-intensity free-stream fluctuations. Despite the low-disturbance level, free-stream disturbances of acoustic nature were measured in the test section. In the area around the leading edge, the interaction of free-stream acoustic perturbations with the boundary layer generated mass-flux oscillations within the boundary layer which could be several times larger than the free-stream disturbances. Downstream of the leading edge, the boundary-layer fluctuations were found to be primarily of low frequency, with most of the energy concentrated at frequencies below the so-called Mack first-mode family (Mack, 1984). The growth of these modes appeared not to be consistent with the classical linear stability theory. It could be linked instead to the results of Mack's forcing theory (Mack, 1975). Further downstream, higher frequencies components were found, whose nonlinear development was connected to the appearance of spikes in the time traces of the fluctuating hot-wire voltage. At the late stage of transition, the spikes merged near the plate surface and the time traces became chaotic. Interestingly, the authors noticed that the time interval between spikes matched the time scale of the low-frequency fluctuations. They hypothesized that transition breakdown and nonlinearities onset could be driven by these forced acoustic disturbances.

Although most of the experimental studies in the last few decades have focussed on acoustic disturbances, it should be recognized that more attention needs to be devoted to vortical disturbances. As speculated by Kendall (1975), at low speeds the tunnel sound might be less effective than other types of disturbances, such as the vortical fluctuations. In flight conditions vortical disturbances are the main source of perturbation influencing transition, while acoustic modes are weak and only become relevant at locations affected by the noise radiated by the engine.

Mayer *et al.* (2011) performed DNS of the downstream development of a pair of oblique instability waves in a supersonic flat-plate boundary layer. They confirmed that the oblique-wave breakdown mechanism proposed by Chang and Malik (1994) may be the dominant route to transition in supersonic flows. In this scenario, a wave vortex triad consisting of two oblique modes amplify linearly and interact nonlinearly to generate a steady streamwise vortex mode. Typical structures for the early stages of oblique breakdown were found to be predominantly longitudinal with regions of high shear. In the late stage of transition, the lifted up tips of these structures finally break down into small-scale structures leading to fully developed turbulent flow. They showed that transition in supersonic two-dimensional boundary layers can be initiated by very low free-stream turbulence intensity (abbreviated as FSTI hereinafter and equivalently referred to as Tu), e.g. less than 0.01%, which explains the practical relevance of the oblique-breakdown mechanism for quiet environment such as free flight. Joo and Durbin (2012) carried out DNS of the transition initiated by discrete instability modes and continuous vortical modes in a Mach 4.5 boundary layer. As in Jacobs and Durbin (2001) and Zaki and Durbin (2005), their approach consisted of specifying the inflow conditions in terms of a superposition of the continuous spectra of the Orr-Sommerfield and Squire operators. An approximate decoupling technique was employed to avoid the strong coupling between the free-stream disturbances in the compressible regime which was causing ‘unphysically’ large vorticity and entropy continuous modes to appear in the free stream. A discrete unstable Mack second mode was shown to lead to streak breakdown and, when combined with a vortical continuous mode, it caused earlier transition.

Free-stream disturbances may interact with the boundary layer when other types of external disturbances, such as surface roughness and wall transpiration, are also at play. A DNS study on the receptivity of a supersonic boundary layer to free-stream acoustic and vortical perturbations in the presence of surface step excrescences was performed by Sescu *et al.* (2016). The boundary layer was also perturbed by two-dimensional wall transpiration imposed upstream of the step. The results confirmed that two-dimensional roughness elements act to stabilize high-speed boundary layers, thus delaying the onset of transition.

1.1.2 Theoretical works

Transient optimal-growth theory

Significant effort in the past fifty years has been addressed to the understanding of the so-called transient growth as a central mechanism of formation and amplification of streaks. This term was coined by Landahl (1980) to indicate the algebraic temporal growth of three-dimensional disturbances with very long or infinite streamwise wavelengths in exactly parallel flows (i.e. plane Poiseuille and Couette flows), followed by and exponential decay (Gustavsson, 1991). Luchini (2000) and Andersson *et al.* (1999) showed that a similar spatial amplification occurs in a spatially broadening boundary layer and extended the transient growth approach to the so-called optimal perturbation theory. The steady three-dimensional disturbances are governed by the steady boundary-layer equations. The initial (upstream) conditions are derived by using the adjoint of the equations to determine the optimal perturbations, i.e. the initial velocity profile leading to maximum growth of the perturbation energy at a pre-selected streamwise location. Free-stream disturbances, the very factor causing bypass transition, are not taken into account in this formulation as the fluctuations are imposed to vanish in the free stream. Furthermore, it is not clear how these optimal perturbations could be physically realized in a laboratory experiment.

Zuccher *et al.* (2006) extended the the optimization technique to the nonlinear regime. They determined the input energy E_0 below which nonlinear interactions are unimportant and found that, by increasing E_0, the wavelength of the most amplified optimal disturbance becomes larger. For small values of the initial energy, the mean velocity profiles at the end of the plate almost coincide with Blasius profile, while for high values of E_0, nonlinear effects become more evident and cause strong distortion of the mean-flow profiles.

As pointed out by Ricco *et al.* (2016) the relationship between the boundary-layer disturbances and the free-stream flow is not established in this approach because the latter is not included in the formulation. As a consequence, the initial conditions cannot be imposed before starting the integration, instead they are calculated as an output of the optimization process.

Orr-Sommerfeld continuous spectrum theory

The Orr-Sommerfeld theory has been extensively used to model the inflow conditions in DNS of bypass transition (e.g. Jacobs and Durbin, 2001; Brandt *et al.*, 2004; Zaki and Durbin, 2005; Joo and Durbin, 2012). Such a practice has been questioned by Dong and Wu (2013) and Wu and Dong (2016), who showed that neglecting nonparallel-flow effects in the boundary layer leads to some non-physical features, namely:

i) A spurious entanglement of Fourier components, that is, any two Fourier components with wall-normal wavenumbers $\pm k_y$ and amplitudes A and B are entangled at infinity and the ratio of their amplitudes $|B/A|$ is fixed by the boundary layer. This behavior is at odds with the physical nature of free-stream vorticity, in which Fourier components should be present independently and the relations among their amplitudes should be fixed by the oncoming flow.

ii) A strong anisotropy of the free-stream velocity field, that is, the streamwise velocity is forced by the presence of the boundary layer to assume a much higher magnitude than that of the transverse velocities in the free stream.

Non-parallelism actually plays a dominant role in the entrainment of free-stream turbulent fluctuations into the boundary layer. Therefore continuous modes cannot be employed to describe how free stream vortical disturbances interact with, and penetrate into, the boundary layer, they are just a 'mathematically entity of a given operator' with no physical meaning (Dong and Wu, 2013).

Goldstein theory

In order to include the interaction between free-stream perturbations and the boundary layer, a rigorous mathematical framework has been developed by Goldstein and co-workers (Goldstein *et al.*, 1992; Goldstein and Leib, 1993; Choudhari, 1996; Goldstein, 1997; Wundrow and Goldstein, 2001). The Goldstein theory is based on the boundary-region equations (Kemp, 1951), which arise in the rigorous asymptotic limit of the Navier-Stokes equations for long-wavelength and low-frequency disturbances. For these perturbations, the streamwise derivatives in the viscous and pressure gradient terms are negligible, while the spanwise viscous diffusion is retained.

The boundary-region equations bear some analogies with the parabolized-stability equations (PSE) as both sets of equations are solved with a marching procedure. The PSE approach has been developed and used to study the evolution of instability modes both in incompressible (see e.g. Bertolotti, 1997) and compressible boundary layers (see e.g. Chang *et al.*, 1991). This methodology is based on the assumption that the base flow varies slowly in the streamwise direction and thus a Wentzel-Kramers-Brillouin (WKB) type of analysis is employed to parabolize the Navier-Stokes equations. The method requires, however, an *ad hoc* iterative procedure to identify a local streamwise wavenumber, and, furthermore, the presence of the streamwise pressure gradient causes some numerical instability due to a residual ellipticity in the equations (Li and Malik, 1996). Neither of these problems occurs in the boundary-region-equation approach because the local streamwise wavenumber tends to zero in the low-frequency asymptotic limit, and the equations are strictly parabolic.

In the limit of small amplitude disturbances or short downstream distance, the boundary-region equations can be linearized about the Blasius solution. Leib *et al.* (1999) used the linearized unsteady boundary-region equations to investigate the response of an incompressible laminar boundary layer to free-stream vortical perturbations of the convected-gust type. The initial and far-field boundary conditions were derived by asymptotic matching of the boundary region equations with the upstream and the edge solutions. Thanks to this rigorous mathematical approach, Leib *et al.* (1999) were able to calculate the streamwise evolution of the boundary-layer streak signature (i.e. the root-mean-square of the streamwise velocity fluctuations) and good agreement with experiments was achieved. Their results show that, at the leading order, the generation and growth of Klebanoff modes in the core of the boundary layer is only due to the transverse components of the free-stream perturbation, while the forcing through the free-stream streamwise velocity is of higher order.

Ricco (2009), by extending the approach of Leib *et al.* (1999) to account for second-order terms of the streak signature, showed that this part of the disturbance, despite being negligible in the core of the boundary layer, becomes of leading order at the outer edge of the boundary layer. The mechanism of formation of these streak fluctuations in the outer portion of the boundary layer involves a balance between the free-stream streamwise velocity and pressure fluctuations. A good agreement with the experimental data of Westin *et al.* (1994) was obtained throughout the entire wall-normal extent of the boundary layer.

Wu and Luo (2003) and Wu and Choudhari (2003) studied the instability of a Blasius boundary layer in the presence of steady and unsteady streaks with a spanwise wavelength much larger than δ. They showed that inviscid instability may occur when the distortion of the Klebanoff modes reaches a certain threshold value. The unsteadiness of the streaks was revealed to be essential for the inviscid instability to be triggered, as later confirmed by Goldstein and Sescu (2008). This shows another limit of the optimal-growth theory which, in contradiction to experiments, predicts the streaks to be completely steady. The linear analysis of Leib *et al.* (1999) was extended by Ricco *et al.* (2011) to include nonlinear effects. Nonlinearity was found to attenuate the amplification of the streaks and to distort the mean-flow profile significantly. A secondary instability analysis was performed on the streaky boundary-layer flow, proving that the streaks may become inviscidly unstable during certain phases of the time modulation.

Ricco and Wu (2007) extended the incompressible analysis by Leib *et al.* (1999) to the compressible case and explained the formation and growth of thermal streaks, which are thought to play a significant role in the secondary instability. Ricco *et al.* (2009, 2013) further studied the influence of wall heat transfer and wall suction, respectively, on the thermal streaks. The boundary-layer signature in the region relatively close to the leading edge corresponds to the inhomogeneous solution forced by the free-stream disturbance. However, Ricco and Wu (2007) also observed that sufficiently downstream exponentially growing disturbances are formed. For high-subsonic and supersonic Mach numbers, the appearance of the amplifying disturbances was in the streamwise region of practical interest. Ricco and Wu (2007) showed that the growing disturbances evolved from the so-called quasi-three-dimensional Lam-Rott eigensolutions (Lam and Rott, 1960), which were excited by the free-stream disturbance, and may be identified as highly oblique low-frequency T-S waves in the Mack first-mode family. Ricco *et al.* (2009) found that wall cooling suppresses streaks and the instability waves are excited.

It should be emphasized that, in contrast to the optimal-growth and Orr-Sommerfeld theories, what we referred to as the boundary-region-equation approach consists of the appropriate initial (upstream) and outer boundary conditions, which correctly describe the entrainment of physically-realizable free-stream disturbances, and includes non-parallel and non-local effects.

1.2 Görtler vortices

A boundary layer over a concave surface is subject to a centrifugal instability with respect to three-dimensional disturbances which leads to the generation and amplification of streamwise-oriented counter-rotating vortices, shown schematically in figure 1.3. Such disturbances are known as Görtler vortices, as their existence was first theoretically predicted by Görtler (1940). The experiments of Liepmann (1945) confirmed Görtler's conclusion that the critical Reynolds number is lower for a concave wall than for a flat plate. Since then, a wealth of investigations on the Görtler instability problem has been developed (refer to Saric (1994) for an exhaustive review), due to the primary role that Görtler vortices play in driving transition in many fluid flows of practical relevance. In supercritical laminar-flow-control airfoils (i.e. wings specially designed to delay the formation of shock waves in the transonic-speed regime), transition to turbulence may be caused by centrifugal instability occurring at the leading and trailing edges of the lower

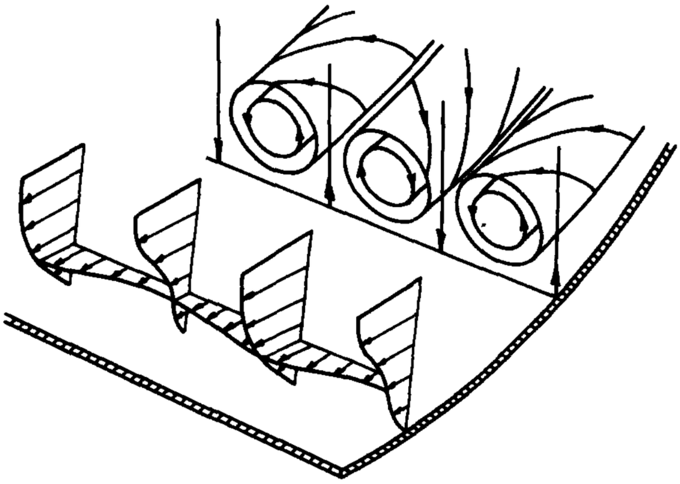

Fig. 1.3: A schematic illustration of Görtler vortices over a concave wall (from Winoto and Crane, 1980).

surface (Mangalam *et al.*, 1985). In turbomachinery, Görtler vortices are found to enhance the heat transfer and the skin friction on the pressure sides of turbine or compressor blades, thus crucially affecting the efficiency of the system (Kim *et al.*, 1992; Volino and Simon, 1995).

A Görtler boundary-layer flow forms over a curved surface due to the presence of a centrifugal force which cannot be balanced by the wall-normal pressure gradient. This underlying mechanism is analogous to that of Taylor vortices, which occur in a flow between two concentric rotating cylinders, or Dean vortices, which appear in fully-developed curved channel flows. However, the theoretical description of Görtler instability is more challenging as it develops in an open domain and it is associated with a growing base flow. As a consequence, nonparallel effects and the influence of external disturbances must be taken into account and an initial-value problem must be solved.

This was rigorously shown by Hall (1983). Until then, all analyses neglected the spatial development of the boundary layer and resorted to a local eigenmode approach. A brief review of the main contributions to the early stage of studies is provided in the following section.

1.2.1 *Early works: the normal-mode approach*

Görtler (1940) considered the temporal stability of the Blasius boundary layer treated as a parallel flow along a curved plate with radius of curvature much larger than boundary-layer thickness. He was able to determine a critical value of the nondimensional parameter G_θ, which now bears his name, above which the flow becomes unstable. The Görtler number represents a measure of the ratio between the centrifugal forces and the viscous and inertial forces. It is usually defined as $G_\theta = R_\theta \sqrt{K}$, where R_θ is the Reynolds number based on the boundary-layer momentum thickness θ and the free-stream velocity and K is the radius of curvature normalized by θ. Hot-wire measurements by Tani (1962) and Tani and Aihara (1969) showed that the vortices hold their spanwise wavelength almost constant as they develop downstream. Additional data were provided by Aihara (1962) and Wortmann (1969) through visualization of the vortex structure.

Improved calculations of Görtler's original formulation were derived by Hämmerlin (1956), who retained the higher-order curvature terms, and Smith (1955), who also included some nonparallel effects and performed a spatial instability analysis rather than a temporal one. Although Smith (1955) considered the correct approximation in the curvature terms, the streamwise gradient of the wall-normal velocity of the base flow was still neglected and the Reynolds number explicitly appeared in the disturbance equations because the same scaling of the perturbation velocity components was employed. Floryan and Saric (1982) derived the first-order approximation to the stability equations of the Görtler problem by introducing two velocity scales, one for the streamwise velocity and one for the crossflow velocities, the former being greater than the latter by an order $\mathcal{O}(R_\theta)$. As previously recognized by Diprima and Stuart (1972), this scaling is necessary to account for the convection of streamwise momentum by weak wall-normal and spanwise velocity components. The disturbance equations derived by Floryan and Saric (1982), which are known as the locally nonparallel stability equations, were written in the optimal coordinate system based on the streamlines and potential lines of the inviscid flowfield over a curved surface. With these optimal coordinates, the zeroth-order approximation of the base flow was shown to correspond to the Blasius flow, an assumption that was not rigorously justified in previous works.

The linear stability equations have often been solved by freezing the base flow at each downstream locations, thus neglecting the nonparallel effects (Floryan and Saric, 1982; Finnis and Brown, 1989; Ragab and Nayfeh, 1981). A normal-mode solution for the disturbance may thus be sought and an eigenvalue system is obtained. Although separation of variables is strictly not permissible because the coefficients of the disturbance equations depend on the streamwise coordinate, Floryan (1991) argued that the normal-mode approach can be interpreted as a local analysis that can be used for engineering purposes. The advantage of the eigenvalue formulation is that a unique neutral curve can, in theory, be produced in the wavenumber-Görtler number plane. Little or no agreement between the different neutral curves predicted with different Görtler instability models was obtained, especially at low spanwise wavenumbers (Herbert, 1976; Floryan and Saric, 1982; Finnis and Brown, 1989; Ragab and Nayfeh, 1981), and, more importantly, the disturbance growth rates were found to differ significantly from experimental data. Floryan and Saric (1982) compared the local analysis neutral curve and the disturbance profile to experimental results by Bippes (1972), Wortmann (1964), Tani (1962) and Tani and Sakagami (1962). The neutral point of Wortmann (1964) was located above its theoretical counterpart. The experimental neutral curve of Bippes (1972) was shifted toward larger wavenumber with respect to that obtained by Floryan and Saric (1982). Finnis and Brown (1997) found that the growth rates measured in the experiments were much lower than those predicted by the linear stability analysis.

As pointed out by Hall (1990), the disagreement between different parallel or quasi-parallel theories was caused by their inconsistency in retaining higher-order curvature effects and some nonparallel effects, while the discrepancies with experiments were due to the parabolic (initial-condition dependent) nature of the problem being unsuitable for eigenvalue description.

1.2.2 The initial-value approach

Hall (1982a,b) showed that the separation-of-variable solution is justifiable only for large values of the Görtler number and, in this limit, a linear and a nonlinear asymptotic theory in the vicinity of the short-wave branch of the neutral curve were developed. The analytic expression of the upper neutral branch derived by Hall (1982a), i.e. $k_z=\mathcal{O}(G_\theta^{1/2})$, where k_z is the spanwise wavenumber of the vortices scaled by the local boundary-layer thickness δ, was found to agree well with previous numerical data for large k_z. Timoshin (1990) analyzed the large-G_θ asymptotic structure of the unstable vortices for different relations between G_θ and k_z. The most unstable regime was identified for $k_z=\mathcal{O}(G_\theta^{2/5})$, while the inviscid mechanism of instability was found to be operational when the spanwise wavelength is comparable with the local boundary-layer thickness. Timoshin (1990) also confirmed the conclusion of Hall (1982b) conclusion that at high Görtler numbers the short wavelength eigensolutions tend to concentrate in an internal viscous layer away from the wall and from the free stream.

Hall (1983) pointed out that if $G_\theta = \mathcal{O}(1)$ and $\lambda_z/\delta = \mathcal{O}(1)$ the normal-mode approach is not tenable and the only appropriate method for analyzing Görtler instability is the numerical integration of the set of parabolic partial differential equations which govern the problem. Hall (1983) solved the linear stability equations by a streamwise marching scheme and showed that the neutral point significantly depends on the location x_0 and on the shape of the specified initial conditions. He showed, for example, that the neutral point can be placed anywhere by simply moving x_0.

The streamwise-integrated solutions and the eigenvalue solutions were compared by Day *et al.* (1990) and Kalburgi *et al.* (1988). The local eigenmode was used as initial condition to the parabolic system. Kalburgi *et al.* (1988) criticized the choice of initial conditions in Hall (1983) and argued that the 'physical' initial condition should be found by solving the eigenvalue problem. As pointed out by Hall (1990), this criticism is unfounded as it resorts to an 'ad hoc' choice of the upstream perturbation and it misses the point that Görtler vortices represent an initial-value problem and not an eigenvalue one. The calculations of Day *et al.* (1990) support the thesis of Hall (1983) that a unique neutral curve is not tenable. Although the results obtained from different initial conditions were found to evolve differently, sufficiently downstream the solutions were shown to be unaffected by the initial conditions and to approach the local eigenvalues. Similar conclusions were drawn by Bottaro and Luchini (1999), who performed a multiple-scale analysis to account for nonparallel effects and found close agreement of the amplification rates computed with streamwise-integrated and local methods at large downstream distances.

1.2.3 The receptivity problem

Because the Görtler instability is an initial-value problem, the receptivity process is of crucial importance. In practical situations where the Görtler instability is bound to be relevant, Görtler vortices can be stimulated by roughness on the wing surface (e.g. in flight conditions), by free-stream vorticity impinging on the leading edge (e.g. in turbomachinery applications), or by any other source of disturbance that sheds streamwise vortices.

Experimental evidence of the influence of upstream and external perturbations was already provided in early measurements by Bippes (1972), Bippes and Görtler (1972), Kottke and Mpourdis (1987), Kottke (1988) and Swearingen and Blackwelder (1983). Bippes (1972) and Bippes and Görtler (1972) performed their experiments in a towing tank, thus at very low free-stream disturbance level. It was found necessary to place a turbulence-generating grid in front of the test section or to introduce small heated wires along the span to visualize the vortices. The measured characteristic wavelength was shown to depend on the nature of the oncoming flow. This was confirmed by low-speed wind tunnel experiments of Swearingen and Blackwelder (1983), who were able to alter the vortex wavelengths by placing strips of tape on the wall plate or by introducing cylinders in the oncoming flow. Kottke and Mpourdis (1987) could not observe Görtler vortices when the screens that act as a source of perturbations were placed sufficiently upstream from the leading edge. By putting the screens ahead of the model and by varying the grid mesh size, Kottke (1988) was able to observe Görtler vortices of longer wavelength with increasing mesh size.

One of the first theoretical study on receptivity of Görtler boundary layers was performed by Hall (1990), who focused on vortices induced by free-stream disturbances encountering the leading edge of the curved wall. The perturbation was in the form of a steady spanwise and wall-normal periodic longitudinal velocity superimposed on the oncoming flow, and the most unstable case occurred for a perturbation with null wall-normal wavenumber, i.e. external disturbances proportional to $\cos k_z z$, where z here is the spanwise coordinate. Bertolotti (1993) employed the parabolized stability equations to examine the generation and development of Görtler vortices driven by surface waviness and wall suction. The streamwise-aligned wall corrugations proved to be an efficient means of vortex generator, with the growth of the vortices being promoted in the presence of spanwise and streamwise periodicity of the surface inhomogeneities. The generation of Görtler vortices by surface imperfections was investigated by Denier *et al.* (1991) and later re-examined by Bassom and Hall (1994) with asymptotic techniques. Denier *et al.* (1991) found that the coupling coefficient, which relates the amplitude of the forcing function to that of the induced vortex, is exponentially small when the forced vortex wavelength is small compared to the boundary-layer thickness. Their analysis showed that wall roughness is an extremely weak generator of short-wavelength Görtler vortices associated with the right branch of the neutral curve. However, in the region where $k_z = \mathcal{O}(G_\theta^{2/5})$ the coupling coefficient of the fastest growing mode was found to be $\mathcal{O}(1)$. Bassom and Hall (1994) focused on the case of $\mathcal{O}(1)$ wavenumber Görtler vortices and considered different forcing functions. In the case of an isolated roughness element, amplification of the vortex system is triggered if the local Görtler number G_x exceeds a certain threshold, while in the case of distributed roughness, unstable vortices are generated irrespectively of G_x. In the review of Bassom and Seddougui (1995), the free-stream disturbance receptivity mechanism examined by Hall (1990) is compared to the roughness receptivity process analyzed by Denier *et al.* (1991) and Bassom and Hall (1994). It is concluded that, whilst the first route is more efficient for small wavelength modes, for $\mathcal{O}(1)$-wavelength modes the boundary layer is most receptive to distributed roughness.

The mechanism of generation of Görtler vortices by free-stream vorticity is of particular relevance to turbomachinery applications because blade surfaces are usually curved and the oncoming flow is characterized by elevated turbulence level. Görtler instability in high turbulence environments was examined by Winoto and Crane (1980) and Leoutsakos and Crane (1990) for a curved water channel, and by Kim *et al.* (1992), Kestoras and Simon (1993), Riley *et al.* (1989) and Volino and Simon (1996, 2000) (refer to Volino and Simon (2000) for a review) for a concave blade surface. Volino and Simon (1995) showed that free-stream turbulence and wall curvature significantly affect the onset and length of transition, and, as a consequence, the skin friction and the wall-heat transfer characteristic. Kim *et al.* (1992) considered two different free-stream turbulence intensities, 0.6 and 8.6%, and were able to detect steady Görtler vortices only in the low turbulence case. At high Tu it was conjectured that unsteady Görtler vortices may form, although their presence could not be confirmed with the experimental techniques used.

The available literature on Görtler instability is mainly devoted to steady vortices because these are the structures which have been primarily studied in the laboratory. The predominance of time-independent vortices in most of the experiments may be explained by a preferential receptivity route in driving these disturbances (Choudhari and Streett, 1990). However, in real transition scenarios, and especially in high turbulence environment characteristic of turbine blades, unsteady Görtler vortices may be at play (Schultz and Volino, 2003). The first experimental study on unsteady Görtler vortices was carried out by Boiko *et al.* (2010b). Controlled vortices were excited by low-frequency time-periodic blowing/suction imposed on the wall. Particular care was devoted to perform the measurements at low disturbance amplitude so that the linearity of the stability problem was guaranteed. The weakly-nonlinear stage of the unsteady Görtler instability was considered by Boiko *et al.* (2010a) and a minimum amplitude of 4-6% of the fundamental mode was found to be necessary for the disturbances to enter the region of nonlinear evolution. Ivanov *et al.* (2011, 2012, 2014) focused on the excitation of controlled unsteady Görtler vortices by surface non-uniformities and free-stream vortices. In Ivanov *et al.* (2014) four possible receptivity mechanisms were analysed, i.e localized scattering of two-dimensional/three-dimensional free-stream vortices by three-dimensional/two-dimensional surface non-uniformities (roughness or vibrations), and distributed scattering of two-dimensional/three-dimensional free-stream vortices by natural three-dimensional/two-dimensional base-flow non-uniformities. Only the latter, i.e. the scattering of longitudinal free-stream vortices by natural two-dimensional non-uniformity of the growing boundary layer, proved to be efficient in generating Görtler vortices.

As for the theoretical and numerical works, more attention has recently been devoted to the subject of receptivity and growth of Görtler vortices, although many aspects still lack of a thorough understanding. The main theoretical frameworks used in the study of laminar streaks over a flat plate, i.e. the optimal-growth approach, the Orr-Sommerfeld theory and the boundary-region equations, are extendible to the analysis of a curved wall. The flaws of the optimal-growth and O-S approaches as compared to Goldstein theory were discussed in the previous section for the case of a flat plate, but the same considerations are valid for a curved wall. Optimal disturbances were employed by Luchini and Bottaro (1998) and Cossu *et al.* (2000) to study the receptivity to wall roughness and free-stream disturbance. Schrader *et al.* (2011) performed a numerical study of the flow over a concave surface subject to streamwise-localized wall roughness and free-stream vortical modes of different frequencies. As in Jacobs and Durbin (2001) and Zaki and Durbin (2005), the latter were modelled as Orr-Sommerfeld and Squire continuous-spectra eigenfunctions and a superimposition of these modes was used to synthesize the inflow condition for spatial direct numerical simulations (DNS) of the transition process. Wu *et al.* (2011) instead employed the boundary-region equation approach to study the initiation and linear development of unsteady Görtler rolls generated by free-stream vorticity. The work of Leib *et al.* (1999) was extended to account for centrifugal effects that arise over a curved wall. The free-stream disturbances enter the boundary layer immediately downstream of the leading edge and trigger streamwise streaks, as in the flat-plate case. When the Görtler number G_λ (based on the spanwise wavelength λ_z of the disturbance) exceeds a critical value, the excited perturbation undergoes an exponential growth and develop into Görtler modes. The growth rate of the induced vortices was found to increase as the frequency decreased, with the steady rolls being most amplified. Wu *et al.* (2011) also performed an asymptotic analysis for $G_\lambda \gg 1$ to identify the distinguished regimes undergone by rolls with fixed spanwise wavelength. Their formulation confirmed the results of Timoshin (1990) and Denier *et al.* (1991) and generalized them to include unsteadiness.

1.2.4 Nonlinear effects and secondary instability

As elucidated by the experimental work of Swearingen and Blackwelder (1987), Görtler vortices themselves do not lead to transition. Instead, elongated low-speed regions are generated between the vortices, as low-momentum fluid is pumped away from the wall. The low-speed streaks are alternated in the spanwise direction by high-speed regions caused by the upwelling of high-momentum fluid. Further downstream, as the nonlinear interactions become more intense, these high-low speed structures develop into a mushroom-shaped distribution. The high-speed regions feature a thinner boundary layer and therefore are more stable, while the low-speed regions create highly distorted velocity profiles with inflectional points in the normal and spanwise directions. Periodic oscillations lead to the breakdown to turbulence. Although this unsteadiness of the vortices was already observed by Bippes (1972), it was the work of Swearingen and Blackwelder (1987) that shed light on the breakdown process through secondary instability. Two types of waviness were identified: sinuous modes, driven by unstable inflectional spanwise profiles, and varicose modes, associated with instability in the inflectional normal profiles. The former was found to be the most preferred mechanism of transition. More recent experiments performed by Tandiono *et al.* (2008, 2013) confirmed the picture provided by Swearingen and Blackwelder (1987) on the transition process of Görtler flows.

Hall (1988) integrated the nonlinear parabolized equations and was able to predict the flow distortion. The nonlinear development of Görtler vortices was also studied by Benmalek and Saric (1994) with a similar approach. After a relatively short linear regime, the disturbance energy was found to saturate. In both studies the wall curvature was chosen to vary with the streamwise distance, while Hall (1990) performed constant-curvature nonlinear calculations and was able to obtain qualitative agreement with the experiments of Swearingen and Blackwelder (1987).

The existence of sinuous and varicose modes was confirmed by numerous secondary instability calculations (e.g. Hall and Horseman, 1991; Yu and Liu, 1994; Li and Malik, 1995), which helped clarify the relative importance of these two types of instability in causing transition. All these calculations were performed for steady Görtler vortices. A temporal DNS of breakdown of Görtler flow was carried out by Liu and Domaradzki (1993). Instability fluctuations were shown to occur first in the spanwise direction and later in the wall-normal direction. In agreement with the experiments of Swearingen and Blackwelder (1987), the spanwise shear was found to play a more important role than the wall-normal shear in triggering transition to turbulence. However, this is not always the case. For sufficiently large wavelengths the varicose modes are dominant. This was demonstrated by the secondary-instability analysis of Li and Malik (1995) and later confirmed in the experiments of Asai *et al.* (2002). Schrader *et al.* (2011) performed a spatial DNS of streamwise developing Görtler vortices initiated by broadband free-stream turbulence. The physical mechanism of boundary-layer transition was found to be similar to that occurring over a flat plate, although in the latter case the flow break downs to turbulence further downstream than in a Görtler flow. The skin-friction coefficient in transitional and turbulent Görtler boundary layers exceeded the level reached by the flat-plate counterpart. This behavior was also observed in the nonlinear calculations of Girgis and Liu (2006), who associated it with the distortion of the primary Görtler modes due to secondary sinuous oscillations.

1.3 Objectives

The aim of this thesis is to investigate the nonlinear response of a laminar boundary layer to free-stream vorticity in different flow regimes and configurations. Of relevance are low-frequency free-stream components which are shown in the experiments to penetrate the most into the core of the boundary layer. The induced perturbation is governed by the boundary-region equations, which retain the non-parallel effects and the spanwise viscous diffusion. In chapter 2, we focus on compressible streaks because in high-speed flows transition occurs more frequently through the bypass route than via the T-S wave growth described by classical stability theory. As in the incompressible case, bypass transition in compressible boundary layers is of relevance for engineering applications, but it is also challenging theoretically because of both the difficult mathematics involved and the complex physical mechanisms at play. As an essential step towards understanding and predicting compressible bypass transition, we formulate a rigorous description of the formation and nonlinear development of the unsteady compressible streaks induced by free-stream vortical fluctuations. Such a mathematical theory for compressible disturbances responsible for bypass transition is still absent. A further goal is to explain the nonlinear interactions between the free-stream flow and the viscous boundary-layer flow, which occur through the displacement effect.

In chapter 3, the effect of the wall curvature is considered in the incompressible regime. The rigorous mathematical formulation of the boundary-region equations is extended to account for the centrifugal force due to the concavity of the wall. The goal of this analysis is to predict the generation of unsteady Görtler vortices by FSVD, their downstream amplification and nonlinear evolution. This problem is of particular relevance in turbomachinery applications, where the onset of transition is significantly affected by the curvature of the blades and the enhanced level of free-stream turbulence (Volino and Simon, 1995). The combination of these two effects leads to the formation of Görtler vortices, whose amplitude is high enough for nonlinear interactions to occur. Although the nonlinear evolution of Görtler vortices has been investigated by a number of researchers (e.g. Hall, 1988; Benmalek and Saric, 1994), all these works are exclusively concerned with steady vortices. The problem of excitation of nonlinear unsteady Görtler vortices by elevated free-stream turbulence is addressed here for the first time. Different physical parameters which may affect the growth of the vortices in realistic scenarios are analysed.

Describing the nonlinear development of the streaks and of the Görtler vortices is an indispensable step for the secondary instability analysis, which, in the compressible case, must account for both the velocity and thermal streaks. A key observation is that, in our methodology the unsteady and three-dimensional base flow generated by the nonlinear interactions inside the boundary layer is constructed by including the forcing of physically-realizable free-stream disturbances. Only in this way, a systematic and physics-based approach suitable for boundary-layer transition prediction (e.g. for correlating the transition Reynolds number with the FSTI) may be developed.

2. NONLINEAR UNSTEADY STREAKS ENGENDERED BY THE INTERACTION OF FREE-STREAM VORTICITY WITH A COMPRESSIBLE BOUNDARY LAYER

This chapter focuses on the nonlinear response of a compressible laminar boundary layer to free-stream vortical disturbances of the convected-gust type. The free-stream turbulence level is assumed to be sufficiently high that the induced boundary-layer streaks acquire an $\mathcal{O}(1)$ amplitude in the region where the boundary-layer thickness becomes comparable with the spanwise wavelength of the disturbance. The previous works by Ricco and Wu (2007) and Ricco *et al.* (2011) are extended to account for both compressibility and nonlinearity. In §2.1, the mathematical formulation and the scalings adopted are presented. In §2.1.1 the free-stream perturbation is described and in §2.1.2 the nonlinear unsteady compressible boundary-region equations are derived. In §2.1.3 the outer-flow solution is obtained and matched with the inner solution in §2.1.4. The numerical procedure to solve the boundary-region problem is outlined in §2.2. The outer-flow velocity and pressure fields are shown in §2.3 for the subsonic and supersonic regimes. In §2.4.1 three different cases are considered, i.e. a turbomachinery flow, a free-flight flow and a supersonic wind-tunnel flow. The relevant results for the unsteady compressible streaks are presented in §2.4.2 and §2.4.3.

2.1 Formulation: scalings and governing equations

An air flow with a mean uniform velocity U_∞^* and constant temperature T_∞^* is considered; hereinafter the symbol * is used to indicate dimensional quantities.

Superimposed on the mean flow are homogeneous, statistically-stationary turbulent vortical fluctuations, which are of the convected-gust type, i.e. passively advected by U^*_∞. The perturbed air flow encounters a semi-infinite smooth flat plate. The oncoming flow is considered isentropic and air is treated as a perfect gas. The speed of sound in the free stream is:

$$a^*_\infty = \sqrt{\gamma \mathcal{R}^* T^*_\infty}, \tag{2.1}$$

where γ=1.4 is the ratio of the specific heats and $\mathcal{R}^*$ is the specific gas constant of air ($\mathcal{R}^*$=287.05 $\mathrm{N\,m\,kg^{-1}K^{-1}}$). The Mach number is defined as

$$M_\infty \equiv \frac{U^*_\infty}{a^*_\infty} = \mathcal{O}(1). \tag{2.2}$$

In the Cartesian coordinate system employed to describe the flow, a point is represented by a position vector $\mathbf{x}^*$=$x^*\mathbf{i} + y^*\mathbf{j} + z^*\mathbf{k}$, where x^*, y^* and z^* define the streamwise, wall-normal and spanwise directions, respectively. The spatial coordinates are non-dimensionalized by a suitable reference length scale λ^*, which we shall specify below. The velocity and temperature reference scales are U^*_∞ and T^*_∞. The fluid properties, such as the density ρ^* and the dynamic viscosity μ^*, are scaled by their respective constant free-stream values, ρ^*_∞ and μ^*_∞. The time t^* and the pressure p^* are non-dimensionalized by λ^*/U^*_∞ and $\rho^*_\infty U^{*2}_\infty$, respectively.

It should be pointed out that in the supersonic regime shocks appear when the aerodynamic body (including a flat plate) has a finite thickness, and that at sufficiently highly Mach numbers, shocks can also arise for the idealized case of a flat plate with zero thickness due to the significant displacement produced near the leading edge by the viscous boundary-layer motion. The presence of a shock may change the boundary-layer instability property if it is sufficiently close to the boundary layer (Chang *et al.*, 1990; Cowley and Hall, 1990). Moreover, when any of three types of perturbations, e.g. a vortical fluctuation, interact with a shock, all three disturbances may appear downstream of the shock (McKenzie and Westphal, 1968). The acoustic and entropy perturbations may influence transition via receptivity mechanisms (Fedorov and Khokhlov, 2003; Zhong and Wang, 2012; Qin and Wu, 2016). In the present case of an infinitely thin flat plate with zero angle of incidence, a large hypersonic Mach number is needed for shock waves to form close to the body. In the literature (e.g. Anderson, 2006), a Mach number range M_∞>8-10 is generally used in this configuration to include the effects of shocks, although a precise lower bound is not provided. The hypersonic regime is not considered in our study (except for one slightly hypersonic Mach number of 6 which will be discussed later) as in this case other effects come at play, such as high-temperature chemical reactions and shock-layer viscous interaction, which are beyond the scope of the thesis. Throughout this chapter, the Mach number is assumed to be relatively moderate (M_∞=2-3 in the supersonic regime), so that shocks are weak and distant from the boundary and their effect is negligible. In this case, the interaction of unsteady disturbances with the shock is decoupled from their subsequent interaction with the boundary layer (Qin and Wu, 2016). The response of the boundary layer to each type of free-stream disturbance downstream of a shock can be analyzed separately.

2.1.1 Free-stream disturbances and scaling

Free-stream turbulence is in general of broadband nature. For simplicity, we consider the case of vortical perturbation consisting of a pair of modes with the same frequency (and thus streamwise wavenumber), but opposite spanwise wavenumber $\pm k_z^*$. In the incompressible analysis of Ricco *et al.* (2011), this choice of free-stream disturbance has led to good quantitative agreement between the theoretical prediction and wind-tunnel experimental data. A similar behavior is expected in the compressible case. The formulation and computation can be extended to realistic free-stream perturbation, which are of broadband nature as was shown by Zhang *et al.* (2011) for incompressible flows.

The velocity field of free-stream convected gusts of the assumed form can be expressed as

$$\mathbf{u}-\mathbf{i}=\epsilon\mathbf{u}_\infty(x-t,y,z)=\epsilon\left(\hat{\mathbf{u}}_+^\infty e^{ik_z z}+\hat{\mathbf{u}}_-^\infty e^{-ik_z z}\right)e^{ik_x(x-t)+ik_y y}+c.c., \tag{2.3}$$

where $\hat{\mathbf{u}}_\pm^\infty=\{\hat{u}_{x,\pm}^\infty,\hat{u}_{y,\pm}^\infty,\hat{u}_{z,\pm}^\infty\}=\mathcal{O}(1)$ is a real vector, $\epsilon\ll1$ is a measure of the free-stream perturbation level, and *c.c.* indicates the complex conjugate. From the continuity equation, it follows that

$$k_x\hat{u}_{x,\pm}^\infty+k_y\hat{u}_{y,\pm}^\infty\pm k_z\hat{u}_{z,\pm}^\infty=0. \tag{2.4}$$

It is appropriate and convenient to take $\lambda^*=1/k_z^*$, so that $k_z=1$. The characteristic Reynolds number is

$$R_\lambda\equiv\frac{U_\infty^*\lambda^*}{\nu_\infty^*}\gg1. \tag{2.5}$$

Only the components of the free-stream disturbance with $k_x\ll1$ are considered as they have been shown in experiments to be the ones that penetrate the most into the core of the boundary layer to induce streaks.

Goldstein (1997) showed that the flow domain can be decomposed into four asymptotic regions (figure 2.1), which are described in the following. Further details are given in Appendix A.

Region I is an inviscid region of dimension $\mathcal{O}(\lambda^*)$ in all three directions located above the boundary layer and around the leading edge of the plate. The disturbances are considered as small perturbations of U_∞^*. The solution is described by Leib *et al.* (1999) for the incompressible case and extended to the compressible regime by Ricco (2006).

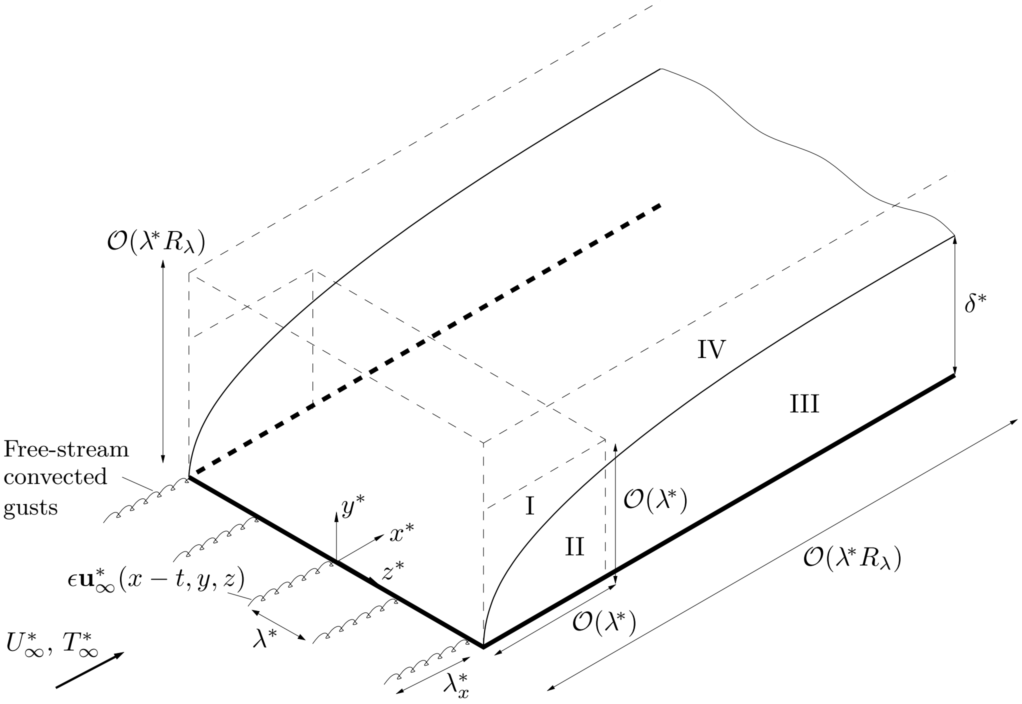

Fig. 2.1: Sketch of the flow configuration representing the asymptotic regions (Leib *et al.*, 1999).

Region II is a viscous region located beneath region I. The flow is governed by the linearized unsteady boundary-layer (LUBL) equations (Gulyaev *et al.*, 1989 and Leib *et al.*, 1999, for the incompressible case, Ricco and Wu, 2007, for the compressible case). The LUBL equations are valid as long as the local boundary-layer thickness δ^* remains smaller than the spanwise length scale λ^*. Since δ^* is related to the streamwise location x^* by $\delta^*{=}\mathcal{O}\left(x^* R_\infty^{-1/2}\right)$, where $R_\infty{=}U^*_\infty x^*/\nu^*_\infty$, it follows that in this region $x^*{\ll}\mathcal{O}(\lambda^* R_\lambda)$ or $x/R_\lambda{\ll}\mathcal{O}(1)$.

According to the result of Leib *et al.* (1999), the velocity perturbation is maximum when $x{=}\mathcal{O}(k_x^{-1})$. The following scaling is thus introduced:

$$\bar{x} = k_x x = \mathcal{O}(1). \tag{2.6}$$

As a measure of the ratio between the local boundary-layer thickness δ^* and the spanwise length scale λ^* at $\bar{x}=\mathcal{O}(1)$, a scaled spanwise wavenumber is defined as

$$\kappa \equiv \frac{1}{\lambda^*}\sqrt{\frac{\lambda_x^* \nu_\infty^*}{2\pi U_\infty^*}} = \frac{k_z}{\sqrt{k_x R_\lambda}}. \qquad (2.7)$$

It thus follows that in region II $k_x \gg \mathcal{O}(R_\lambda^{-1})$, or, equivalently, $\kappa \ll \mathcal{O}(1)$.

Region III is a viscous region where $\delta^*=\mathcal{O}(\lambda^*)$ so that viscous diffusion effects in the spanwise and wall-normal directions are comparable. This occurs at streamwise locations $x^*=\mathcal{O}(\lambda^* R_\lambda)$, which, together with (2.6), leads to $k_x=\mathcal{O}(R_\lambda^{-1})$, or, equivalently, $\kappa=\mathcal{O}(1)$. The perturbations are governed by the unsteady boundary-region equations (Kemp, 1951), which are the limit of the Navier-Stokes equations for low-frequency and streamwise-elongated perturbations, i.e. with the streamwise derivatives neglected in the viscous and pressure-gradient terms. The boundary-region equations are parabolic in the streamwise direction and elliptic in the spanwise direction. As shown by Leib *et al.* (1999), $\mathcal{O}(\epsilon)$ free-stream disturbances can produce $\mathcal{O}(\epsilon/k_x)$ fluctuations of the streamwise velocity component within the boundary layer. Nonlinear effects become of leading order when $\epsilon/k_x=\mathcal{O}(1)$, i.e. when the turbulent Reynolds number

$$r_t \equiv \epsilon R_\lambda = \mathcal{O}(1), \qquad (2.8)$$

since $k_x=\mathcal{O}(R_\lambda^{-1})$.

Region IV is an outer region located above region III. At $\bar{x}=\mathcal{O}(1)$ the outer flow is influenced at the leading order by the displacement effect due to the presence of a thicker viscous layer beneath. In addition to the three-dimensional vortical gust advected from upstream, the disturbance in this region includes a two-dimensional irrotational perturbation induced by the displacement effect. The latter assumes different forms depending on the flow regime.

The focus of the present work is on the last two regions, i.e. region III (the inner region) and IV (the outer region), where the nonlinear effects are important.

2.1.2 The inner region: nonlinear unsteady compressible streaks

In the boundary layer the solution is expressed as the superimposition of the unsteady perturbation on the steady laminar compressible boundary layer. The velocities and temperature of the Blasius flow have the similarity solution (Stewartson, 1964)

$$\{U, V\} = \left\{F'(\eta), \frac{T(\eta_c F' - F)}{\sqrt{2xR_\lambda}}\right\}, \qquad T = T(\eta),$$

where the prime indicates differentiation with respect to the similarity variable η,

$$\eta \equiv \sqrt{\frac{R_\lambda}{2x}} \int_0^y \rho(x, \check{y})\,\mathrm{d}\check{y}, \tag{2.9}$$

and $\eta_c{=}T^{-1}\displaystyle\int_0^\eta T(\check{\eta})\,\mathrm{d}(\check{\eta})$. The procedure to obtain V is described in Appendix B. The x-momentum and the energy equations are:

$$FF'' + \left(\frac{\mu}{T}F''\right)' = 0,$$

$$\left(\frac{\mu T'}{T}\right)' + \mathrm{Pr}FT' + \mathrm{Pr}(\gamma - 1)M_\infty^2 \frac{\mu}{T}F''^2 = 0,$$

where the Prandtl number Pr=0.7. The system is subject to the boundary conditions,

$$F(0) = F'(0) = 0, \qquad T(0) = T_w,$$

$$F' \to 1, \;\; T \to 1 \;\text{ as } \eta \to \infty,$$

where T_w is the imposed wall temperature (isothermal condition). For $\eta{\gg}1$, $F{\to}\bar{\eta}{\equiv}\eta - \beta_c$, where β_c depends on M_∞ (refer to figure B.1). Using the equation of state, the density ρ is given by

$$\rho = \frac{1}{T}. \tag{2.11}$$

The viscosity μ=$\mu(T)$ is assumed to follow a power law,

$$\mu = T^{\omega} \text{ with } \omega = 0.76. \tag{2.12}$$

This relation has been proved to be more appropriate than the linear Chapman law (ω=1) in the Mach number range of interest M_{∞}<4 (Stewartson, 1964).

The total boundary-layer flow is decomposed as the sum of the Blasius flow and the perturbation induced by the free-stream disturbance, namely,

$$\begin{aligned} \{u_{tot}, v_{tot}, w_{tot}, p_{tot}, \tau_{tot}\} = \left\{U, V, 0, -\frac{1}{2}, T\right\} + r_t \Bigg\{ \bar{u}\left(\bar{x}, \eta, z, t\right), \sqrt{\frac{2\bar{x}k_x}{R_\lambda}}\bar{v}\left(\bar{x}, \eta, z, t\right), \\ \frac{k_x}{k_z}\bar{w}\left(\bar{x}, \eta, z, t\right), \frac{k_x}{R_\lambda}\bar{p}\left(\bar{x}, \eta, z, t\right), \bar{\tau}\left(\bar{x}, \eta, z, t\right)\Bigg\}, \end{aligned} \tag{2.13}$$

where τ stands for the temperature. The Blasius flow does not correspond to the mean flow; the latter also consists of the time-independent components generated by the nonlinear interactions, which are included in the perturbation. The scaling (2.8) and equation (2.13) indicate that for low-frequency free-stream disturbances with spanwise wavelength comparable with the local boundary-layer thickness and streamwise wavelength of $\mathcal{O}(\lambda^* R_\lambda)$, the streamwise velocity and the temperature of the induced streaks acquire an amplitude of $\mathcal{O}(\epsilon R_\lambda)$, which is much larger than $\mathcal{O}(\epsilon)$ transverse velocity components (and the intensity of free-stream disturbances). The boundary-layer signature therefore bears all hallmarks of streaks observed in experiments. For the assumed simple composition of free-stream disturbance, the seeded oblique mode pair would be dominant in the earlier stage, and is expected to remain the most significant in the nonlinear stage downstream. However, nonlinear interactions generate harmonics and the mean-flow distortion. The disturbance must be expressed as a Fourier series in time and z,

$$\{\bar{u}, \bar{v}, \bar{w}, \bar{p}, \bar{\tau}\} = \sum_{m,n} \{\hat{u}_{m,n}, \hat{v}_{m,n}, \hat{w}_{m,n}, \hat{p}_{m,n}, \hat{\tau}_{m,n}\} \, e^{imk_x t + ink_z z}, \tag{2.14}$$

where $\{\hat{u}_{m,n}, \hat{v}_{m,n}, \hat{w}_{m,n}, \hat{p}_{m,n}, \hat{\tau}_{m,n}\}$ are functions of $\bar{x}$ and η. Unless otherwise specified, hereinafter the upper and lower limits of the summations are $\pm\infty$. From the reality of the physical quality, the Fourier coefficients are Hermitian,

$$\hat{q}_{-m,-n} = \hat{q}^{\star}_{m,n}, \tag{2.15}$$

where $\hat{q}$ indicates any of $\{\hat{u}, \hat{v}, \hat{w}, \hat{p}, \hat{\tau}\}$ and the * denotes the complex conjugate. The total density is decomposed as $\rho_{tot}=\rho + r_t\bar{\rho}$, where ρ is given by (2.11). Substituting the total flow into the equation of state, one finds

$$\bar{\rho} = \frac{\gamma M_\infty^2 k_x}{T R_\lambda} \bar{p} - \frac{\bar{\tau}}{T^2} - r_t \frac{\bar{\rho}\bar{\tau}}{T}. \tag{2.16}$$

It follows that the total density is:

$$\rho_{tot} = \frac{1}{T} + r_t \left(\frac{\gamma M_\infty^2 k_x}{T R_\lambda} \bar{p} - \frac{\bar{\tau}}{T^2} \right) - r_t^2 \frac{\bar{\rho}\bar{\tau}}{T}. \tag{2.17}$$

The total viscosity is expressed by applying (2.12) to the total flow and by expanding it using the binomial formula as

$$\mu_{tot} = (T + r_t\bar{\tau})^\omega = \sum_{j=0}^{\infty} \frac{(\omega)_j}{j!} T^{\omega - j} r_t^j \bar{\tau}^j = \mu + r_t \mu' \bar{\tau} + r_t^2 \bar{\mu}, \tag{2.18}$$

where $(\omega)_j{=}\omega(\omega-1)(\omega-2)...(\omega-j+1)$, $\mu'{=}\mathrm{d}\mu/\mathrm{d}T$, and $\bar{\mu}$ is the nonlinear part of the viscosity perturbation, which is decomposed as

$$\bar{\mu} = \sum_{m,n} \hat{\mu}_{m,n}(\bar{x},\eta)e^{imk_xt+ink_zz}. \tag{2.19}$$

The nonlinearity of the viscosity comes from the power law exponent $\omega{\neq}1$ and the turbulent Reynolds number $r_t{=}\mathcal{O}(1)$. The nonlinear part $\bar{\mu}$ is null when either(i) $\omega{=}1 \ \ \forall\, r_t$ or (ii) $r_t{=}0 \ \ \forall\omega$ in (2.18). As long as $|r_t\bar{\tau}|{<}1$, which applies to all the cases considered, the series in (2.18) is absolutely convergent.

By inserting (2.13) and (2.14) into the continuity, momentum and energy equations, using (2.17)-(2.19), and taking the limits $k_x{\ll}k_z$, $R_\lambda{\gg}1$ with $k_xR_\lambda{=}\mathcal{O}(1)$, the nonlinear unsteady compressible boundary-region equations are found as follows.

The continuity equation

$$\begin{aligned}&\frac{\eta_c}{2\bar{x}}\frac{T'}{T}\hat{u}_{m,n} + \frac{\partial\hat{u}_{m,n}}{\partial\bar{x}} - \frac{\eta_c}{2\bar{x}}\frac{\partial\hat{u}_{m,n}}{\partial\eta} - \frac{T'}{T^2}\hat{v}_{m,n} + \frac{1}{T}\frac{\partial\hat{v}_{m,n}}{\partial\eta} + in\hat{w}_{m,n}\\ &-\left(\frac{im}{T}+\frac{FT'}{2\bar{x}T^2}\right)\hat{\tau}_{m,n} - \frac{F'}{T}\frac{\partial\hat{\tau}_{m,n}}{\partial\bar{x}} + \frac{F}{2\bar{x}T}\frac{\partial\hat{\tau}_{m,n}}{\partial\eta} = r_t\hat{\mathcal{C}}_{m,n},\end{aligned} \tag{2.20}$$

the x-momentum equation

$$\begin{aligned}&\left(im - \frac{\eta_c}{2\bar{x}}F'' + \kappa^2n^2T\mu\right)\hat{u}_{m,n} + F'\frac{\partial\hat{u}_{m,n}}{\partial\bar{x}} - \frac{1}{2\bar{x}}\left(F + \frac{\mu'T'}{T} - \frac{\mu T'}{T^2}\right)\frac{\partial\hat{u}_{m,n}}{\partial\eta}\\ &-\frac{\mu}{2\bar{x}T}\frac{\partial^2\hat{u}_{m,n}}{\partial\eta^2} + \frac{F''}{T}\hat{v}_{m,n} + \left(\frac{FF''-\mu'F'''-\mu''F''T'}{2\bar{x}T} + \frac{\mu'T'F''}{2\bar{x}T^2}\right)\hat{\tau}_{m,n}\\ &-\frac{\mu'F''}{2\bar{x}T}\frac{\partial\hat{\tau}_{m,n}}{\partial\eta} = r_t\hat{\mathcal{X}}_{m,n},\end{aligned} \tag{2.21}$$

the y-momentum equation

$$\frac{1}{4\bar{x}^2}\left[FT + \eta_c(FT'-TF') - \eta_c^2F''T\right]\hat{u}_{m,n} + \frac{\mu'T'}{3\bar{x}}\frac{\partial\hat{u}_{m,n}}{\partial\bar{x}} - \frac{\mu}{6\bar{x}}\frac{\partial^2\hat{u}_{m,n}}{\partial\eta\partial\bar{x}}$$

$$
\begin{aligned}
&+\frac{1}{12\bar{x}^2}\left(\mu+\eta_c T'\mu'-\frac{\mu T'\eta_c}{T}\right)\frac{\partial \hat{u}_{m,n}}{\partial \eta}+\frac{\eta_c\mu}{12\bar{x}^2}\frac{\partial^2 \hat{u}_{m,n}}{\partial \eta^2}\\
&+\left(im+\frac{\eta_c}{2\bar{x}}F''+\frac{F'}{2\bar{x}}-\frac{FT'}{2\bar{x}T}+\kappa^2n^2\mu T\right)\hat{v}_{m,n}+F'\frac{\partial \hat{v}_{m,n}}{\partial \bar{x}}\\
&-\frac{1}{\bar{x}}\left(\frac{F}{2}+\frac{2\mu'T'}{3T}-\frac{2\mu T'}{3T^2}\right)\frac{\partial \hat{v}_{m,n}}{\partial \eta}-\frac{2\mu}{3\bar{x}T}\frac{\partial^2 \hat{v}_{m,n}}{\partial \eta^2}+in\frac{\mu'T'}{3\bar{x}}\hat{w}_{m,n}-in\frac{\mu}{6\bar{x}}\frac{\partial \hat{w}_{m,n}}{\partial \eta}\\
&+\frac{1}{4\bar{x}^2}\left[\eta_c\left((FF')'-T\left(\frac{\mu'F''}{T}\right)'\right)-FF'-\frac{F^2T'}{T}-\mu'F''+\frac{4}{3}\left(\frac{\mu'T'F}{T}\right)'\right]\hat{\tau}_{m,n}\\
&-\frac{\mu'F''}{2\bar{x}}\frac{\partial \hat{\tau}_{m,n}}{\partial \bar{x}}+\left(\frac{\mu'T'F}{3\bar{x}^2T}-\frac{\eta_c\mu'F''}{4\bar{x}^2}\right)\frac{\partial \hat{\tau}_{m,n}}{\partial \eta}+\frac{1}{2\bar{x}}\frac{\partial \hat{p}_{m,n}}{\partial \eta}=r_t\hat{\mathcal{Y}}_{m,n},
\end{aligned}
\tag{2.22}
$$

the z-momentum equation

$$
\begin{aligned}
&in\kappa^2\frac{\eta_c\mu'T'T}{2\bar{x}}\hat{u}_{m,n}-in\kappa^2\frac{\mu T}{3}\frac{\partial \hat{u}_{m,n}}{\partial \bar{x}}+in\kappa^2\frac{\eta_c\mu T}{6\bar{x}}\frac{\partial \hat{u}_{m,n}}{\partial \eta}-in\kappa^2\mu'T'\hat{v}_{m,m}\\
&-in\kappa^2\frac{\mu}{3}\frac{\partial \hat{v}_{m,n}}{\partial \eta}+\left(im+\frac{4n^2\kappa^2\mu T}{3}\right)\hat{w}_{m,n}+F'\frac{\partial \hat{w}_{m,n}}{\partial \bar{x}}\\
&-\frac{1}{2\bar{x}}\left(F+\frac{\mu'T'}{T}-\frac{\mu T'}{T^2}\right)\frac{\partial \hat{w}_{m,n}}{\partial \eta}-\frac{\mu}{2\bar{x}T}\frac{\partial^2 \hat{w}_{m,n}}{\partial \eta^2}-\frac{in\kappa^2FT'\mu'}{3\bar{x}}\hat{\tau}_{m,n}\\
&+in\kappa^2T\hat{p}_{m,n}=r_t\hat{\mathcal{Z}}_{m,n},
\end{aligned}
\tag{2.23}
$$

the energy equation

$$
\begin{aligned}
&-\frac{\eta_cT'}{2\bar{x}}\hat{u}_{m,n}-\frac{M_\infty^2(\gamma-1)\mu F''}{\bar{x}T}\frac{\partial \hat{u}_{m,n}}{\partial \eta}+\frac{T'}{T}\hat{v}_{m,n}\\
&+\left[im+\frac{FT'}{2\bar{x}T}-\frac{1}{2\mathrm{Pr}\bar{x}}\left(\frac{\mu'T'}{T}\right)'-\frac{M_\infty^2(\gamma-1)\mu'(F'')^2}{2\bar{x}T}+\frac{\mu n^2\kappa^2T}{\mathrm{Pr}}\right]\hat{\tau}_{m,n}\\
&+F'\frac{\partial \hat{\tau}_{m,n}}{\partial \bar{x}}-\frac{1}{2\bar{x}}\left(F+\frac{2\mu'T'}{\mathrm{Pr}T}-\frac{\mu T'}{\mathrm{Pr}T^2}\right)\frac{\partial \hat{\tau}_{m,n}}{\partial \eta}-\frac{\mu}{2\mathrm{Pr}\bar{x}T}\frac{\partial^2 \hat{\tau}_{m,n}}{\partial \eta^2}=r_t\hat{\mathcal{E}}_{m,n},
\end{aligned}
\tag{2.24}
$$

where the terms $\hat{\mathcal{C}}_{m,n}$, $\hat{\mathcal{X}}_{m,n}$, $\hat{\mathcal{Y}}_{m,n}$, $\hat{\mathcal{Z}}_{m,n}$, $\hat{\mathcal{E}}_{m,n}$ arise due to nonlinearity and are given below:

$$
\hat{\mathcal{C}}_{m,n}=\left\{-T\frac{\partial \widehat{\bar{\rho}\bar{u}}}{\partial \bar{x}}+\frac{\eta_cT}{2\bar{x}}\frac{\partial \widehat{\bar{\rho}\bar{u}}}{\partial \eta}-\frac{\partial \widehat{\bar{\rho}\bar{v}}}{\partial \eta}-inT\widehat{\bar{\rho}\bar{w}}+im\widehat{\bar{\rho}\bar{\tau}}+F'\frac{\partial \widehat{\bar{\rho}\bar{\tau}}}{\partial \bar{x}}-\frac{F}{2\bar{x}}\frac{\partial \widehat{\bar{\rho}\bar{\tau}}}{\partial \eta}\right\}_{m,n},
$$

$$
\begin{aligned}
\hat{\mathcal{X}}_{m,n} = \Bigg\{ & \left(-imT + \frac{\eta_c T}{2\bar{x}}F'' + \frac{FT'}{2\bar{x}}\right)\widehat{\bar{\rho}\bar{u}} - F'T\frac{\partial\widehat{\bar{\rho}\bar{u}}}{\partial\bar{x}} + \frac{FT}{2\bar{x}}\frac{\partial\widehat{\bar{\rho}\bar{u}}}{\partial\eta} - \frac{\eta_c}{2\bar{x}}\frac{T'}{T}\widehat{\bar{u}\bar{u}} - \frac{\partial\widehat{\bar{u}\bar{u}}}{\partial\bar{x}} \\
& + \frac{\eta_c}{2\bar{x}}\frac{\partial\widehat{\bar{u}\bar{u}}}{\partial\eta} - r_tT\frac{\partial\widehat{\bar{\rho}\bar{u}\bar{u}}}{\partial\bar{x}} + r_t\frac{\eta_cT}{2\bar{x}}\frac{\partial\widehat{\bar{\rho}\bar{u}\bar{u}}}{\partial\eta} - F''\widehat{\bar{\rho}\bar{v}} + \frac{T'}{T^2}\widehat{\bar{u}\bar{v}} - \frac{1}{T}\frac{\partial\widehat{\bar{u}\bar{v}}}{\partial\eta} - r_t\frac{\partial\widehat{\bar{\rho}\bar{u}\bar{v}}}{\partial\eta} \\
& - in\widehat{\bar{u}\bar{w}} - r_tinT\widehat{\bar{\rho}\bar{u}\bar{w}} - \frac{FF''}{2\bar{x}}\widehat{\bar{\rho}\bar{\tau}} + \frac{1}{2\bar{x}}\left(\frac{\mu'}{T}\right)'\widehat{\bar{\tau}\frac{\partial\bar{u}}{\partial\eta}} + \frac{\mu'}{2\bar{x}T}\frac{\partial}{\partial\eta}\left(\widehat{\bar{\tau}\frac{\partial\bar{u}}{\partial\eta}}\right) \\
& + in\kappa^2T\mu'\widehat{\bar{\tau}\frac{\partial\bar{u}}{\partial\hat{z}}} + \frac{1}{2\bar{x}}\left(\frac{F''}{T}\right)'\hat{\mu} + \frac{F''}{2\bar{x}T}\frac{\partial\hat{\mu}}{\partial\eta} - \frac{r_tT'}{2\bar{x}T^2}\widehat{\bar{\mu}\frac{\partial\bar{u}}{\partial\eta}} + \frac{r_t}{2\bar{x}T}\frac{\partial}{\partial\eta}\left(\widehat{\bar{\mu}\frac{\partial\bar{u}}{\partial\eta}}\right) \\
& + r_tinT\kappa^2\widehat{\bar{\mu}\frac{\partial\bar{u}}{\partial\hat{z}}}\Bigg\}_{m,n},
\end{aligned}
$$

$$
\begin{aligned}
\hat{\mathcal{Y}}_{m,n} = \Bigg\{ & -\frac{T}{4\bar{x}^2}\left[FT + \eta_c(FT' - TF') - \eta_c^2F''T\right]\widehat{\bar{\rho}\bar{u}} - F'T\frac{\partial\widehat{\bar{\rho}\bar{v}}}{\partial\bar{x}} + \frac{FT}{2\bar{x}}\frac{\partial\widehat{\bar{\rho}\bar{v}}}{\partial\eta} \\
& - \left(imT + \frac{\eta_cTF'' + F'T}{2\bar{x}} - \frac{FT'}{\bar{x}}\right)\widehat{\bar{\rho}\bar{v}} - \frac{1}{2\bar{x}}\left(1 + \frac{\eta_cT'}{T}\right)\widehat{\bar{u}\bar{v}} - \frac{\partial\widehat{\bar{u}\bar{v}}}{\partial\bar{x}} \\
& + \frac{\eta_c}{2\bar{x}}\frac{\partial\widehat{\bar{u}\bar{v}}}{\partial\bar{\eta}} - r_t\frac{T}{2\bar{x}}\widehat{\bar{\rho}\bar{u}\bar{v}} - r_tT\frac{\partial\widehat{\bar{\rho}\bar{u}\bar{v}}}{\partial\bar{x}} + r_t\frac{\eta_cT}{2\bar{x}}\frac{\partial\widehat{\bar{\rho}\bar{u}\bar{v}}}{\partial\eta} + \frac{T'}{T^2}\widehat{\bar{v}\bar{v}} - \frac{1}{T}\frac{\partial\widehat{\bar{v}\bar{v}}}{\partial\eta} \\
& - r_t\frac{\partial\widehat{\bar{\rho}\bar{v}\bar{v}}}{\partial\eta} - in\widehat{\bar{v}\bar{w}} - r_tinT\widehat{\bar{\rho}\bar{v}\bar{w}} + \frac{T}{4\bar{x}^2}\left[-\eta_c(FF')' + FF' + \frac{F^2T'}{T}\right]\widehat{\bar{\rho}\bar{\tau}} \\
& - \frac{\mu''T'}{3\bar{x}}\widehat{\bar{\tau}\frac{\partial\bar{u}}{\partial\bar{x}}} - \frac{\mu'}{3\bar{x}}\frac{\partial}{\partial\eta}\left(\widehat{\bar{\tau}\frac{\partial\bar{u}}{\partial\bar{x}}}\right) - \frac{1}{12\bar{x}^2}\left[\mu' + \eta_cT\left(\frac{\mu'}{T}\right)'\right]\widehat{\bar{\tau}\frac{\partial\bar{u}}{\partial\eta}} \\
& + \frac{\mu'}{2\bar{x}}\frac{\partial}{\partial\bar{x}}\left(\widehat{\bar{\tau}\frac{\partial\bar{u}}{\partial\eta}}\right) - \frac{\eta_c\mu'}{12\bar{x}^2}\frac{\partial}{\partial\eta}\left(\widehat{\bar{\tau}\frac{\partial\bar{u}}{\partial\eta}}\right) + \frac{2}{3\bar{x}}\left(\frac{\mu'}{T}\right)'\widehat{\bar{\tau}\frac{\partial\bar{v}}{\partial\eta}} + \frac{2\mu'}{3\bar{x}T}\frac{\partial}{\partial\eta}\left(\widehat{\bar{\tau}\frac{\partial\bar{v}}{\partial\eta}}\right) \\
& + in\kappa^2T\mu'\widehat{\bar{\tau}\frac{\partial\bar{v}}{\partial\hat{z}}} + \frac{in\mu'}{2\bar{x}}\widehat{\bar{\tau}\frac{\partial\bar{w}}{\partial\eta}} - \frac{\mu''T'}{3\bar{x}}\widehat{\bar{\tau}\frac{\partial\bar{w}}{\partial\hat{z}}} - \frac{\mu'}{3\bar{x}}\frac{\partial}{\partial\eta}\left(\widehat{\bar{\tau}\frac{\partial\bar{w}}{\partial\hat{z}}}\right) \\
& + \left[\frac{F(T')^2}{3\bar{x}^2T^2} + \frac{F''}{4\bar{x}^2} - \frac{\eta_cT'F''}{4\bar{x}^2T} - \frac{(FT')'}{3\bar{x}^2T} + \frac{\eta_cF'''}{4\bar{x}^2}\right]\hat{\mu} + \frac{F''}{2\bar{x}}\frac{\partial\hat{\mu}}{\partial\bar{x}} \\
& + \left(\frac{\eta_cF''}{4\bar{x}^2} - \frac{FT'}{3\bar{x}^2T}\right)\frac{\partial\hat{\mu}}{\partial\eta} - \frac{r_t}{3\bar{x}}\frac{\partial}{\partial\eta}\left(\widehat{\bar{\mu}\frac{\partial\bar{u}}{\partial\bar{x}}}\right) + \frac{r_t}{12\bar{x}^2}\left(\frac{\eta_cT'}{T} - 1\right)\widehat{\bar{\mu}\frac{\partial\bar{u}}{\partial\eta}} \\
& + \frac{r_t}{2\bar{x}}\frac{\partial}{\partial\bar{x}}\left(\widehat{\bar{\mu}\frac{\partial\bar{u}}{\partial\eta}}\right) - \frac{r_t\eta_c}{12\bar{x}^2}\frac{\partial}{\partial\eta}\left(\widehat{\bar{\mu}\frac{\partial\bar{u}}{\partial\eta}}\right) - r_t\frac{2T'}{3\bar{x}T^2}\widehat{\bar{\mu}\frac{\partial\bar{v}}{\partial\eta}} + \frac{2r_t}{3\bar{x}T}\frac{\partial}{\partial\eta}\left(\widehat{\bar{\mu}\frac{\partial\bar{v}}{\partial\eta}}\right) \\
& + r_tinT\kappa^2\widehat{\bar{\mu}\frac{\partial\bar{v}}{\partial\hat{z}}} + r_t\frac{in}{2\bar{x}}\widehat{\bar{\mu}\frac{\partial\bar{w}}{\partial\eta}} - \frac{r_t}{3\bar{x}}\frac{\partial}{\partial\eta}\left(\widehat{\bar{\mu}\frac{\partial\bar{w}}{\partial\hat{z}}}\right)\Bigg\}_{m,n},
\end{aligned}
$$

$$
\begin{aligned}
\hat{\mathcal{Z}}_{m,n} = \Bigg\{ & \left(-imT + \frac{FT'}{2\bar{x}}\right)\widehat{\bar{\rho}\bar{w}} - F'T\frac{\partial\widehat{\bar{\rho}\bar{w}}}{\partial\bar{x}} + \frac{FT}{2\bar{x}}\frac{\partial\widehat{\bar{\rho}\bar{w}}}{\partial\eta} - \frac{\eta_cT'}{2\bar{x}T}\widehat{\bar{u}\bar{w}} - \frac{\partial\widehat{\bar{u}\bar{w}}}{\partial\bar{x}} \\
& + \frac{\eta_c}{2\bar{x}}\frac{\partial\widehat{\bar{u}\bar{w}}}{\partial\eta} - r_tT\frac{\partial\widehat{\bar{\rho}\bar{u}\bar{w}}}{\partial\bar{x}} + r_t\frac{\eta_cT}{2\bar{x}}\frac{\partial\widehat{\bar{\rho}\bar{u}\bar{w}}}{\partial\eta} + \frac{T'}{T^2}\widehat{\bar{v}\bar{w}} - \frac{1}{T}\frac{\partial\widehat{\bar{v}\bar{w}}}{\partial\eta} - r_t\frac{\partial\widehat{\bar{\rho}\bar{v}\bar{w}}}{\partial\eta}
\end{aligned}
$$

$$
\begin{aligned}
&- in\widehat{\bar{w}\bar{w}} - r_t inT\widehat{\bar{\rho}\bar{w}\bar{w}} - \frac{2inT\kappa^2\mu'}{3}\widehat{\bar{\tau}\frac{\partial \bar{u}}{\partial \bar{x}}} + \frac{inT\kappa^2\mu'\eta_c}{3\bar{x}}\widehat{\bar{\tau}\frac{\partial \bar{u}}{\partial \eta}} - \frac{\eta_c\kappa^2\mu''TT'}{2\bar{x}}\widehat{\bar{\tau}\frac{\partial \bar{u}}{\partial \hat{z}}} \\
&+ T\mu'\kappa^2\frac{\partial}{\partial \bar{x}}\left(\widehat{\bar{\tau}\frac{\partial \bar{u}}{\partial \hat{z}}}\right) - \frac{\eta_c\kappa^2 T\mu'}{2\bar{x}}\frac{\partial}{\partial \eta}\left(\widehat{\bar{\tau}\frac{\partial \bar{u}}{\partial \hat{z}}}\right) - \frac{2in\kappa^2\mu'}{3}\widehat{\bar{\tau}\frac{\partial \bar{v}}{\partial \eta}} + \mu''T'\kappa^2\widehat{\bar{\tau}\frac{\partial \bar{v}}{\partial \hat{z}}} \\
&+ \mu'\kappa^2\frac{\partial}{\partial \eta}\left(\widehat{\bar{\tau}\frac{\partial \bar{v}}{\partial \hat{z}}}\right) + \frac{1}{2\bar{x}}\left(\frac{\mu'}{T}\right)'\widehat{\bar{\tau}\frac{\partial \bar{w}}{\partial \eta}} + \frac{\mu'}{2\bar{x}T}\frac{\partial}{\partial \eta}\left(\widehat{\bar{\tau}\frac{\partial \bar{w}}{\partial \eta}}\right) + \frac{4\mu' inT\kappa^2}{3}\widehat{\bar{\tau}\frac{\partial \bar{w}}{\partial \hat{z}}} \\
&+ \frac{in\kappa^2 FT'}{3\bar{x}}\hat{\mu} - r_t\frac{2inT\kappa^2}{3}\widehat{\bar{\mu}\frac{\partial \bar{u}}{\partial \bar{x}}} + r_t\frac{inT\kappa^2\eta_c}{3\bar{x}}\widehat{\bar{\mu}\frac{\partial \bar{u}}{\partial \eta}} + r_t T\kappa^2\frac{\partial}{\partial \bar{x}}\left(\widehat{\bar{\mu}\frac{\partial \bar{u}}{\partial \hat{z}}}\right) \\
&- r_t\frac{\eta_c T\kappa^2}{2\bar{x}}\frac{\partial}{\partial \eta}\left(\widehat{\bar{\mu}\frac{\partial \bar{u}}{\partial \hat{z}}}\right) - r_t\frac{2in\kappa^2}{3}\widehat{\bar{\mu}\frac{\partial \bar{v}}{\partial \eta}} + r_t\kappa^2\frac{\partial}{\partial \eta}\left(\widehat{\bar{\mu}\frac{\partial \bar{v}}{\partial \hat{z}}}\right) - r_t\frac{T'}{2\bar{x}T^2}\widehat{\mu\frac{\partial \bar{w}}{\partial \eta}} \\
&\left.+ \frac{r_t}{2\bar{x}T}\frac{\partial}{\partial \eta}\left(\widehat{\bar{\mu}\frac{\partial \bar{w}}{\partial \eta}}\right) + r_t\frac{4inT\kappa^2}{3}\widehat{\bar{\mu}\frac{\partial \bar{w}}{\partial \hat{z}}}\right\}_{m,n},
\end{aligned}
$$

$$
\begin{aligned}
\hat{\mathcal{E}}_{m,n} = &\left\{\frac{\eta_c T'T}{2\bar{x}}\widehat{\bar{\rho}\bar{u}} - r_t T\frac{\partial \widehat{\bar{\rho}\bar{u}\bar{\tau}}}{\partial \bar{x}} + r_t\frac{\eta_c T}{2\bar{x}}\frac{\partial \widehat{\bar{\rho}\bar{u}\bar{\tau}}}{\partial \eta} - T'\widehat{\bar{\rho}\bar{v}} - r_t\frac{\partial \widehat{\bar{\rho}\bar{v}\bar{\tau}}}{\partial \eta} - r_t inT\widehat{\bar{\rho}\bar{w}\bar{\tau}}\right. \\
&- imT\widehat{\bar{\rho}\bar{\tau}} - F'T\frac{\partial \widehat{\bar{\rho}\bar{\tau}}}{\partial \bar{x}} + \frac{FT}{2\bar{x}}\frac{\partial \widehat{\bar{\rho}\bar{\tau}}}{\partial \eta} - \frac{\eta_c T'}{2\bar{x}T}\widehat{\bar{u}\bar{\tau}} - \frac{\partial \widehat{\bar{u}\bar{\tau}}}{\partial \bar{x}} + \frac{\eta_c}{2\bar{x}}\frac{\partial \widehat{\bar{u}\bar{\tau}}}{\partial \eta} + \frac{T'}{T^2}\widehat{\bar{v}\bar{\tau}} \\
&- \frac{1}{T}\frac{\partial \widehat{\bar{v}\bar{\tau}}}{\partial \eta} - in\widehat{\bar{w}\bar{\tau}} - \frac{\mu' Tn^2\kappa^2}{2\mathrm{Pr}}\widehat{\bar{\tau}^2} + \frac{1}{2\bar{x}\mathrm{Pr}}\left(\frac{\mu'}{T}\right)'\widehat{\bar{\tau}\frac{\partial \bar{\tau}}{\partial \eta}} + \frac{\mu'}{2\bar{x}\mathrm{Pr}T}\frac{\partial}{\partial \eta}\left(\widehat{\bar{\tau}\frac{\partial \bar{\tau}}{\partial \eta}}\right) \\
&+ \frac{M_\infty^2(\gamma-1)\mu}{2\bar{x}T}\widehat{\left(\frac{\partial \bar{u}}{\partial \eta}\right)^2} + \frac{M_\infty^2(\gamma-1)\mu' F''}{\bar{x}T}\widehat{\frac{\partial \bar{u}}{\partial \eta}\bar{\tau}} + r_t\frac{M_\infty^2(\gamma-1)\mu'}{2\bar{x}T}\widehat{\left(\frac{\partial \bar{u}}{\partial \eta}\right)^2\bar{\tau}} \\
&+ M_\infty^2(\gamma-1)\kappa^2 T\mu\widehat{\left(\frac{\partial \bar{u}}{\partial \hat{z}}\right)^2} + M_\infty^2(\gamma-1)r_t\kappa^2 T\mu'\widehat{\left(\frac{\partial \bar{u}}{\partial \hat{z}}\right)^2\bar{\tau}} \\
&+ \left[\frac{1}{2\bar{x}\mathrm{Pr}}\left(\frac{T'}{T}\right)' + \frac{M_\infty^2(\gamma-1)(F'')^2}{2\bar{x}T}\right]\hat{\mu} + \frac{T'}{2\bar{x}\mathrm{Pr}T}\frac{\partial \hat{\mu}}{\partial \eta} \\
&+ r_t\frac{M_\infty^2(\gamma-1)F''}{\bar{x}T}\widehat{\bar{\mu}\frac{\partial \bar{u}}{\partial \eta}} + r_t^2\frac{M_\infty^2(\gamma-1)}{2\bar{x}T}\widehat{\bar{\mu}\left(\frac{\partial \bar{u}}{\partial \eta}\right)^2} + r_t^2 M_\infty^2(\gamma-1)T\kappa^2\widehat{\bar{\mu}\left(\frac{\partial \bar{u}}{\partial \hat{z}}\right)^2} \\
&\left.- r_t\frac{T'}{2\bar{x}\mathrm{Pr}T^2}\widehat{\bar{\mu}\frac{\partial \bar{\tau}}{\partial \eta}} + \frac{r_t}{2\bar{x}\mathrm{Pr}T}\frac{\partial}{\partial \eta}\left(\widehat{\bar{\mu}\frac{\partial \bar{\tau}}{\partial \eta}}\right) + r_t\frac{inT\kappa^2}{\mathrm{Pr}}\widehat{\bar{\mu}\frac{\partial \bar{\tau}}{\partial \hat{z}}}\right\}_{m,n},
\end{aligned}
$$

with $\hat{z}=k_z z$. The right-hand sides of (2.20)-(2.24), where the nonlinear terms are collected, vanish as $r_t \to 0$ so that the linearized compressible unsteady boundary-region equations of Ricco and Wu (2007) are recovered. Note that the above fully nonlinear equations are to be used to predict the entire development of streaks even though the disturbance turns out to evolve through a linear stage near the leading edge.

2.1.3 The outer flow

The outer-flow dynamics are influenced by the displacement of the underlying boundary-layer flow. The displacement effect becomes of leading order at downstream distances where $\bar{x}=\mathcal{O}(1)$ and the streamwise-velocity fluctuations acquire an $\mathcal{O}(1)$-amplitude. The disturbance in the outer region consists of the three-dimensional vortical perturbation convected from upstream and of the two-dimensional disturbance arising from the boundary-layer displacement effect due to the nonlinear interactions in the boundary layer. The two-dimensional component attenuates over a wall-normal distance $\mathcal{O}(\lambda^* R_\lambda)$, and thus depends on the relatively slow wall-normal variable $\bar{y}$, which is the appropriate transverse variable, defined as $\bar{y}=k_x y=\mathcal{O}(1)$. The three-dimensional component depends on y and, *a priori*, also on $\bar{y}$ because its governing equations involve the two-dimensional component as we will discuss later. Following the approach of Wundrow and Goldstein (2001) and Ricco *et al.* (2011), the outer-region solution is expanded as:

$$\{u_{out}, v_{out}, w_{out}, p_{out}, \tau_{out}\} = \mathbf{Q}+\epsilon\bar{\mathbf{q}}_0(\bar{x},\bar{y},\bar{t})+\epsilon\mathbf{q}_0(\bar{x},y,\bar{y},z,\bar{t})+\epsilon^2\mathbf{q}_1(\bar{x},y,\bar{y},z,\bar{t})+..., \tag{2.25}$$

where $\bar{t}=k_x t=\mathcal{O}(1)$, $\mathbf{Q}$ is the uniform mean flow, and $\bar{\mathbf{q}}_\mathbf{i}$ and $\mathbf{q}_\mathbf{i}$ (i=0, 1, ...) indicate the two-dimensional and three-dimensional disturbances, respectively.

Linearized inviscid subsonic and supersonic flows

The two-dimensional inviscid part of the perturbation is considered first: the subsonic and supersonic regimes are analyzed by extending the approach of Ricco *et al.* (2011) to take compressibility into account. The transonic case is however beyond the scope of the present analysis. The two-dimensional terms

$\{\bar{u}_0, \bar{v}_0, \bar{p}_0, \bar{\tau}_0, \bar{\rho}_0\}$ satisfy the linearized unsteady compressible Euler equations:

$$\frac{\partial \bar{u}_0}{\partial \bar{x}} + \frac{\partial \bar{v}_0}{\partial \bar{y}} + M_\infty^2 \left(\frac{\partial \bar{p}_0}{\partial \bar{t}} + \frac{\partial \bar{p}_0}{\partial \bar{x}} \right) = 0, \tag{2.26a}$$

$$\frac{\partial \bar{u}_0}{\partial \bar{t}} + \frac{\partial \bar{u}_0}{\partial \bar{x}} + \frac{\partial \bar{p}_0}{\partial \bar{x}} = 0, \tag{2.26b}$$

$$\frac{\partial \bar{v}_0}{\partial \bar{t}} + \frac{\partial \bar{v}_0}{\partial \bar{x}} + \frac{\partial \bar{p}_0}{\partial \bar{y}} = 0, \tag{2.26c}$$

where the density has been eliminated from the continuity equation by using the energy equation and the equation of state,

$$\frac{\partial \bar{\tau}_0}{\partial \bar{t}} + \frac{\partial \bar{\tau}_0}{\partial \bar{x}} - (\gamma - 1) M_\infty^2 \left(\frac{\partial \bar{p}_0}{\partial \bar{t}} + \frac{\partial \bar{p}_0}{\partial \bar{x}} \right) = 0, \qquad \bar{\rho}_0 = \gamma M_\infty^2 \bar{p}_0 - \bar{\tau}_0. \tag{2.27}$$

The displacement effect is related to the transpiration velocity, that is the spanwise-averaged wall-normal velocity component at the boundary-layer outer edge. The continuity equation,

$$\frac{\partial \rho_{tot}}{\partial t} + \frac{\partial (\rho_{tot} u_{tot})}{\partial x} + \frac{\partial (\rho_{tot} v_{tot})}{\partial y} + \frac{\partial (\rho_{tot} w_{tot})}{\partial z} = 0,$$

is integrated with respect to z over a spanwise period $\lambda_z{=}2\pi/k_z$ and with respect to y from 0 to ∞. For the term $\partial(\rho_{tot} w_{tot})/\partial z$ a change in the order of integration is performed. At supersonic speeds this step is justified by the assumption that shock waves, if present, are of infinitesimal strength and therefore the flow remains smooth and isentropic. It follows that

$$\frac{1}{\lambda_z} \int_0^{\lambda_z} (\rho_{tot} v_{tot})|_{y \to \infty} \mathrm{d}z = -\frac{k_x}{\lambda_z} \left[\int_0^{\lambda_z} \int_0^{\infty} \frac{\partial (\rho_{tot} u_{tot})}{\partial \bar{x}} \mathrm{d}y \mathrm{d}z + \int_0^{\lambda_z} \int_0^{\infty} \frac{\partial \rho_{tot}}{\partial \bar{t}} \mathrm{d}y \mathrm{d}z \right]. \tag{2.28}$$

The first term on the right-hand side of (2.28) represents the derivative with respect to $\bar{x}$ of the spanwise-averaged boundary-layer displacement thickness, defined as

$$\bar{\delta}(\bar{x},\bar{t}) = \frac{1}{\lambda_z}\int_0^{\lambda_z}\int_0^{\infty}\left[1-(\rho_{tot}u_{tot})\right]\mathrm{d}y\mathrm{d}z.$$

The second term on the right-hand side of (2.28) is due to compressibility effects and is not present in Ricco *et al.* (2011). It can be written as the derivative with respect to $\bar{t}$ of a spanwise-averaged boundary-layer thickness $\bar{\delta}^c$ defined as

$$\bar{\delta}^c(\bar{x},\bar{t}) = \frac{1}{\lambda_z}\int_0^{\lambda_z}\int_0^{\infty}\left(1-\rho_{tot}\right)\mathrm{d}y\mathrm{d}z.$$

Matching the left-hand side of (2.28) with the outer flow gives

$$\frac{1}{\lambda_z}\int_0^{\lambda_z}(\rho_{tot}v_{tot})|_{y\to\infty}\mathrm{d}z = \frac{1}{\lambda_z}\int_0^{\lambda_z}(\rho_{out}v_{out})|_{\bar{y}\to 0}\mathrm{d}z = \epsilon\bar{v}_0,$$

where the terms $\mathcal{O}(\epsilon^2)$ have been neglected. Therefore, (2.28) leads to

$$\bar{v}_0 = \frac{k_x}{\epsilon}\left(\frac{\partial\bar{\delta}}{\partial\bar{x}}+\frac{\partial\bar{\delta}^c}{\partial\bar{t}}\right) \quad \text{as } \bar{y}\to 0, \tag{2.29}$$

where the compressibility effects appear in the definition of the displacement thickness $\bar{\delta}$ and in the additional term $\bar{\delta}^c$. Equation (2.29) is used as a boundary condition on the system (2.26).

The proof employed by Ricco *et al.* (2011) to show the irrotationality of the two-dimensional flow holds for the compressible case as long as the flow remains isentropic (i.e. shock waves are absent or, if present, their effect is negligible). Therefore, the potential $\bar{\phi}_0$ is introduced such that $\nabla_{\bar{x}\bar{y}}\bar{\phi}_0=\{\bar{u}_0,\bar{v}_0\}$, where $\nabla_{\bar{x}\bar{y}}$ denotes the gradient in the $\bar{x}-\bar{y}$ plane. By rewriting (2.26) in terms of $\bar{\phi}_0$ and eliminating the pressure from the continuity equation with the aid of the momentum equations, a single equation for the potential is derived,

$$\frac{\partial^2\bar{\phi}_0}{\partial\bar{y}^2}+(1-M_\infty^2)\frac{\partial^2\bar{\phi}_0}{\partial\bar{x}^2}-2M_\infty^2\frac{\partial^2\bar{\phi}_0}{\partial\bar{x}\partial\bar{t}}-M_\infty^2\frac{\partial^2\bar{\phi}_0}{\partial\bar{t}^2}=0, \qquad M_\infty\neq 1, \tag{2.30}$$

which is a wave (i.e. hyperbolic) equation, indicating the acoustic nature of the perturbation. It is interesting that streaks emit sound waves spontaneously during their nonlinear evolution. Equation (2.30) is of the same form as the linearized perturbation-velocity potential equation governing the flow over a thin airfoil performing small unsteady (periodic) oscillations in the transverse direction (refer to Landahl, 1989, equation (1.7)). The small thickness of the airfoil is represented here by the boundary-layer displacement thickness, the equivalent body being semi-infinite rather than finite and closed (i.e. with null thickness at both ends of the body).

The problem of the flow over a thin oscillating airfoil has been widely studied in aeroelasticity because of the loads and vibrations occurring on the wing. Thanks to the linearization, two separated cases are distinguished: the thickness problem (symmetrical) and the lifting problem (anti-symmetrical). Aeroelasticians are usually interested in the latter because of the contribution to the lift experienced by the wing (Dowell, 2014). Here it suffices to state that the analogy between the boundary-layer displacement effect and the thin airfoil theory only concerns the thickness problem, as circulatory flow is absent. This analogy was first suggested by Lighthill (1958) for incompressible flows and its use in the study of steady flows outside boundary layers has been well established (Van Dyke, 1975). However, to the best of our knowledge, this analogy has never been considered for unsteady boundary layers.

By employing Fourier decomposition in time,

$$\bar{\phi}_0(\bar{x},\bar{y},\bar{t}) = \sum_m \hat{\phi}_m(\bar{x},\bar{y}) e^{im\bar{t}},$$

equation (2.30) is recast into a generalized Helmholtz differential equation (i.e. telegraph equation) for the Fourier coefficients $\hat{\phi}_m(\bar{x},\bar{y})$:

$$\frac{\partial^2\hat{\phi}_m}{\partial\bar{y}^2}+(1-M_\infty^2)\frac{\partial^2\hat{\phi}_m}{\partial\bar{x}^2}-2imM_\infty^2\frac{\partial\hat{\phi}_m}{\partial\bar{x}}+m^2M_\infty^2\hat{\phi}_m=0. \tag{2.31}$$

Performing the change $\hat{\phi}_m\to\hat{\Phi}_m$, where

$$\hat{\phi}_m(\bar{x},\bar{y})=\hat{\Phi}_m(\bar{x},\bar{y})e^{-b\bar{x}/2}\qquad\text{with } b=\frac{2imM_\infty^2}{M_\infty^2-1},\quad M_\infty\neq 1, \tag{2.32}$$

the telegraph equation (2.31) is reduced to either the Helmholtz equation if $M_\infty<1$ or the Klein-Gordon equation if $M_\infty>1$:

$$|1-M_\infty^2|\frac{\partial^2\hat{\Phi}_m}{\partial\bar{x}^2}\pm\frac{\partial^2\hat{\Phi}_m}{\partial\bar{y}^2}+\frac{m^2M_\infty^2}{|1-M_\infty^2|}\hat{\Phi}_m=0, \tag{2.33}$$

where the $+$ or $-$ sign correspond to the subsonic or supersonic case, respectively. The appropriate boundary conditions for (2.33) are:

$$\frac{\partial\hat{\Phi}_m}{\partial\bar{y}}=\begin{cases}\dfrac{k_x}{\epsilon}\left(\hat{\delta}'_m+im\hat{\delta}^c_m\right)e^{b\bar{x}/2}, & \bar{y}=0,\bar{x}\geq 0,\\[2ex] 0, & \bar{y}=0,\bar{x}<0;\end{cases} \tag{2.34a}$$

$$\frac{\partial\hat{\Phi}_m}{\partial\bar{x}},\frac{\partial\hat{\Phi}_m}{\partial\bar{y}}\ \text{finite},\qquad \bar{x}^2+\bar{y}^2\to\infty, \tag{2.34b}$$

where $\hat{\delta}_m(\bar{x})$ and $\hat{\delta}^c_m(\bar{x})$ are the Fourier coefficients of $\bar{\delta}(\bar{x},\bar{t})$, and $\bar{\delta}^c(\bar{x},\bar{t})$ and the prime represents differentiation with respect to $\bar{x}$. Equation (2.34a) corresponds to the tangency (i.e. no penetration) condition imposed on a thin airfoil, according to which the velocity component normal to the body is fixed by the airfoil motion. This analogy has given rise to the well-known interpretation of the boundary-layer displacement effect as a surface distribution of sources (Lighthill, 1958). The far-field boundary condition (2.34b) requires that the displacement-induced velocity field remains finite as the distance from the plate increases.

In the supersonic case it is convenient to solve for $\hat{\phi}_m$ directly from (2.31). The fluid ahead of the body remains undisturbed and so the Laplace transform in the $\bar{x}$ direction can be employed,

$$\tilde{\phi}_m(s,\bar{y}) = \int_0^\infty \hat{\phi}_m(\bar{x},\bar{y}) e^{-s\bar{x}} \mathrm{d}\bar{x}.$$

The telegraph equation (2.31) and the boundary condition (2.34a) for $\bar{x}{\geq}0$ become:

$$\frac{\partial^2 \tilde{\phi}_m}{\partial \bar{y}^2} = c^2 \tilde{\phi}_m, \qquad \frac{\partial \tilde{\phi}_m}{\partial \bar{y}}(s,0) = \tilde{v}_m(s,0), \tag{2.35}$$

where $c^2 = s^2 \left(M_\infty^2 - 1\right) + m M_\infty^2 (2is - m)$ and $\tilde{v}_m(s,0)$ indicates the Laplace transform of $\dfrac{\partial \hat{\phi}_m}{\partial \bar{y}}(\bar{x},0)$. The solution to (2.35) is

$$\tilde{\phi}_m(s,\bar{y}) = -\frac{\tilde{v}_m(s,0)}{c} e^{-c\bar{y}}, \qquad \bar{y} \geq 0. \tag{2.36}$$

Inverting (2.36) and using the convolution theorem, one finds

$$\begin{aligned}\hat{\phi}_m(\bar{x},\bar{y};M_\infty{>}1) = &-\frac{k_x}{\epsilon\sqrt{M_\infty^2-1}} \int\limits_0^{\bar{x}-\bar{y}\sqrt{M_\infty^2-1}} \left[\hat{\delta}'_m(\bar{x}_0) + im\hat{\delta}^c_m(\bar{x}_0)\right] e^{-\frac{imM_\infty^2}{M_\infty^2-1}(\bar{x}-\bar{x}_0)} \\ &\times J_0\left[\frac{mM_\infty}{M_\infty^2-1}\sqrt{\left(\bar{x}-\bar{x}_0\right)^2 - \left(M_\infty^2-1\right)\bar{y}^2}\,\right] \mathrm{d}\bar{x}_0,\end{aligned} \tag{2.37}$$

where J_0 is the zeroth-order Bessel function of the first kind (Abramowitz and Stegun, 1964). The procedure to derive (2.37) closely follows the theory proposed by Stewartson (1950) for harmonically-oscillating thin airfoils in supersonic flows.

In the subsonic case, the disturbance is felt in all directions and so the Laplace transform in $\bar{x}$ is not appropriate. The Fourier transform is instead employed and the analytic continuation of the Neumann boundary condition (2.34a) to the complex plane $\bar{\xi} = \bar{x} + i\bar{y}$ is considered. The solution reads

$$\begin{aligned}\hat{\phi}_m(\bar{x},\bar{y};M_\infty{<}1) = &-\frac{ik_x}{2\epsilon\sqrt{1-M_\infty^2}} \int\limits_{\bar{x}-i\bar{y}\sqrt{1-M_\infty^2}}^{\bar{x}+i\bar{y}\sqrt{1-M_\infty^2}} \left[\hat{\delta}'_m(\bar{\xi}) + im\hat{\delta}^c_m(\bar{\xi})\right] e^{\frac{imM_\infty^2}{1-M_\infty^2}(\bar{x}-\bar{\xi})} \\ &\times J_0\left[\frac{mM_\infty}{1-M_\infty^2}\sqrt{\left(\bar{x}-\bar{\xi}\right)^2+\left(1-M_\infty^2\right)\bar{y}^2}\right]\mathrm{d}\bar{\xi}.\end{aligned} \tag{2.38}$$

The solution can also be expressed in terms of the Green's function by modelling the boundary-layer thickness as a distribution of pulsating sources as suggested by Lighthill's theory. The free-space Green's function associated with Helmholtz equation (2.33) is given by Dragos (2004) on page 33 for a single source located in the origin. Considering a line distribution of these sources at the point $(\bar{x}_0, 0)$, where $\bar{x}_0$ spans the $\bar{x}$ axis, and using the method of images to include the boundary $\bar{y}{=}0$, we obtain

$$\begin{aligned}\hat{\phi}_m(\bar{x},\bar{y};M_\infty{<}1) = &\frac{ik_x}{2\epsilon\sqrt{1-M_\infty^2}} \int\limits_0^\infty \left[\hat{\delta}'_m(\bar{x}_0) + im\hat{\delta}^c_m(\bar{x}_0)\right] e^{\frac{imM_\infty^2}{1-M_\infty^2}(\bar{x}-\bar{x}_0)} \\ &\times H_0^{(2)}\left[\frac{mM_\infty}{1-M_\infty^2}\sqrt{\left(\bar{x}-\bar{x}_0\right)^2+\left(1-M_\infty^2\right)\bar{y}^2}\right]\mathrm{d}\bar{x}_0,\end{aligned} \tag{2.39}$$

where $H_0^{(2)}$ is the zeroth-order Hankel function of the second kind (Abramowitz and Stegun, 1964). The solution with $H_0^{(2)}$ has been chosen instead of that with $H_0^{(1)}$ to ensure outgoing waves radiating from the source. As $M_\infty{\to}0$, (2.38) matches the solution obtained in the incompressible case (Ricco *et al.*, 2011):

$$\hat{\phi}_m(\bar{x},\bar{y}) \to \frac{k_x}{\epsilon}\Im\left[\hat{\delta}_m(\bar{x}+i\bar{y})\right],$$

where $\Im$ indicates the imaginary part. For the detailed derivation of the matching the reader is referred to Appendix C. The limit $M_\infty{\to}\infty$ is not considered because for very large hypersonic Mach numbers the Blasius boundary-layer assumption of negligible wall-normal pressure gradient is invalid (refer to Anderson, 2006, page 275).

The pressure is obtained from the y-momentum equation (2.26c) as

$$\bar{p}_0 = -\left(\frac{\partial \bar{\phi}_0}{\partial \bar{t}} + \frac{\partial \bar{\phi}_0}{\partial \bar{x}}\right), \tag{2.40}$$

or, in Fourier space,

$$\hat{p}_m = -\left(im\hat{\phi}_m + \frac{\partial \hat{\phi}_m}{\partial \bar{x}}\right). \tag{2.41}$$

From substitution of the supersonic and subsonic expressions for the potential, (2.37) and (2.39), into (2.41), it follows that

$$\begin{aligned}\hat{p}_m(\bar{x},\bar{y};M_\infty{>}1) = \frac{k_x}{\epsilon\sqrt{M_\infty^2-1}} \Bigg\{ &\int\limits_0^{\bar{x}-\bar{y}\sqrt{M_\infty^2-1}} f(\bar{x_0},\bar{x},\bar{y})\mathrm{d}\bar{x_0} \left[\hat{\delta}'_m\left(\bar{x}-\bar{y}\sqrt{M_\infty^2-1}\right)\right. \\ &\left. +im\hat{\delta}^c_m\left(\bar{x}-\bar{y}\sqrt{M_\infty^2-1}\right)\right] e^{-\frac{imM_\infty^2}{\sqrt{M_\infty^2-1}}\bar{y}} \Bigg\}\end{aligned}$$

in the supersonic case, where

$$\begin{aligned} f = &\left[\hat{\delta}'_m(\bar{x}_0) + im\hat{\delta}^c_m(\bar{x}_0)\right] e^{-\frac{imM_\infty^2}{M_\infty^2-1}(\bar{x}-\bar{x}_0)} \\ &\times \left\{\frac{m}{M_\infty^2-1}\left[iJ_0\left(\frac{mM_\infty}{M_\infty^2-1}\sqrt{\left(\bar{x}-\bar{x}_0\right)^2-\left(M_\infty^2-1\right)\bar{y}^2}\right)\right.\right. \\ &\left.\left.+\frac{M_\infty\left(\bar{x}-\bar{x}_0\right)}{\sqrt{\left(\bar{x}-\bar{x}_0\right)^2-\left(M_\infty^2-1\right)\bar{y}^2}}J_1\left(\frac{mM_\infty}{M_\infty^2-1}\sqrt{\left(\bar{x}-\bar{x}_0\right)^2-\left(M_\infty^2-1\right)\bar{y}^2}\right)\right]\right]\right\}\end{aligned}$$

and J_1 is the first-order Bessel function of the first kind (Abramowitz and Stegun, 1964), and in the subsonic case

$$\hat{p}_m(\bar{x},\bar{y};M_\infty{<}1) = \frac{ik_x}{2\epsilon\sqrt{1-M_\infty^2}}\int\limits_0^\infty g(\bar{x_0},\bar{x},\bar{y})\mathrm{d}\bar{x_0},$$

where

$$\begin{aligned} g = {} & \left[\hat{\delta}'_m(\bar{x}_0) + im\hat{\delta}^c_m(\bar{x}_0)\right] e^{\frac{imM_\infty^2}{1-M_\infty^2}(\bar{x}-\bar{x}_0)} \\ & \times \left\{ \frac{m}{1-M_\infty^2} \left[iH_0^{(2)} \left(\frac{mM_\infty}{1-M_\infty^2} \sqrt{\left(\bar{x}-\bar{x}_0\right)^2 + \left(1-M_\infty^2\right)\bar{y}^2} \right) \right.\right. \\ & \left.\left. - \frac{M_\infty\left(\bar{x}-\bar{x}_0\right)}{\sqrt{\left(\bar{x}-\bar{x}_0\right)^2 + \left(1-M_\infty^2\right)\bar{y}^2}} H_1^{(2)} \left(\frac{mM_\infty}{1-M_\infty^2} \sqrt{\left(\bar{x}-\bar{x}_0\right)^2 + \left(1-M_\infty^2\right)\bar{y}^2} \right) \right] \right\}, \end{aligned}$$

and $H_1^{(2)}$ is the first-order Hankel function of the second kind (Abramowitz and Stegun, 1964). The temperature is found from the energy equation (2.27) as

$$\bar{\tau}_0 = (\gamma - 1) M_\infty^2 \bar{p}_0. \tag{2.42}$$

Viscous three-dimensional flow

By substituting the expansion (2.25) into the Navier-Stokes equations and subtracting the equations (2.26) and (2.27) for the displacement-induced disturbance, the leading order three-dimensional part of the perturbation is found to satisfy the equations:

$$\frac{\partial v_0}{\partial y} + \frac{\partial w_0}{\partial z} = 0, \tag{2.43}$$

$$\mathcal{M} \begin{Bmatrix} u_0 \\ v_0 \\ w_0 \\ \tau_0 \end{Bmatrix} = -\frac{\epsilon}{k_x} \begin{Bmatrix} 0 \\ \partial p_1/\partial y \\ \partial p_1/\partial z \\ 0 \end{Bmatrix} + \kappa^2 \nabla_{yz}^2 \begin{Bmatrix} u_0 \\ v_0 \\ w_0 \\ \mathrm{Pr}^{-1}\tau_0 \end{Bmatrix}, \tag{2.44}$$

where p_0=0 without loss of generality, ∇_{yz} is the gradient operator in the $y - z$ plane and $\mathcal{M}$ is the differential operator

$$\mathcal{M} = \left\{ \frac{\partial}{\partial \bar{t}} + \frac{\partial}{\partial \bar{x}} + \frac{\epsilon}{k_x} \left[(\bar{v}_0 + v_0)\frac{\partial}{\partial y} + w_0 \frac{\partial}{\partial z} \right] \right\}. \tag{2.45}$$

The three-dimensional part of the perturbation in (2.43) and (2.44) does not directly depend on the slow variable $\bar{y}$ at the leading order, but the momentum equations (2.44) include the inviscid wall-normal velocity component $\bar{v}_0$, which depends on $\bar{y}$. The aim of the following analysis is to decouple (2.44) from $\bar{v}_0$ to obtain a system of equations in the only unknowns $\{u_0, v_0, w_0, \tau_0, p_1\}$. This is accomplished by introducing the Prandtl transformation, $\hat{y}{=}y-\Re[\Delta(\bar{\xi}, \bar{t})]$, where $\Re$ denotes the real part and Δ is suitably chosen to eliminate the coupling between $\{u_0, v_0, w_0, \tau_0, p_1\}$ and $\bar{v}_0$ from (2.44). The new variable $\hat{y}$ is written in this form for consistency with the previous analyses of Wundrow and Goldstein (2001) and Ricco *et al.* (2011), although it will turn out that only the dependence of Δ on the real variables $\bar{x}$ and $\bar{t}$ is relevant since we are interested in the matching at $\bar{y}{=}0$. Written in terms of $\hat{y}$, equations (2.43)-(2.44) become

$$\frac{\partial v_0}{\partial \hat{y}} + \frac{\partial w_0}{\partial z} = 0, \tag{2.46}$$

$$\mathcal{N}\begin{Bmatrix} u_0 \\ v_0 \\ w_0 \\ \tau_0 \end{Bmatrix} = -\frac{\epsilon}{k_x}\begin{Bmatrix} 0 \\ p_{1\hat{y}} \\ p_{1z} \\ 0 \end{Bmatrix} + \kappa^2 \nabla^2_{\hat{y}z}\begin{Bmatrix} u_0 \\ v_0 \\ w_0 \\ \mathrm{Pr}^{-1}\tau_0 \end{Bmatrix}, \tag{2.47}$$

where $\nabla_{\hat{y}z}$ is the gradient operator in the $\hat{y}-z$ plane and $\mathcal{N}$ is the differential operator:

$$\mathcal{N} = \frac{\partial}{\partial \bar{t}} + \frac{\partial}{\partial \bar{x}} + \frac{\epsilon}{k_x}\left(v_0\frac{\partial}{\partial \hat{y}} + w_0\frac{\partial}{\partial z}\right) - \left(\Re\left[\frac{\partial \Delta}{\partial \bar{t}} + \frac{\partial \Delta}{\partial \bar{\xi}}\right] - \frac{\epsilon}{k_x}\bar{v}_0\right)\frac{\partial}{\partial \hat{y}}.$$

The dependence on $\bar{v}_0$ is removed by choosing Δ to satisfy (Ricco *et al.*, 2011)

$$\Re\left[\frac{\partial \Delta}{\partial \bar{t}} + \frac{\partial \Delta}{\partial \bar{\xi}}\right] = \frac{\epsilon}{k_x}\bar{v}_0,$$

which, in view of (2.29), becomes

$$\frac{\partial \Delta}{\partial \bar{t}} + \frac{\partial \Delta}{\partial \bar{x}} = \frac{\partial \bar{\delta}}{\partial \bar{x}} + \frac{\partial \bar{\delta}^c}{\partial \bar{t}} \qquad \text{at } \bar{y} = 0.$$

Decomposing Δ into Fourier series as

$$\Delta\left(\bar{x}, \bar{t}\right) = \sum_m \hat{\Delta}_m(\bar{x}) e^{-im(\bar{x}-\bar{t})} \qquad \text{at } \bar{y} = 0,$$

and using the time Fourier series of $\bar{\delta}$ and $\bar{\delta}^c$, we obtain the expression for $\hat{\Delta}_m$,

$$\hat{\Delta}_m(\bar{x}) = \hat{\delta}_m(\bar{x}) e^{im\bar{x}} + im \int_0^{\bar{x}} \left[\hat{\delta}_m(\check{x}) - \hat{\delta}^c_m(\check{x})\right] e^{im\check{x}} \mathrm{d}\check{x}, \qquad \text{at } \bar{y} = 0, \tag{2.48}$$

where the condition $\Delta(0, \bar{t})=0$, $\forall \bar{t}>0$ has been employed.

Equations (2.47) show that the streamwise velocity u_0 and the temperature τ_0 are decoupled from the transverse velocities $\{v_0, w_0\}$ and from the pressure p_1. At leading order only $\{v_0, w_0, p_1\}$ enter the matching with the boundary-layer solution, while the matching of $\{u_0, \tau_0\}$ needs to be considered when a solution with an order of accuracy higher than $\mathcal{O}(R_\lambda^{-1})$ is required.

In light of (2.46), the streamfunction $\psi_0(\bar{x}, \hat{y}, z, \bar{t})$ is introduced such that $\nabla_{\hat{y}z}\psi_0=\{-w_0, v_0\}$. In terms of the streamfunction the transverse momentum equations are recast into a transport equation for the longitudinal vorticity $\nabla^2_{\hat{y}z}\psi_0$,

$$\left[\frac{\partial}{\partial \bar{t}} + \frac{\partial}{\partial \bar{x}} + \frac{\epsilon}{k_x}\left(\frac{\partial \psi_0}{\partial z}\frac{\partial}{\partial \hat{y}} - \frac{\partial \psi_0}{\partial \hat{y}}\frac{\partial}{\partial \hat{z}}\right)\right] \nabla^2_{\hat{y}z}\psi_0 = \kappa^2 \nabla^4_{\hat{y}z}\psi_0, \tag{2.49}$$

along with the Poisson equation for the pressure,

$$\nabla^2_{\hat{y}z} p_1 = 2\left[\frac{\partial^2 \psi_0}{\partial \hat{y}^2}\frac{\partial^2 \psi_0}{\partial z^2} - \left(\frac{\partial^2 \psi_0}{\partial \hat{y}\partial z}\right)^2\right]. \tag{2.50}$$

In the general case of a full forcing spectrum of free-stream vortical disturbances, the streamfunction is decomposed as:

$$\psi_0\left(\bar{x},\hat{y},z,\bar{t}\right)=\sum_{m,n,j}\hat{\psi}^{(j)}_{m,n}(\bar{x})e^{i(m\bar{t}+jk_y\hat{y}+nk_z z)}. \tag{2.51}$$

By substituting (2.51) into (2.49) and expanding the resulting equation for a pair of oblique forcing modes (i.e. $\{m,j,n\}$=$\{1,-1,\pm1\}$), the nonlinear terms cancel out with (2.49) reducing to

$$\left(im+\frac{\partial}{\partial\bar{x}}\right)\hat{\psi}^{(j)}_{m,n}=-\kappa^2\left(j^2k_y^2+n^2k_z^2\right)\hat{\psi}^{(j)}_{m,n}.$$

The solution is:

$$\hat{\psi}^{(-1)}_{1,\pm1}=\mp ic_\infty e^{-i\bar{x}-\kappa^2(k_y^2+k_z^2)\bar{x}}+c.c., \tag{2.52}$$

where c_∞=$1/k_y$ is chosen to normalize the amplitude of the free-stream spanwise velocity to unity. From (2.51) and (2.52) it follows that

$$\psi_0\left(\bar{x},\hat{y},z,\bar{t}\right)=-2ic_\infty\cos\left(\bar{x}-\bar{t}+k_y\hat{y}\right)e^{-\kappa^2(k_y^2+k_z^2)\bar{x}+ik_z z}+c.c.. \tag{2.53}$$

The transverse velocities are obtained as

$$v_0=2c_\infty k_z\cos\left(\bar{x}-\bar{t}+k_y\hat{y}\right)e^{-\kappa^2(k_y^2+k_z^2)\bar{x}+ik_z z}+c.c., \tag{2.54a}$$

$$w_0=-2ic_\infty k_y\sin\left(\bar{x}-\bar{t}+k_y\hat{y}\right)e^{-\kappa^2(k_y^2+k_z^2)\bar{x}+ik_z z}+c.c.. \tag{2.54b}$$

By inserting (2.53) into (2.50), the pressure is found to be

$$p_1=2c_\infty^2\left[k_y^2e^{2ik_z z}-k_z^2\cos\left(2\bar{x}-2\bar{t}+2k_y\hat{y}\right)\right]e^{-2\kappa^2(k_y^2+k_z^2)\bar{x}}+c.c.. \tag{2.55}$$

At $\bar{y}$=0, the expression $\hat{y}$=y−$\Delta(\bar{x},\bar{t})$ is substituted into (2.53)-(2.55), and the time-dependent terms are expanded into Fourier series,

$$e^{i\bar{t}+ik_y\Delta(\bar{x},\bar{t})} = \sum_m \hat{\chi}_m(\bar{x})e^{im\bar{t}}, \qquad e^{2i\bar{t}+2ik_y\Delta(\bar{x},\bar{t})} = \sum_m \hat{\pi}_m(\bar{x})e^{im\bar{t}}. \tag{2.56}$$

Rewriting (2.54a) and (2.55) with the aid of (2.56), the outer-flow solution for y=$\mathcal{O}(1)$ is obtained as

$$\{v_0, w_0, p_1\} = \sum_{m,n} \left\{v^\dagger_{m,n}, w^\dagger_{m,n}, p^\dagger_{m,n}\right\} e^{im\bar{t}+ink_z z}, \tag{2.57}$$

with

$$v^\dagger_{m,\pm1} = k_z c_\infty e^{-\kappa^2(k_y^2+k_z^2)\bar{x}}\left[\hat{\chi}_m e^{-i(\bar{x}+k_y y)} + \hat{\chi}^\star_{-m} e^{i(\bar{x}+k_y y)}\right], \tag{2.58a}$$

$$w^\dagger_{m,\pm1} = \pm k_y c_\infty e^{-\kappa^2(k_y^2+k_z^2)\bar{x}}\left[\hat{\chi}_m e^{-i(\bar{x}+k_y y)} - \hat{\chi}^\star_{-m} e^{i(\bar{x}+k_y y)}\right], \tag{2.58b}$$

$$p^\dagger_{0,\pm2} = 2k_y^2 c_\infty^2 e^{-2\kappa^2(k_y^2+k_z^2)\bar{x}}, \tag{2.58c}$$

$$p^\dagger_{m,0} = -2k_z^2 c_\infty^2 e^{-2\kappa^2(k_y^2+k_z^2)\bar{x}}\left[\hat{\pi}_m e^{-2i(\bar{x}+k_y y)} + \hat{\pi}^\star_{-m} e^{2i(\bar{x}+k_y y)}\right]. \tag{2.58d}$$

The other components $v^\dagger_{m,n}, w^\dagger_{m,n}$ with $n \neq \pm 1$ and $p^\dagger_{m,n}$ with $n \neq 0, \pm 2$ are null. Although the upstream flow is forced only by a pair of oblique modes with opposite spanwise wavenumbers, further downstream the disturbance is composed of all the temporal harmonics, which are generated by nonlinear interactions in the boundary layer and transmitted to the outer flow via the displacement effect. Although the Fourier components (2.58) are of the same form as those obtained in the incompressible case (refer to Ricco *et al.*, 2011, equation (2.28)), the coefficients $\hat{\chi}_m$ and $\hat{\pi}_m$ defined in (2.56) now include the compressible effects, the function $\Delta(\bar{x},\bar{t})$ being related to δ and δ^c through (2.48).

2.1.4 Initial and boundary conditions

As the boundary-region equations (2.20)-(2.24) constitute a parabolic system in the streamwise direction, initial conditions are needed for $\bar{x} \ll 1$. Since the velocity and temperature fluctuations are of small amplitude near the leading edge, their governing equations become linear. This was elucidated by Ricco *et al.* (2011), who showed that the full nonlinear regime evolves gradually from the initial linear regime in the upstream region corresponding to $R_\lambda^{-1} \ll \bar{x} \ll 1$. The initial conditions for the forced modes $(m,n) = (1, \pm 1)$ are thus the same as those in Ricco and Wu (2007).

The upstream conditions are obtained by first expanding the solution into power series $\eta = \mathcal{O}(1)$ and $\bar{x} \ll 1$,

$$\{\bar{u}, \bar{v}, \bar{w}, \bar{\tau}, \bar{p}\} = \sum_{n=0}^{\infty} (2\bar{x})^{n/2} \left\{ 2\bar{x} U_n(\eta), V_n(\eta), W_n(\eta), 2\bar{x} T_n(\eta), (2\bar{x})^{-1/2} P_n(\eta) \right\},$$

and by constructing a composite solution that is valid for $\bar{x} \ll 1$ and $\forall \eta$:

$$\{\hat{u}, \hat{v}, \hat{w}, \hat{\tau}, \hat{p}\}_{-1,\pm 1} \rightarrow \pm \frac{i\kappa^2}{k_z} u_{z,w,\pm} \{U_{in}, V_{in}, \mp i W_{in}, T_{in}, P_{in}\}, \tag{2.59}$$

where $\{U_{in}, V_{in}, W_{in}, T_{in}, P_{in}\}$ are equal to the right-hand sides of equations (4.12)-(4.16) in Ricco and Wu (2007). The term $u_{z,w,\pm}$ represents the spanwise slip velocity at the surface of the plate (refer to Leib *et al.*, 1999, equation (3.14)). In the case of a pair of oblique modes, it is given by

$$u_{z,w,\pm} = \mp 1 \pm \frac{i k_z}{\sqrt{k_x^2 + k_z^2}} \hat{u}_{y,\pm}^{\infty}.$$

For all the other harmonics generated by nonlinear effects, null initial velocity, temperature and pressure profiles are imposed.

The velocity fluctuations are required to vanish at the wall (no-slip condition).

Two types of different thermal boundary conditions at the wall may be imposed: the Dirichlet boundary condition, $\bar{\tau}(0)=0$, which was also employed by Ricco and Wu (2007), and the Neumann boundary condition, $\partial\bar{\tau}/\partial\eta|_{\eta=0}=0$. The condition $\bar{\tau}(0)=0$ is used herein as Ricco *et al.* (2009) showed that there is no substantial difference in the development of the Klebanoff modes.

As $\eta\to\infty$, the boundary-region solution must match to the limit $\bar{y}\to 0$ of the outer flow. On taking into account the decomposition (2.13) and (2.14) within the boundary layer, the matching with the outer solution (2.57) requires that

$$\{\hat{u}_{m,n}, \hat{v}_{m,n}, \hat{w}_{m,n}, \hat{p}_{m,n}, \hat{\tau}_{m,n}\} \to \left\{0, \frac{\kappa}{\sqrt{2\bar{x}}} v^{\dagger}_{m,n}, \kappa^2 w^{\dagger}_{m,n}, \frac{\epsilon}{k_x} p^{\dagger}_{m,n}, 0\right\} \text{ as } \eta\to\infty \tag{2.60}$$

for $\bar{x}=\mathcal{O}(1)$, where the condition on $\hat{v}_{m,n}$ holds only for $n\neq 0$. In the spanwise-averaged equations ($n=0$) the pressure only appears in the y-momentum equation. The velocities and the temperature are calculated by solving the continuity, $x-$ and $z-$momentum and the energy equations. The condition on $\hat{v}_{m,0}$ as $\eta\to\infty$ is not needed because the order of the system has decreased. As an *a posteriori* check, the free-stream value of $\hat{v}_{m,0}$ is obtained from the large-η limit of the continuity equation,

$$\begin{aligned}\hat{v}_{m,0}(\bar{x}, \eta\to\infty) &= \frac{k_x}{\epsilon}\frac{\kappa}{\sqrt{2\bar{x}}}\left(\frac{\mathrm{d}\hat{\delta}_m}{\mathrm{d}\bar{x}} - \frac{\mathrm{d}\delta_{bl}}{\mathrm{d}\bar{x}} + im\hat{\delta}^c_m\right)\\ &= -\int_0^\infty \left(\frac{\partial \hat{u}_{m,0}}{\partial\bar{x}} + \frac{\hat{u}_{m,0}}{2\bar{x}}\right)\mathrm{d}\eta + \int_0^\infty \frac{F'}{T}\left(\frac{\partial\hat{\tau}_{m,0}}{\partial\bar{x}} + \frac{\hat{\tau}_{m,0}}{2\bar{x}}\right)\mathrm{d}\eta\\ &\quad + \int_0^\infty \frac{im}{T}\hat{\tau}_{m,0}\mathrm{d}\eta - r_t\int_0^\infty T\left(\frac{\partial\widehat{\bar{\rho}\bar{u}}_{m,0}}{\partial\bar{x}} + \frac{\widehat{\bar{\rho}\bar{u}}_{m,0}}{2\bar{x}}\right)\mathrm{d}\eta\\ &\quad + r_t\int_0^\infty \frac{im}{T}\widehat{\bar{\rho}\bar{\tau}}_{m,0}\mathrm{d}\eta + r_t\int_0^\infty F'\left(\frac{\partial\widehat{\bar{\rho}\bar{\tau}}_{m,0}}{\partial\bar{x}} + \frac{\widehat{\bar{\rho}\bar{\tau}}_{m,0}}{2\bar{x}}\right)\mathrm{d}\eta,\end{aligned} \tag{2.61}$$

where δ_{bl} is the compressible Blasius displacement thickness,

$$\delta_{bl} = \int_0^\infty \left[1 - \frac{F'(\eta)}{T(\eta)}\right] \mathrm{d}y = \sqrt{\frac{2\bar{x}}{k_x R_\lambda}}(\gamma_c + \beta_c),$$

and $\gamma_c{=}\eta_c - \eta$ as $\eta{\to}\infty$. In the limit $M_\infty{\to}0$ the result of Ricco *et al.* (2011) is recovered:

$$\hat{v}_{m,0}(\bar{x}, \eta \to \infty) = \frac{k_x}{\epsilon}\frac{\kappa}{\sqrt{2\bar{x}}}\left(\frac{\mathrm{d}\hat{\delta}_m}{\mathrm{d}\bar{x}} - \frac{\mathrm{d}\delta_{bl}}{\mathrm{d}\bar{x}}\right) = -\int_0^\infty \left(\frac{\partial \hat{u}_{m,0}}{\partial \bar{x}} + \frac{\hat{u}_{m,0}}{2\bar{x}}\right)\mathrm{d}\eta,$$

where $\delta_{bl}{=}\int_0^\infty [1 - F'(\eta)]\, \mathrm{d}y{=}\beta\sqrt{2\bar{x}/k_x R_\lambda}$ is the incompressible Blasius displacement thickness and $\beta{=}1.2168$. In the compressible case the additional terms related to $\bar{\delta}^c$ in (2.61) are present or absent depending on the motion being unsteady or steady, while in the incompressible case the transpiration velocity is not affected by unsteady effects.

2.2 Numerical procedures

The Fourier coefficients $\{\hat{u}_{m,n}, \hat{v}_{m,n}, \hat{w}_{m,n}, \hat{p}_{m,n}, \hat{\tau}_{m,n}\}$ are obtained by solving the boundary-region equations (2.20)-(2.24) with the initial conditions (2.59) and the boundary conditions (2.60). The wall-normal domain extends to $\eta_{\max}{=}60$, and 2000 grid points are employed in this direction. The typical grid size in the marching direction is $\Delta\bar{x}{=}10^{-3}$. After discretization with a second-order finite-difference scheme, a block tri-diagonal system is obtained. The latter is solved by means of a block-elimination algorithm described in Ricco (2006) (refer also to Cebeci, 2002, pages 260-264, for the detailed procedure).

Particular care is devoted to the solution of the boundary-region equations in the spanwise-averaged case (i.e. $n{=}0$), as the pressure $\hat{p}_{m,0}$ vanishes in the z-momentum equation. It only appears in the y-momentum equation as $\partial\hat{p}_{m,0}/\partial\eta$. Therefore, the three velocity components and the temperature are computed by only solving the continuity, x- and z-momentum and energy equations. The spanwise-averaged pressure fluctuations $\hat{p}_{m,0}$ can be calculated *a posteriori* by solving the y-momentum equation and using the boundary condition (2.60). In order to avoid the pressure decoupling phenomenon, the pressure is computed on a grid that is staggered in the η direction with respect to the grid employed for the velocity and temperature.

The initial conditions (2.59) for the wall-normal and spanwise velocity components contain a term proportional to $\exp[-|\kappa|\sqrt{2\bar{x}}\eta]$, which represents a reflected disturbance by the wall. The mixed boundary conditions (4.7)-(4.10) of Ricco and Wu (2007) accommodate the transverse decay of this reflected disturbance. For very small $\bar{x}$, the Dirichlet conditions (2.60) are consistent with the initial conditions (2.59) if $|\kappa|\sqrt{2\bar{x}}\eta \gg 1$, i.e when the reflected disturbance is negligible. Because of this condition a very large $\eta_{\max}$ needs to be employed at small $\bar{x}$. To avoid this, the mixed outer conditions (4.7)-(4.10) of Ricco and Wu (2007) are used to march the boundary-region equations for a short downstream distance, after which the boundary conditions are switched to (2.60). Typically, the switching occurs at a streamwise location $\bar{x}$=0.02-0.04 where the solution is still linear. Accurate numerical checks have been carried out to assure that the cross-flow velocity components match the values imposed by (2.60) smoothly and that the results are not affected by the switching location. In Appendix D the far-field conditions of the mixed and Dirichlet types are shown to be consistent as they both match onto the oncoming disturbance.

The nonlinear terms of the boundary-region equations (2.20)-(2.24) are evaluated using the pseudo-spectral method (Canuto *et al.*, 1988), that is, the spectral variables are inverse Fourier transformed to physical space to perform multiplications and the products are then transformed back to the spectral space. Dealiasing is performed by using the so-called 3/2-rule to avoid the spurious cascade

$$\begin{tikzcd}
\hat{\tau}_{m,n} \arrow[r, "1."] & \bar{\tau} \arrow[d, "2."] \\
\begin{array}{c}\hat{\rho}_{m,n} \\ \hat{\mu}_{m,n}\end{array} & \begin{array}{c}\bar{\rho} \\ \bar{\mu}\end{array} \arrow[l, "3."']
\end{tikzcd}$$

Fig. 2.2: Schematic of the procedure used to calculate the density and viscosity fluctuations. The numbers on the arrows refer to the steps described in the text.

of the unresolved higher-frequency fluctuations into the resolved lower-frequency modes (Canuto *et al.*, 1988).

The density fluctuations are calculated using (2.16), where the first term is neglected with respect to the other two because $k_x/R_\lambda \ll 1$. The viscosity fluctuations are evaluated using (2.18), where the summation is started from $j{=}2$ to exclude the mean flow and the linear part of the disturbance. The following steps are performed to obtain $\hat{\rho}_{m,n}$ and $\hat{\mu}_{m,n}$ (as shown schematically in figure 2.2).

1. The temperature fluctuation $\hat{\tau}_{m,n}$ is transformed back from the spectral to physical space to calculate $\bar{\tau}$.

2. The fluctuations of density and viscosity are evaluated as follows

$$\bar{\rho} = -\frac{\bar{\tau}}{T(T + r_t\bar{\tau})}, \quad \bar{\mu} = \sum_{j=2}^{\infty} \frac{(\omega)_j}{j!} T^{\omega-j} r_t^{j-2} \bar{\tau}^j.$$

3. The latter are transformed back to the spectral space to obtain $\hat{\rho}_{m,n}$ and $\hat{\mu}_{m,n}$.

The Hermitian property (2.15) is exploited to reduce the computational cost of the numerical solution of the boundary-region problem. The property is applied for time t, that is, only the half of the Fourier modes with positive m index are calculated. A second-order predictor-corrector scheme is used to compute the nonlinear terms while marching downstream. At each $\bar{x}$ location, the nonlinear terms are first treated explicitly using the velocity and temperature field at the previous $\bar{x}$ location with no extrapolation. A predicted solution is thus obtained by solving the resulting linear algebraic system and is used, together with the previous downstream solution, to compute the nonlinear terms again. This procedure is repeated until the difference between the predictor (the solution at the previous iteration) and the corrector (the solution at the current iteration) is smaller than a specified tolerance. Extensive resolution checks have been carried out to verify the accuracy of the code. The amplitudes of the truncated Fourier series are six or seven order of magnitude smaller than that of the forcing modes and so they do not significantly affect the flow dynamics. Use of N_t=N_z=9 is sufficient to capture the nonlinear effects in the case r_t=2, while for r_t=4 an accuracy of the same order is obtained with N_t=N_z=13.

To calculate the outer-flow field in the subsonic case, we solve the Helmholtz equation (2.33) numerically with $M_\infty<1$ to obtain $\hat{\Phi}_m(\bar{x},\bar{y})$, and the Fourier coefficients $\hat{\phi}_m(\bar{x},\bar{y})$ are then retrieved from (2.32). The computational domain for $\bar{x}\geq 0$ extends sufficiently downstream for the forcing at $\bar{y}$=0 to vanish. The symmetry about $\bar{y}=0$ implies the homogeneous Neumann boundary condition $\partial\hat{\Phi}_m/\partial\bar{y}=0$ is used at $\bar{y}$=0 and $\bar{x}<0$. Careful resolution checks have been performed to ensure that the solution is independent of the size of the computational domain. The Helmholtz equation is discretized with a second-order finite difference scheme in $\bar{x}$ and $\bar{y}$. The resulting block tri-diagonal matrix is solved at each point using the generalized minimum residual method (Saad and Schultz, 1986) with diagonal preconditioner implemented in the Iterative Methods Library, IML++ (Dongarra *et al.*, 2006).

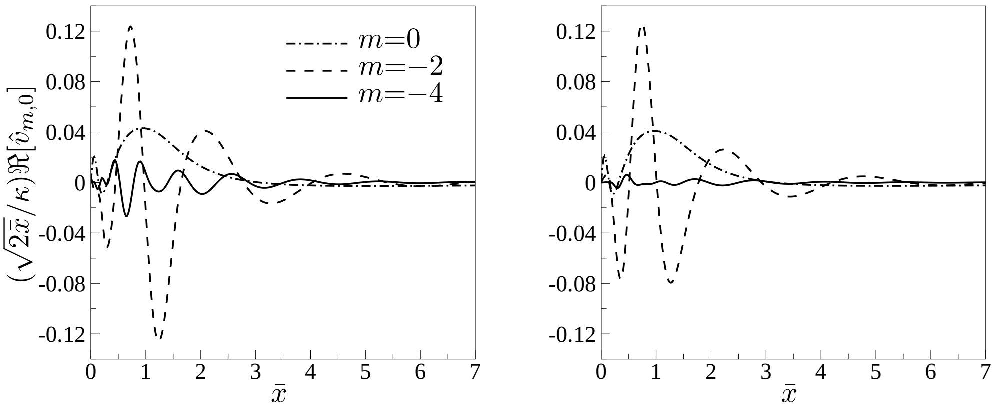

Fig. 2.3: Large-η limit of $\hat{v}_{m,0}$ for M_∞=0.69 (left) and M_∞=3 (right).

2.3 Results for the outer flow

The solution for the irrotational part of the outer flow $\bar{\mathbf{q}}_0(\bar{x},\bar{y},\bar{t})$ (refer to equation (2.25)) is studied in this section. The streamwise and wall-normal velocity components, $\bar{u}_0(\bar{x},\bar{y},\bar{t})$ and $\bar{v}_0(\bar{x},\bar{y},\bar{t})$, are calculated for two different flow regimes: a subsonic case with $\{M_\infty, R_\lambda, r_t, \kappa\}$=$\{0.69, 600, 3.6, 1.3\}$ and a supersonic case with $\{M_\infty, R_\lambda, r_t, \kappa\}$=$\{3, 1000, 3.6, 1.12\}$.

The displacement induced transverse velocity $\hat{v}_{m,0}$ given in (2.61) represents, after multiplication by $\sqrt{2\bar{x}}/\kappa$, the Neumann boundary condition at $\bar{y}$=0 for $\hat{\phi}_m$ and is shown in figure 2.3 for the subsonic and supersonic cases. Only the real part of the modes with $|m|$=0, 2, 4 is considered, as the imaginary part is similar to the real part and higher harmonics are negligible. Physically, the terms $\hat{v}_{m,0}(\bar{x},\eta\gg1)$ represent the harmonics of a spanwise-averaged time-periodic modulation which is superimposed onto the slope of the Blasius displacement thickness. In the light of the thin-airfoil theory analogy, this modulation is interpreted as the strength of the pulse-source distribution.

In the subsonic case, due to the difficulty in calculating the integral in (2.38), the solution is obtained numerically, as explained in §2.2. In the supersonic case, the solution (2.37) is employed to calculate the Fourier coefficients $\hat{\phi}_m(\bar{x}, \bar{y})$, from which $\bar{u}_0(\bar{x}, \bar{y}, \bar{t})$ and $\bar{v}_0(\bar{x}, \bar{y}, \bar{t})$ are obtained. The pressure $\bar{p}_0(\bar{x}, \bar{y}, \bar{t})$ is derived from (2.40).

Contours of $\bar{u}_0$, $\bar{v}_0$ and $\bar{p}_0$ in the $\bar{x} - \bar{y}$ plane, which represent the acoustic field emitted by streaks, are shown in figures 2.4 and 2.5 at two different times $\bar{t}$ for the subsonic and supersonic cases, respectively. According to (2.42) the temperature $\bar{\tau}_0$ differs from $\bar{p}_0$ by a factor $(\gamma - 1)M_\infty^2$, which is equal to 0.19 and 3.6 in the two flow regimes considered. The scale for the temperature $\bar{\tau}_0$ is thus reported together with that for the pressure.

In the subsonic case, the influence of the boundary-layer thickness pulsation propagates in all directions from the plate and gradually diminishes as the distance from the body increases. The streamwise modulation of the solution is caused by the oscillatory forcing at $\bar{y}$=0, which corresponds to a sequence of sources with positive and negative strength (refer to figure 2.3). The apparent ‘wavelength’ of modulation is $\Delta\bar{x} \approx 0.5$. The outer-flow solution shows the most intense peaks for $0.5<\bar{x}<2$, i.e. where the forcing is strongest.

The supersonic solution, shown in figure 2.5, is non zero only inside the Mach dihedron delimited by the Mach line $\bar{y}=\bar{x}/\sqrt{M_\infty^2 - 1}$, as in the thin airfoil theory (Dragos, 2004, page 32). The magnitude of the disturbance is constant along the Mach line and thus the perturbations do not vanish as $\bar{y}\to\infty$.

2.4 Results for the boundary-layer streaks

The parameters for the numerical results are selected to be representative of two possible applications: subsonic turbomachinery and supersonic flight conditions. The former is characterized by a relatively low Mach number and an intense turbulence level, while the latter features a higher Mach number and a quieter disturbance environment. An idealized case of a supersonic wind-tunnel flow with

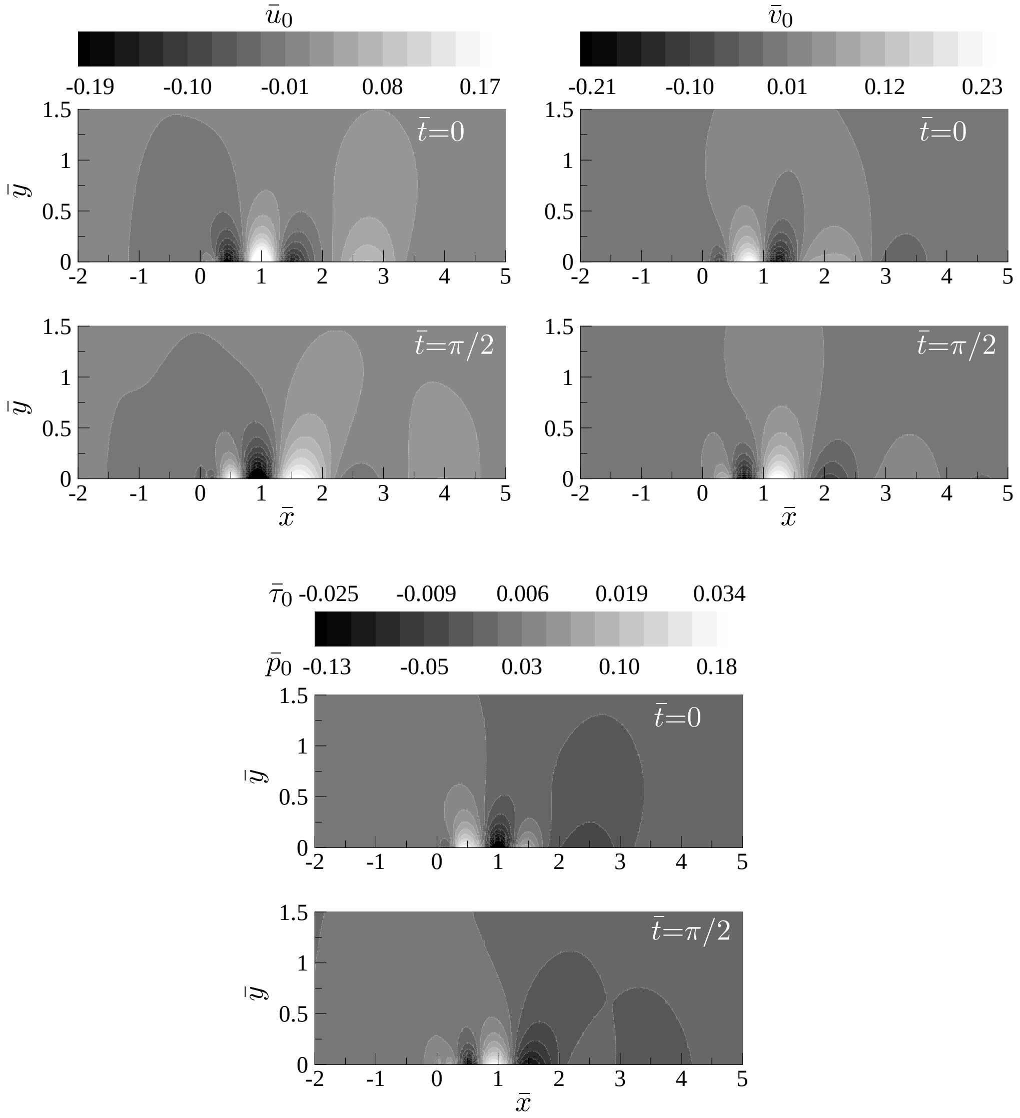

Fig. 2.4: Contours of the streamwise and wall-normal velocity components, $\bar{u}_0$ and $\bar{v}_0$, the pressure $\bar{p}_0$ and the temperature $\bar{\tau}_0$ in $\bar{x}-\bar{y}$ plane, at different times $\bar{t}$ for M_∞=0.69.

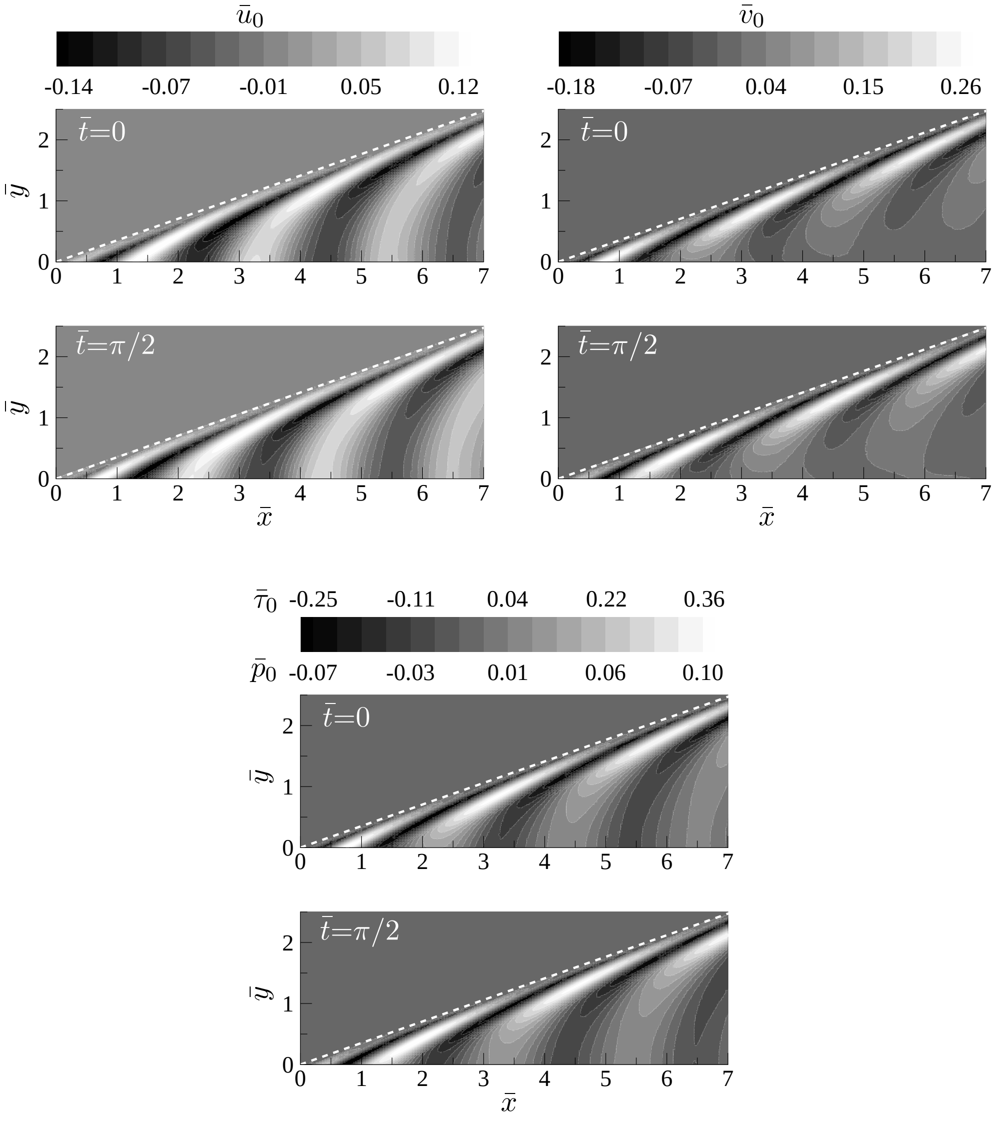

Fig. 2.5: Contours of the streamwise and wall-normal velocity components, $\bar{u}_0$ and $\bar{v}_0$, the pressure $\bar{p}_0$ and the temperature $\bar{\tau}_0$ in $\bar{x} - \bar{y}$ plane, at different times $\bar{t}$ for M_∞=3. The dashed lines represent the Mach line $\bar{y}$=$\bar{x}/\sqrt{M_\infty^2 - 1}$.

no acoustic modes is also considered. In all the cases, the scaled amplitudes of the free-stream turbulence velocity components are: $\hat{u}^{\infty}_{x,\pm}=\hat{u}^{\infty}_{y,\pm}=1$ and $\hat{u}^{\infty}_{z,\pm}=\mp 1$. Through continuity (2.4), this leads to the following relation for the wavenumbers: $k_x + k_y - 1=0$.

In the following, the parameters employed for the three sets of calculations are presented and the relevant results are shown. The reader may skip §2.4.1 without loss of clarity.

2.4.1 Choice of parameters

Turbomachinery applications

With a reference to typical experimental works on turbomachinery applications (e.g. Camci and Arts, 1990) the following parameters are adopted: unit Reynolds number $R^*_{1\infty}\equiv U^*_\infty/\nu^*_\infty=8 \times 10^6$ m^{-1}, chord length $\ell^*=8$ cm, free-stream temperature and kinematic viscosity of air at that temperature $T^*_\infty=500$ K and $\nu^*_\infty=3.9 \times 10^{-5}$ m^{2}s^{-1}, free-stream Mach number $M_\infty=0.69$ and turbulence level $Tu=0.8 - 5.2\%$. Although we have chosen our flow parameters to be as close as possible to the experimental ones, important extra factors are present in real experimental and technological flow systems, such as acoustic free-stream forcing, surface curvature, pressure gradient and wall cooling. These can be taken into account by suitable extensions of the present framework. For example, the boundary-region-equation approach has been extended to study the generation and development of Görtler vortices in the incompressible boundary layer over a concave wall (refer to Wu *et al.,* 2011 for the linearized case and to chapter 3 of this thesis for the nonlinear case). With further progress, precise quantitative comparisons with experiments and applications to practical situations would be possible eventually. Presently, the results are of qualitative value as far as their relevance to turbomachinery is concerned. The adiabatic-wall temperature is calculated using the following relation valid for a perfect gas,

$$T^*_{ad} = T^*_\infty \left(1 + C_t \frac{\gamma - 1}{2} M^2_\infty\right), \tag{2.62}$$

where C_t is the recovery factor. In a laminar boundary layer over a flat plate $C_t = \sqrt{\mathrm{Pr}}$. The resulting adiabatic-wall temperature, $T^*_{ad} = 540.5$ K, is in the range of typical turbine-rotor applications. The ratio of the wall temperature to the adiabatic-wall temperature $T^*_w / T^*_{ad} = 0.7$ is chosen to mimic realistic aero-engine conditions (Zhang and He, 2014), where blade cooling is most often applied to avoid excessive surface temperature. The resulting non-dimensional wall temperature is $T_w = 0.75$.

As the relevant length scales and spectra of the free-stream turbulence are not documented in the experiments, we have to assume that the ratio of the streamwise integral scale to the chord is equal to 1.5. It follows that $\lambda^*_x = 0.12$ m and the frequency $f^* = U^*_\infty / \lambda^*_x = 2.5$ kHz. At downstream locations where $x^* = \mathcal{O}(\lambda^* R_\lambda)$, the boundary-layer thickness is comparable with the spanwise length scale λ^*. The laminar boundary-layer thickness is proportional to $\sqrt{\nu^*_\infty x^* / U^*_\infty}$, and it is estimated that transition occurs at $x^*_T / \ell^* = 0.67$ (i.e. $x^*_T = 5.36$ cm), which corresponds to a critical Reynolds number of 5×10^5 (Schlichting and Gersten, 2000). It follows that the boundary-layer thickness δ^*_{99}, defined as the wall-normal location where $U = 0.99$, is 0.41 mm, and the displacement thickness is $\delta^* = 0.14$ mm. The latter value is taken as the reference length scale λ^*. The Reynolds number R_λ and the scaled streamwise wavenumber κ are worked out by use of (2.5) and (2.7). The free-stream disturbance intensity is defined as $Tu = 2\epsilon\sqrt{(\hat{u}^\infty_{x,+})^2 + (\hat{u}^\infty_{x,-})^2}$. For our choice of $\hat{u}^\infty_{x,\pm} = 1$, $Tu = 2\sqrt{2}\epsilon$. Given ϵ and R_λ, the turbulent Reynolds number r_t is calculated from (2.8). The influence of nonlinear effects is investigated by varying the turbulence level (i.e. ϵ) with all the other parameters kept constant, as shown in table 2.1(a). Two different values of $\lambda^*_x / \ell^* = 0.77$, 3.1 are considered in order to study the effect of the streamwise wavenumber (refer to table 2.1(b)). The relation between λ_z^*, shown in table 2.1, and λ^* is $\lambda_z^*{=}2\pi\lambda^*$.

Flight conditions

The data reported in Schneider (1999) are analysed to infer typical parameters for supersonic flight conditions. The following values are adopted: free-stream Mach number $M_\infty{=}3$, unit Reynolds number $R_{1\infty}^*{=}3.33 \times 10^6$ m^{-1} and wall-temperature ratio $T_w^*/T_{ad}^*{=}0.5$. The latter value is in the typical range of high-supersonic flight speeds, where, in addition to aerodynamic heating, radiative cooling also occurs due to the solid wall of the body radiating energy from the surface (Fedorov and Khokhlov, 2001). A free-stream temperature $T_\infty^*{=}218$ K is assumed at a typical altitude for supersonic flight of 20 km (Wilson *et al.*, 1971). It follows that the velocity and the kinematic viscosity of air in the free stream are $U_\infty^*{=}888$ ms^{-1} and $\nu_\infty^*{=}2.67 \times 10^{-4}$ m^{2}s^{-1}. From (2.62) the adiabatic-wall temperature $T_{ad}^*{=}548$ K is obtained. It follows that $T_w^*{=}274$ K. The boundary-layer thickness δ^* at high Mach number is assumed to grow as $x^* M_\infty^2/\sqrt{R_x}$, where R_x is the local Reynolds number at the edge of the boundary layer (refer to Anderson, 2006, equation (7.9)). At the transition-onset location $x_T^*{=}0.1$ m (Schneider, 1999), $\delta^*{=}1.5$ mm, which is taken as the reference length scale, $\lambda^*{=}\delta^*$.

Considering the data reported in figure 6 of Wilson *et al.* (1971) and figure 1 of Hocking (1985) on the atmospheric turbulence power spectra and scales, a streamwise wavelength $\lambda_x^*{=}3.68$ m is chosen. The corresponding frequency is $f^*{=}240.8$ Hz. In-flight measurements by Riedel and Sitzmann (1998) and Saric (2008) indicate that the turbulence level in subsonic flight for the quiescent air atmosphere is $0.05 - 0.06\%$. For the high-altitude environment of a supersonic aircraft, Coleman and Steiner (1960) and Ehernberger and Love (1975) report even lower turbulence intensities. However, close to inversion layers (i.e. areas where the usual trend of decrease in air temperature with increasing altitude is reversed) or within clouds, large turbulence levels in the range $0.1\%<Tu<1\%$ or more may occur (Zanin, 1985). The turbulence levels for our simulations are chosen as representative of these atmospheric conditions ($0.1\%<Tu<0.3\%$).

The influence of compressibility is investigated by varying M_∞. It is assumed that the variation of M_∞ is only due to a variation of the free-stream velocity U_∞^*, while the free-stream temperature T_∞^* is unchanged. Therefore, a_∞^* and ν_∞^* are also constant. The wall temperature is the same in all the cases considered, while T_{ad}^* varies according to (2.62) for different Mach numbers. The dimensional amplitude of the gust is kept fixed at 2.39 ms^{-1}. It follows that the turbulence level decreases as the free-stream velocity increases, but the turbulence Reynolds number, which is defined by (2.8), does not change because R_λ increases linearly with U_∞^*. The dimensional frequency is kept constant and it corresponds to different λ_x^* depending on U_∞^*, as presented in table 2.1(c). The hypersonic case $M_\infty=6$ should be regarded as approximated because in this regime other effects (e.g. presence of strong shock waves close to the body and high-temperature chemical reactions) may become important (see discussion in §2.1), which are neglected in our model. The degree of idealization is acceptable in this case as the Mach number is still of $\mathcal{O}(1)$ and is in the low range of hypersonic speeds. In order to analyse the effect of nonlinearity at supersonic speeds, two different turbulence levels, $Tu=0.19\%$ and 0.35%, are considered for $M_\infty=3$ (refer to table 2.1(d)).

Wind tunnel conditions

The following parameters are chosen as representative of typical supersonic wind tunnel experiments (Graziosi and Brown, 2002; Fedorov *et al.*, 2003; Beckwith and Miller III, 1990): $M_\infty=3$, $U_\infty^*=646$ ms^{-1}, $\nu_\infty^*=3.7\times10^{-5}$ m^{2}s^{-1}, $T_\infty^*=115.4$ K,

f^*=500Hz, k_x=1.55 × 10^{-3}, R_λ=5400 and κ=0.34. The calculations are performed for three different turbulence levels, Tu=0.11%, 0.23%, 0.31%, which correspond to r_t=2.1, 4.4, 6 (refer to table 2.1(e)). The representation is idealized since acoustic disturbances are excluded.

For these cases the ratio between the wall temperature and the adiabatic-wall temperature provided by Graziosi and Brown (2002), T_w^*/T_{ad}^*=1.1, is employed. The results for this hot-wall condition will be compared with those obtained with the adiabatic condition T_w^*=T_{ad}^* and with the cold-wall condition employed by Fedorov *et al.* (2003), where T_w^*/T_{ad}^*=0.8.

		U^*_∞	ν^*_∞	T^*_∞	λ^*_z	λ^*_x	δ^*_{99}	f^*	M_∞	R_λ	k_x	κ	Tu	r_t
		[ms^{-1}]	[m^{2}s^{-1}]	[K]	[m]	[m]	[m]	[kHz]						
			$\times 10^4$		$\times 10^3$		$\times 10^3$				$\times 10^3$		[%]	
Turbomach.	(a)	309	0.39	500	0.89	0.12	0.41	2.5	0.69	1124	7.3	0.35	0.7	2.7
		309	0.39	500	0.89	0.12	0.41	2.5	0.69	1124	7.3	0.35	2	7.9
	(b)	309	0.39	500	0.89	0.25	0.41	1.25	0.69	1124	3.6	0.5	1.3	5.3
		309	0.39	500	0.89	0.06	0.41	5	0.69	1124	14.2	0.25	1.3	5.3
Flight	(c)	592	2.67	218	9.4	2.5	2.6	0.24	2	3343	3.85	0.28	0.41	4.8
		1776	2.67	218	9.4	7.4	3.8	0.24	6	10029	1.28	0.28	0.14	4.8
	(d)	888	2.67	218	9.4	3.68	2.8	0.24	3	5014	2.6	0.28	0.19	3.37
		888	2.67	218	9.4	3.68	2.8	0.24	3	5014	2.6	0.28	0.35	6.25
W.T.	(e)	646	0.37	115.4	2	1.3	1.2	0.5	3	5400	1.55	0.34	0.11	2.1
		646	0.37	115.4	2	1.3	1.2	0.5	3	5400	1.55	0.34	0.23	4.4
		646	0.37	115.4	2	1.3	1.2	0.5	3	5400	1.55	0.34	0.31	6

Tab. 2.1: Choice of the parameters for the turbomachinery, flight and wind-tunnel (W.T.) cases.

2.4.2 Evolution of nonlinear compressible streaks

As anticipated on the basis of the linear analysis by Ricco and Wu (2007), free-stream disturbances of the hydrodynamic kind (i.e. convected gusts) generate thermal fluctuations inside the boundary layer due to the velocity-temperature coupling. Just as the temperature profile affects the stability of a two-dimensional flow (Lees, 1947; Mack, 1975), thermal streaks are bound to influence the secondary instability of the streaky boundary layer. We will therefore focus on the fluctuations of the streamwise velocity and temperature inside the boundary layer.

The overall intensity of the streak signature, which comprises all the harmonics in the nonlinear regime, is measured by the root mean square (r.m.s. hereinafter) of the fluctuating quantity, defined as

$$q_{rms} \equiv r_t \sqrt{\sum_{m=-\bar{N}_t}^{\bar{N}_t} \sum_{n=-\bar{N}_z}^{\bar{N}_z} |\hat{q}_{m,n}|^2}, \quad m \neq 0, \tag{2.63}$$

where the variable q may stand for the streamwise velocity or the temperature and $\bar{N}_t{=}(N_t-1)/2$, $\bar{N}_z{=}(N_z-1)/2$. The downstream development of the maximum q_{rms} along η,

$$q_{rms,max}(\bar{x}) = \max_{\eta} q_{rms}(\bar{x}, \eta),$$

is shown in figures 2.6 (turbomachinery case), 2.7 (flight case) and 2.8 (wind tunnel case), where the nonlinear solutions are compared with the correspondent linearized approximations for different values of Tu. In the linear case, the peak of the r.m.s. is given by

$$q_{rms,max} = \epsilon\sqrt{2}(k_z/k_x)\sqrt{|u_{z,w,+}|^2 + |u_{z,w,-}|^2}\, \max_{\eta} |\bar{q}_l(\bar{x}, \eta)|, \tag{2.64}$$

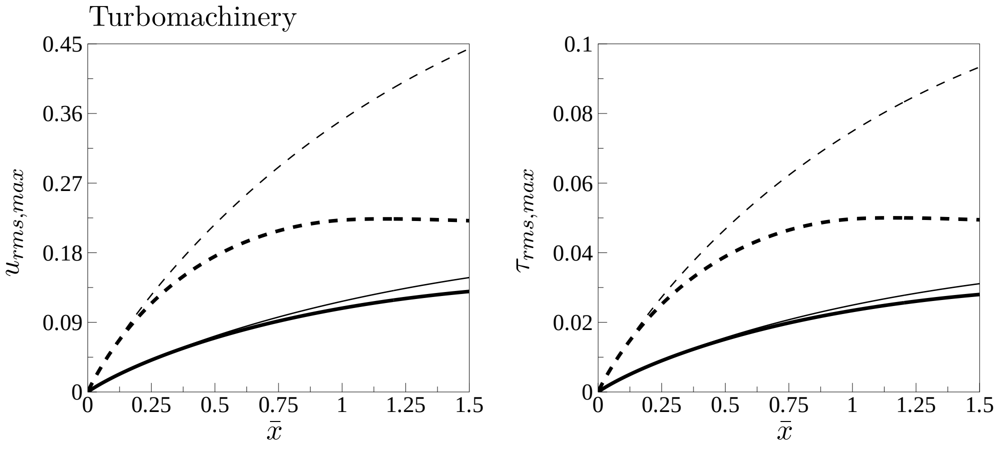

Fig. 2.6: Evolution of the maximum r.m.s. of the streamwise velocity and the temperature for different values of the turbulent Reynolds number: r_t=2.7 (solid lines), r_t=7.9 (dashed lines) at M_∞=0.69 (refer to table 2.1(a)). Thick lines: nonlinear solutions, thin lines: linearized solution.

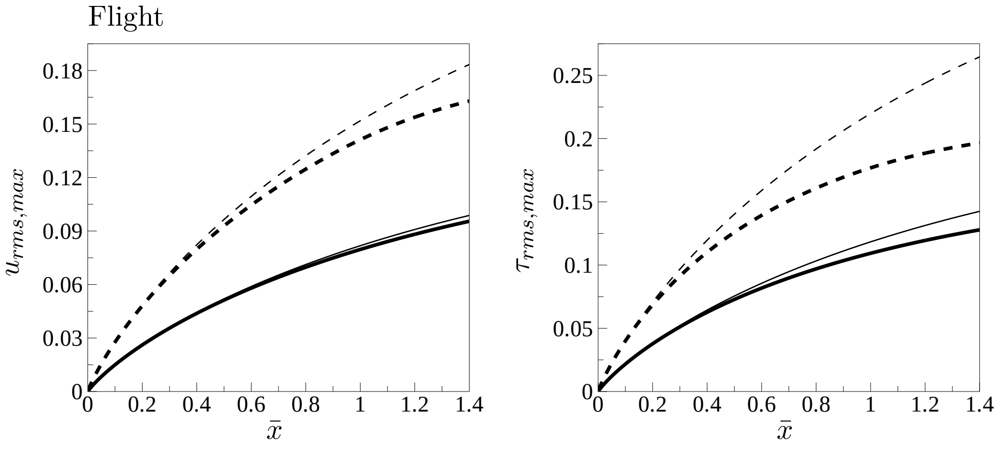

Fig. 2.7: Evolution of the maximum r.m.s. of the streamwise velocity and the temperature for different values of the turbulent Reynolds number: r_t=3.37 (solid line), r_t=6.25 (dashed lines) at M_∞=3 (refer to table 2.1(d)). Thick lines: nonlinear solutions, thin lines: linearized solution.

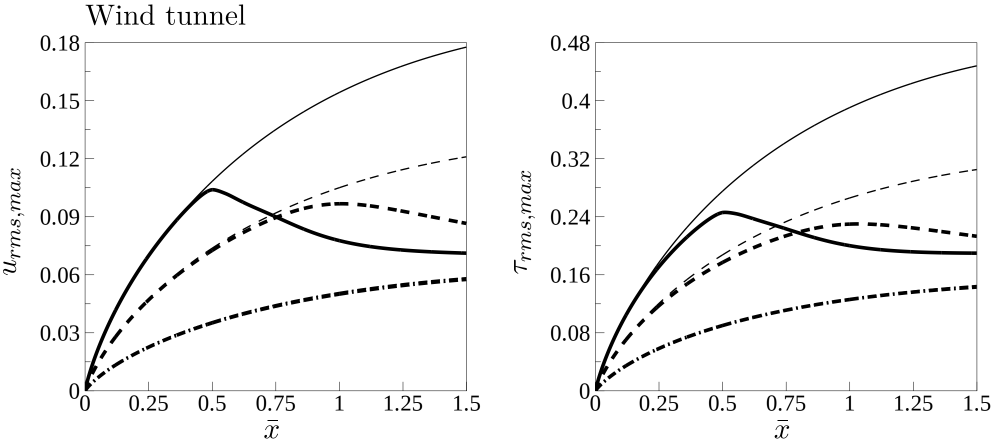

Fig. 2.8: Evolution of the maximum r.m.s. of the streamwise velocity and temperature for different value of the turbulent Reynolds number: r_t=2.1 (dashed-dotted lines), r_t=4.4 (dashed lines), r_t=6 (solid lines) at M_∞=3 (refer to table 2.1(e)). Thick lines: nonlinear solutions, thin lines: linearized solution.

where $\bar{q}_l$ represents the solution provided by Ricco and Wu (2007). Since $|u_{z,w,+}|$ =$|u_{z,w,-}|$=$|u_{z,w}|$, (2.64) simplifies to:

$$q_{rms,max} = 2\epsilon(k_z/k_x)|u_{z,w}| \max_{\eta} |\bar{q}_l(\bar{x}, \eta)|.$$

Sufficiently upstream, the linear and nonlinear solutions overlap as the influence of nonlinearity is still weak. Due to the continued amplification of the disturbance, the streak signature becomes stronger and the linear and nonlinear solutions start diverging for moderate r_t. In the case with the lowest r_t for all the three scenarios considered, the linear and nonlinear curves are almost indistinguishable. In the cases with higher r_t, a stabilizing effect of nonlinearity is observed on the streamwise velocity and temperature and, as the turbulence intensity increases, the attenuation of the disturbances is enhanced. The higher the turbulence level is, the slower and the weaker the disturbance growth becomes, and the farther upstream the nonlinear effects start asserting their influence. The stabilizing effect of nonlinearity was already observed by Ricco *et al.* (2011) in the incompressible regime for high turbulence levels. Here, it is shown that nonlinear effects play the same role on thermal (temperature) streaks.

For the turbomachinery case (figure 2.6), the attenuation of the streaks is more pronounced than in flight conditions as the turbulence levels are higher, and the deviation of the kinematic and thermal streaks from the linearized solution is of similar magnitude. The kinematic fluctuations are about one order of magnitude higher than the thermal streaks relatively to the correspondent free-stream mean velocity and temperature.

In flight conditions (figure 2.7), because of a higher Mach number, the temperature fluctuation acquires a large intensity, which is comparable with that of the velocity fluctuation. Although the influence of Tu on the streamwise velocity is quite weak even in the highest turbulence intensity case, r_t=6.25, appreciable attenuation of the nonlinear thermal streaks with respect to the linearized ones is observed. The stabilizing effect is more marked on the temperature than on the streamwise velocity. The nonlinear and linear r.m.s. of the temperature streaks diverge farther upstream than the r.m.s. of the streamwise velocity. Even for a low-disturbance environment such as free flight, it seems necessary to describe the formation and amplification of the streaks correctly by taking into account the nonlinear interactions inside the boundary layer.

In the wind tunnel case shown in figure 2.8, a peculiar behavior of the nonlinear curve for the highest turbulence level case is observed. A sharp deviation of the nonlinear solution from the linear one occurs at $\bar{x}\approx 0.5$, which corresponds to a physical downstream position of $x^*\approx 10$ cm. This phenomenon was not observed in the incompressible cases studied by Ricco *et al.* (2011). The parameters used in this case are very similar to those of the flight case with highest r_t (refer to tables 2.1(d) and 2.1(e)), except that k_x is about half of that in the flight case. As a consequence, the effect of nonlinearity is stronger. The streamwise

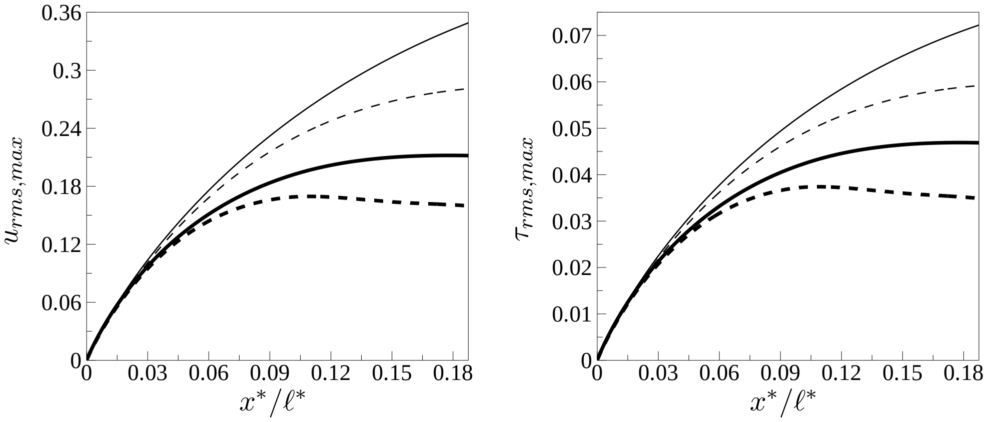

Fig. 2.9: Evolution of the maximum r.m.s. of the streamwise velocity and the temperature for different streamwise wavenumber: k_x=0.0036 (solid lines) and k_x=0.0142 (dashed lines) at M_∞=0.69 (refer to table 2.1(b)). Thick lines: nonlinear solutions, thin lines: linearized solution.

wavenumber of the wind-tunnel case is comparable with that of the flight case with M_∞=6 (refer to table 2.1(c)) but r_t is smaller and M_∞ is higher in the latter, thus resulting into weaker nonlinear effects. Additional calculations suggest that this abrupt change occurs when a sufficiently small streamwise wavenumber is employed, i.e. $k_x \leq 1.5 \times 10^{-3}$, together with a high turbulent Reynolds number, $r_t \geq 6$, at supersonic speed. In the subsonic regime no such sharp deviation was observed, even at high r_t.

The effect of the frequency is displayed in figure 2.9, where the downstream evolutions of $u_{rms,max}$ and $\tau_{rms,max}$ are plotted for different values of k_x in the turbomachinery case (refer to table 2.1(b)). The fluctuations of the streamwise velocity and temperature are higher for smaller k_x, but the dependence of the stabilizing effect of nonlinearity on the frequency is very weak and it is the same for the streamwise velocity component and the temperature. For $k_x \geq 0.01$ the amplitude saturates at an almost constant value before decaying farther downstream.

Figure 2.10 displays the signature of the streamwise velocity and tempera-

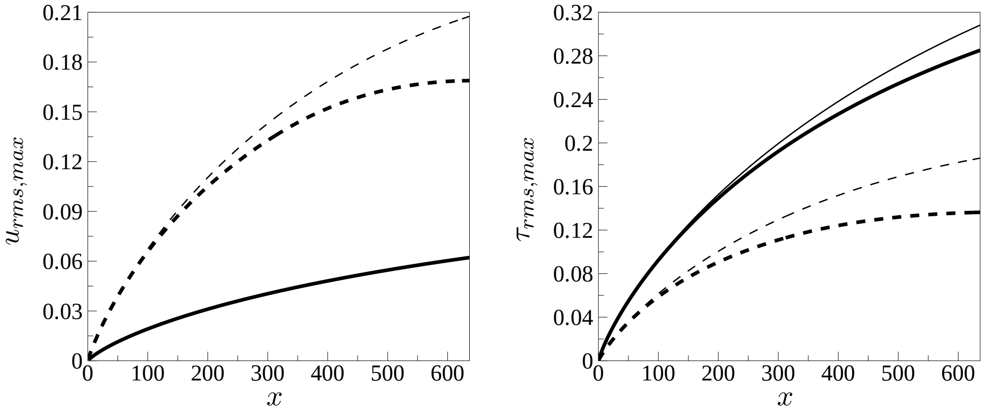

Fig. 2.10: Evolution of the maximum r.m.s. of the streamwise velocity and the temperature for different free-stream Mach number: M_∞=2 (dashed lines), M_∞=6 (solid lines). The turbulent Reynolds number is r_t=4.8 (refer to table 2.1(c)). Thick lines: nonlinear solutions, thin lines: linearized solution.

ture for different Mach numbers in the flight case (refer to table 2.1(c)). The variation of M_∞ is only due to a variation of U^*_∞, while T^*_∞ is constant. As the Mach number increases the r.m.s. of the streamwise velocity is attenuated while the temperature fluctuations are intensified. For M_∞=6, the latter acquire an intensity as large as 26% of T^*_∞, whereas the velocity fluctuations merely reach 5% of U^*_∞. The result suggests that thermal streaks are likely to be primarily responsible for secondary instability in high speed flows. Figure 2.10 also shows that the attenuation effect on the velocity is stronger than the enhancement of the temperature. For example, tripling the Mach number from 2 to 6 results in a decrease of more than three times in the r.m.s. of the streamwise velocity and an increase of twice in the temperature signature at x=600. Despite r_t being the same, for higher M_∞ the stabilizing effect of nonlinearity becomes less pronounced and this is more evident for the streamwise-velocity r.m.s., whose nonlinear evolution is indistinguishable from the linearized curve in the highest M_∞ case. This behavior is attributed to the turbulence level being smaller for higher values of the free-stream velocity, although r_t is the same in all the cases

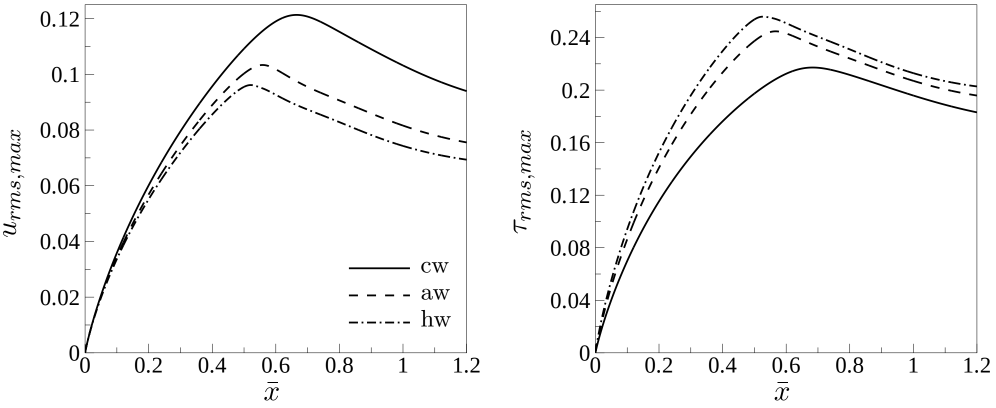

Fig. 2.11: Evolution of the maximum r.m.s. of the streamwise velocity and the temperature for different wall-temperature conditions: hot wall (hw), adiabatic wall (aw) and cold wall (cw) at M_∞=3.

considered.

In figure 2.11 the results obtained in the wind-tunnel case with r_t=6 for the hot-wall condition T^*_w/T^*_{ad}=1.1 are compared with those relative to a cold-wall condition T^*_w/T^*_{ad}=0.8 and an adiabatic temperature at the wall T^*_w=T^*_{ad}. As the wall-heat flux increases from negative (heating), to zero (adiabatic) and to positive (cooling), the signature of the streamwise-velocity is enhanced while the temperature disturbance is attenuated. The position where the abrupt deviation occurs moves from $\bar{x}\approx0.5$ in the hot-wall case to $\bar{x}\approx0.7$ in the cold-wall case. Therefore the wall-heat flux influences the position where the onset of the stabilizing effect due to nonlinearity occurs. This suggests that the employment of the adiabatic-wall condition in wind-tunnel experiments may lead to an inaccurate prediction of the transition location for high-Mach-number supersonic flight conditions, where wall-cooling usually needs to be deployed for thermal protection.

2.4.3 Wall-normal profiles of the perturbation for flight condition

The wall-normal profiles of the streamwise velocity and the temperature are now examined for flight conditions with M_∞=3 and r_t=4.8, as this case features significant effects of nonlinearity and compressibility, whereas in the turbomachinery case compressible effects are weak. The parameters correspond to case (d) in table 2.1, except that Tu=0.27% and r_t=4.8. The flow is symmetric with respect to the z direction because the Fourier forcing modes have opposite spanwise wavenumbers but equal amplitude. Therefore, results will only be presented for modes with $n{\geq}0$, since modes (m, n) and $(m, -n)$ have the same amplitude and shape.

Figure 2.12 shows the profiles of the spanwise-uniform time-averaged flow distortion $(0, 0)$, the forcing mode $(-1, 1)$, and the second and third harmonics with $|m|{=}|n|$, i.e. $(-2, 2)$ and $(-3, 3)$, at $\bar{x}$=0.5 and 1.2. As expected, the forcing mode has a higher amplitude than the other components The mean-flow distortion makes a significant contribution to the overall flow. The magnitude of the higher harmonics decreases so quickly that the third harmonic becomes almost negligible. The profiles of the temperature perturbation are similar to those of the streamwise velocity and evolve in a similar manner, but the amplitude of the thermal fluctuations is slightly higher than those of the streamwise velocity (relatively to the free-stream values).

The streamwise velocity and temperature of the seeded modes attain their respective maxima at η=1.5 and η=2. The most pronounced peak of the second harmonic occurs at a larger wall-normal distance, η=3. The mean-flow distortion of the streamwise velocity is positive near the wall and negative for $\eta{>}2$, while the temperature profile $(0, 0)$ is negative close to the plate (excluding a small positive region at $\eta{<}0.5$) and positive in the outer layer. The $(0, 0)$ components of the streamwise velocity and temperature grow significantly with the downstream

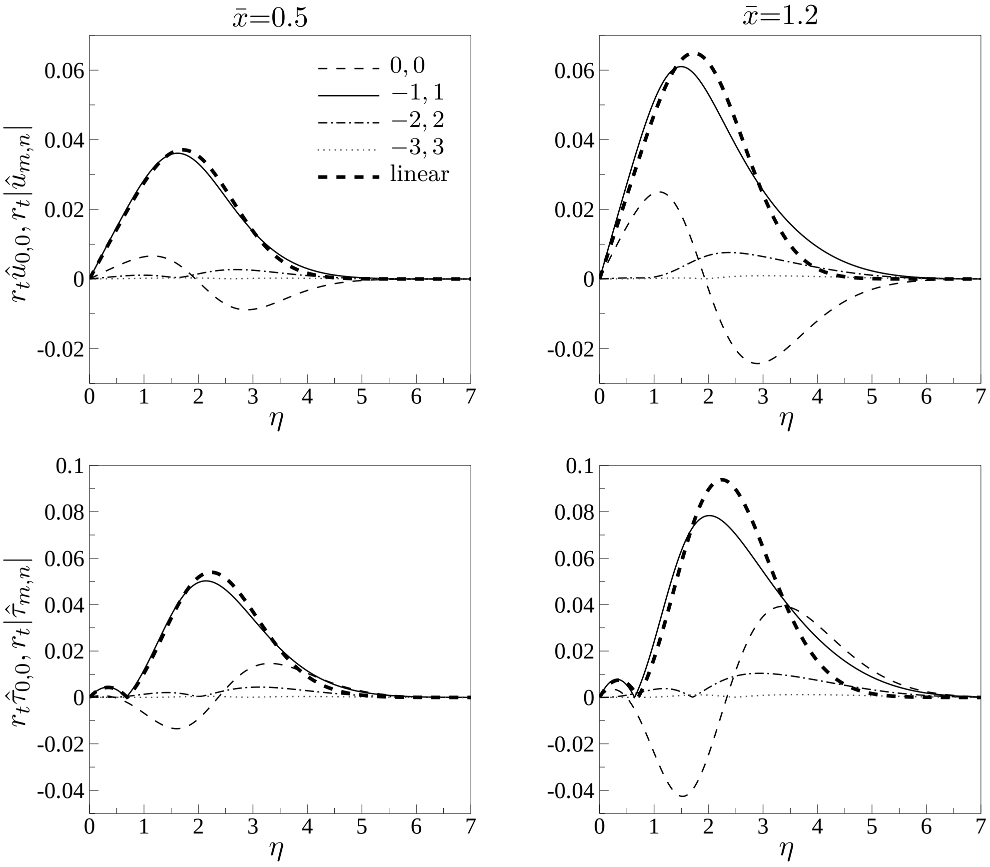

Fig. 2.12: Profiles of the streamwise velocity (first row) and the temperature (second row) of the mean-flow distortion and harmonics with $|m|$=$|n|$=1, 2, 3 at $\bar{x}$=0.5 (first column) and $\bar{x}$=1.2 (second column). The parameters correspond to the flight case with M_∞=3 and r_t=4.8.

distance and their amplitudes become greater than that of the seeded modes in the outer portion of the boundary layer, η>4. The difference between the maximum values of the linear and nonlinear profiles is larger for the temperature than for the streamwise velocity. This confirms the stronger effect of nonlinearity on temperature for high-speed flows, which was already observed in figure 2.7. At $\bar{x}$=0.5 the linear solution of $r_t|\hat{u}_{-1,1}|$ and $r_t|\hat{\tau}_{-1,1}|$ are almost indistinguishable from their nonlinear counterparts. At $\bar{x}$=1.2 the peaks of $r_t|\hat{u}_{-1,1}|$ and $r_t|\hat{\tau}_{-1,1}|$ in the nonlinear case have moved closer to the wall and have decreased in comparison to the linear case. After reaching their maxima, the nonlinear solutions decay more slowly and become larger than the linearized approximations in the outer region of the boundary layer. The mean-flow distortion acquires an amplitude comparable with that of the seeded modes. Therefore, the effect of nonlinearity is to move the location of the disturbance peaks nearer to the wall, to weaken the fluctuations in the core of the boundary layer while enhancing them close to the free stream, and most notably to generate significant mean-flow distortion.

As was pointed out by Ricco (2006), the nonlinear interactions generate only Fourier modes with m=n when the flow is forced by a single free-stream mode, while in the case of a pair of oblique free-stream modes additional components with m≠n are induced. The nonlinearly generated modes are those with $|m|+|n|$ equal to an even integer, i.e. they are arranged as a checkerboard in spectral space. Those generated at the second and third orders are displayed in figure 2.13 at the downstream locations $\bar{x}$=0.5 and 1.2. The amplitudes of the components $(-2,0)$ and $(0,2)$ are comparable with each other but about three times smaller than that of the mean-flow distortion $(0,0)$. At $\bar{x}$=0.5, the peak positions and the magnitudes of the modes $(-2,0)$ and $(0,2)$ are very similar (or almost identical for η>2), while at $\bar{x}$=1.2 the first peak of the mode $(-2,0)$ becomes much higher than that of the component $(0,2)$, and the second peak moves fur-

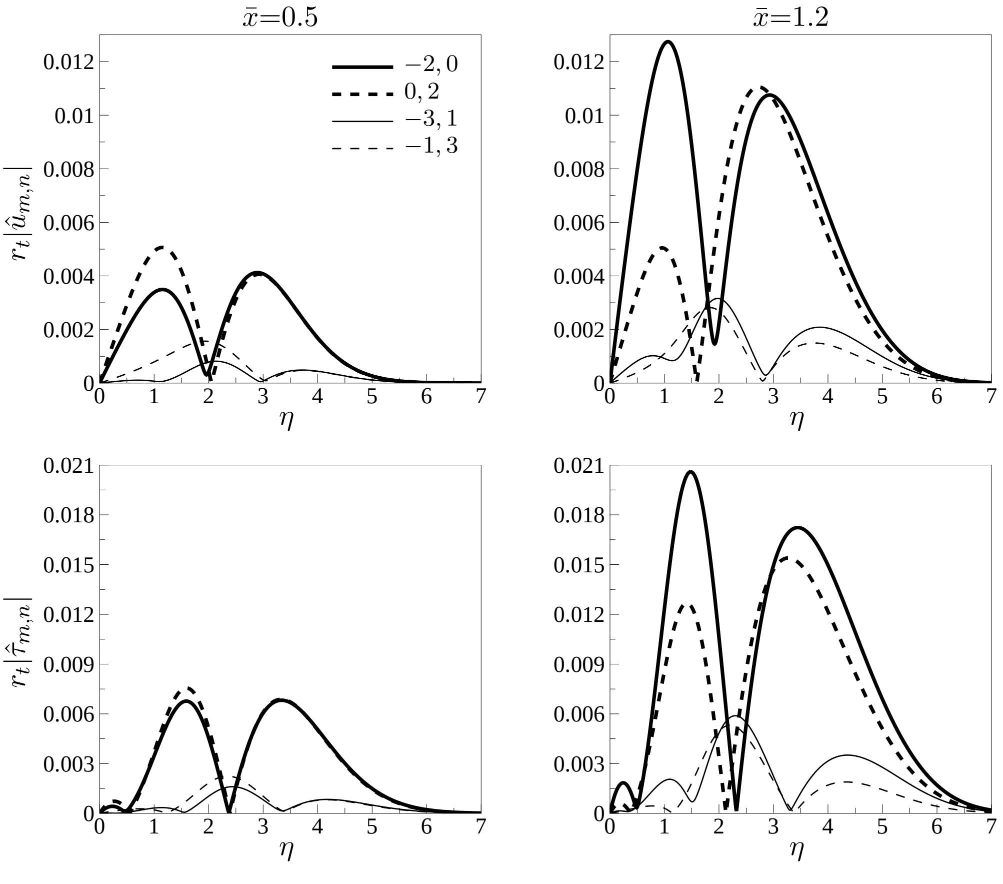

Fig. 2.13: Profiles of the streamwise velocity (first row) and the temperature (second row) of harmonics with $m \neq n$ at $\bar{x}$=0.5 (first column) and $\bar{x}$=1.2 (second column). The parameters correspond to the flight case with M_∞=3 and r_t=4.8.

ther from the wall. The third-order harmonics feature two or three humps, with the first or second peak being coincident with the valley of the second-order components. Profiles with three peaks were not observed in the incompressible case (Ricco *et al.*, 2011) and they are more evident in the temperature streaks.

The profiles of the cross-flow velocity components and of the pressure are displayed in figure 2.14. No mean spanwise velocity component is generated because the disturbances are symmetric with respect to the plane z=0. The profiles of $\hat{v}_{m,0}$ asymptotically approach a constant value (with respect to η) in the free stream, as the right-hand side of (2.61) is a function of $\bar{x}$ only. The amplitudes of the wall-normal and spanwise velocity components are much smaller than that of the streamwise velocity, as $\sqrt{k_x/R_\lambda}=\mathcal{O}(10^{-4})$ and $k_x/k_z=\mathcal{O}(10^{-3})$.

The pressure fluctuations at the wall are analyzed in order to show that these do not represent an aeroelasticity problem. The root-mean-square of the wall pressure is calculated and transformed in dimensional terms by multiplying it by $\rho^*_\infty U^{*2}_\infty$, where U^*_∞=888 ms^{-1} (table 2.1(d)) and ρ^*_∞=0.09kgm^{-3} at 20 km altitude (Champion *et al.*, 1985). The value obtained p^*_{rms}=0.055 Pa is compared to the pressure difference on the wing. The latter is derived from the lift coefficient C_l, which is evaluated using the supersonic linearized theory (refer to Anderson, 2007, equation (12.23)) and assuming an angle of attack equal to 10°. The resulting pressure difference Δp^*=4200 Pa is five orders of magnitude higher than the pressure oscillations obtained in our calculations. A comparison is also performed with the wall-pressure oscillations in a turbulent boundary layer for the same set of parameters. The experimental data provided by Tsuji *et al.* (2007), who measured the r.m.s. of the wall pressure at different friction Reynolds number R_τ, are used to evaluate the p_{rms} at the wall at the current friction Reynolds number $R_\tau \equiv u^*_\tau x^*/\nu^*_\infty$, where u^*_τ is the friction velocity and x^* is the distance from the leading edge. From our calculations we obtain u^*_τ=13 ms^{-1} and we choose

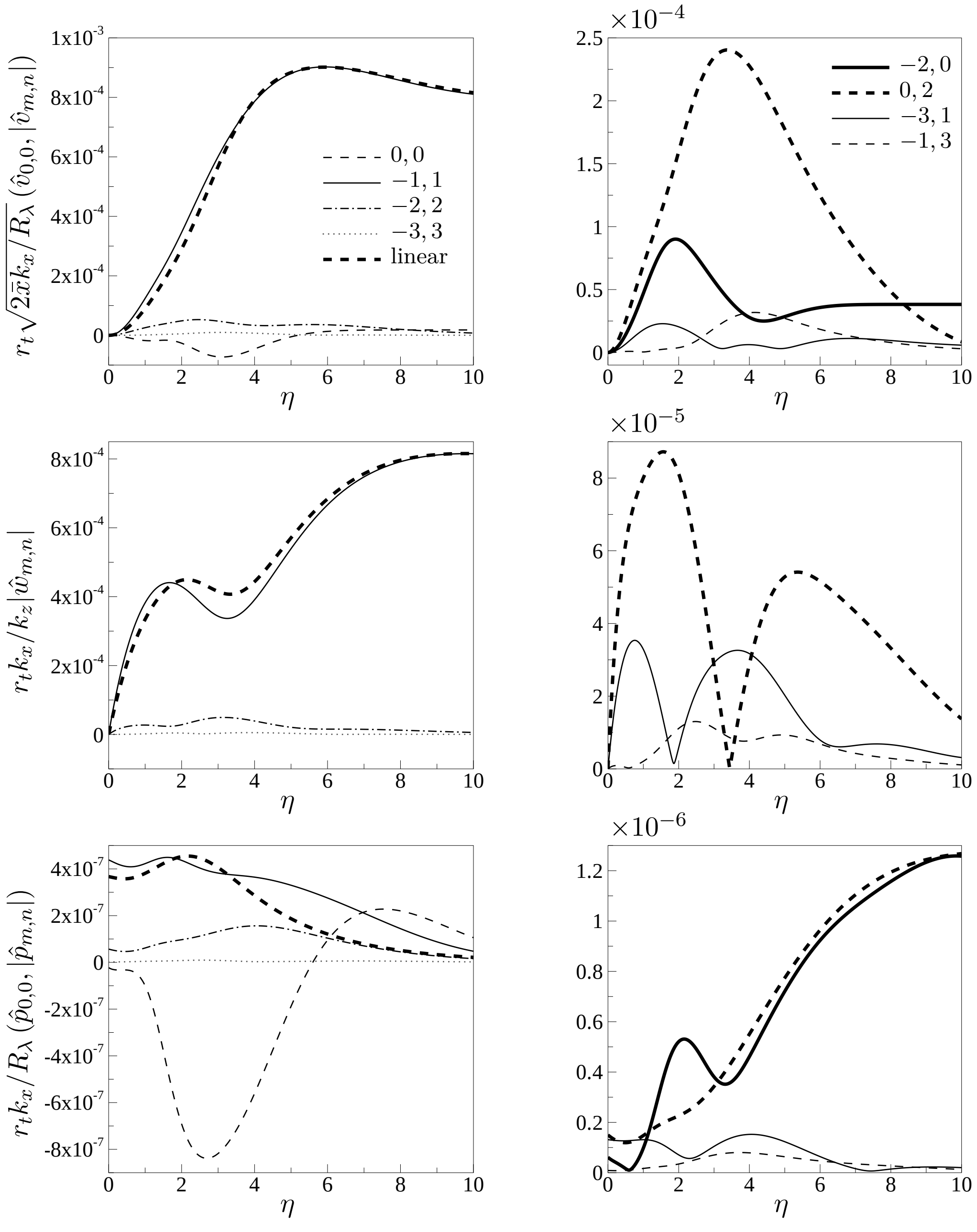

Fig. 2.14: Profiles of the wall-normal velocity (first row), spanwise velocity (second row) and the pressure (third row) of the mean-flow distortion and harmonics at $\bar{x}$=1.2. The parameters correspond to the flight case with M_∞=3 and r_t=4.8.

x^*=0.7 m corresponding to $\bar{x}$=1.2. It follows that R_τ=3.4 × 10^4. The relation proposed by Farabee & Casarella $(p^+_{rms})^2$=6.5 + 1.86 ln$(R_\tau/333)$ is employed to extrapolate the wall-pressure r.m.s. p^+_{rms} scaled with inner viscous units. The experiments of Tsuji *et al.* (2007) refer to an incompressible boundary layer and therefore the effect of the Mach number on the wall pressure needs to be included in our calculations. As a first estimate, the effect of compressibility on the skin-friction coefficient C_f is evaluated by means of figure 19.1 of Schlichting and Gersten (2000) and the same ratio $C_f(M_\infty{=}3)/C_f(M_\infty{=}0)$=0.6 is assumed to be valid for the wall pressure. It follows that p^*_{rms}=35Pa and therefore the ratio between the wall-pressure turbulent and pre-transitional fluctuations is about 6 × 10^2.

The total time-averaged (m=0) streaks of the streamwise velocity and temperature, which will be referred to as u_{str} and τ_{str}, are defined as

$$\{u_{str}(\bar{x},\eta,z),\tau_{str}(\bar{x},\eta,z)\} = r_t \sum_{n=-\bar{N}_z}^{\bar{N}_z} \{\hat{u}_{0,n},\hat{\tau}_{0,n}\}\, e^{ink_z z},$$

in which only modes with n=0, 2, 4, ... provide a non-zero contribution, but the component (0, 4) is almost negligible. They represent a time-averaged spanwise modulation superimposed onto the Blasius boundary layer.

Figure 2.15 shows the contours of the time-averaged streamwise velocity and the temperature streaks plotted in the $\eta - z$ plane at different downstream locations. A positive value of the contours means that the mean flow is higher than the local Blasius solution, while a negative value means that it is lower. Therefore, near the wall the flow is accelerated and cooled, while close to the free stream it is decelerated and heated. The mean-flow distortion of the streamwise velocity has been interpreted as an increase of the mean wall shear stress and backward jets at the edge of the boundary layer, both of which have been observed in experiments (Ricco *et al.*, 2011).

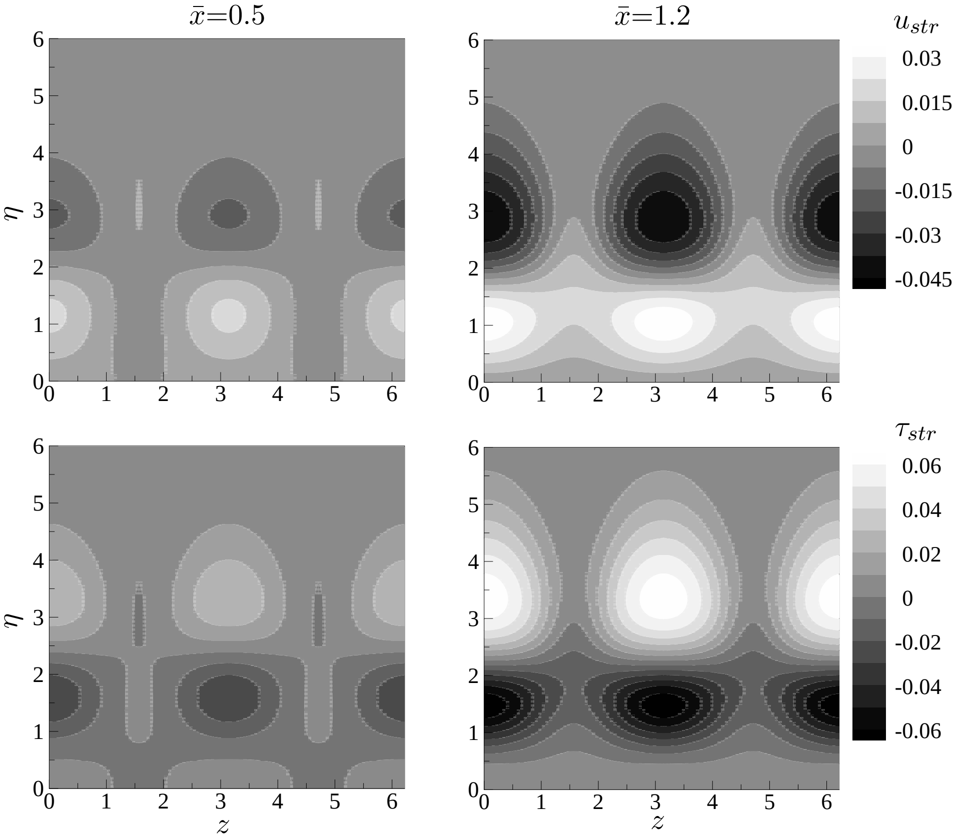

Fig. 2.15: Contours of the time-averaged streamwise velocity streaks u_{str} (first row) and the temperature streaks τ_{str} (second row) in $\eta - z$ plane, at different downstream locations: $\bar{x}$=0.5 (first column), $\bar{x}$=1.2 (second column). The parameters correspond to the flight case with M_∞=3 and r_t=4.8.

2.5 Summary

This chapter investigated the nonlinear response of a compressible boundary layer to free-stream unsteady vortical fluctuations of the convected-gust type. Attention is focused on the low-frequency and long-streamwise components of the disturbances because these penetrate the most into the core of the boundary layer to form kinematic and thermal streaks (or Klebanoff modes). Thanks to this assumption, the mathematical framework of the compressible boundary-region equations (i.e. the Navier-Stokes equations with the streamwise derivative being neglected in the pressure and viscous terms) can be employed. The free-stream perturbation is assumed to be sufficiently strong that the amplitude of the induced streaks is comparable with the mean flow. Nonlinear effects must therefore be taken into account. The previous works by Ricco and Wu (2007) and Ricco *et al.* (2011) were extended to take into account both compressibility and nonlinear effects.

The boundary-layer displacement effect influences the outer-flow solution at leading order, that is, nonlinear interactions within the boundary layer generate a spanwise-independent flow, which drives an unsteady two-dimensional flow of acoustic nature in the outer inviscid region. The analysis shows that the displacement-induced part of the outer perturbation assumes different forms depending on the regime being subsonic or supersonic. Thanks to the well-known analogy with the flow over a thin oscillating airfoil, analytical linearized solutions in the subsonic and supersonic cases are derived. This analogy is used here for the first time to study unsteady boundary layers. In the subsonic regime the disturbances propagate in all directions from the plate, while at supersonic speeds the fluid ahead of the body remains undisturbed and the perturbations are confined within the Mach dihedron.

An initial-boundary-value problem, comprising the nonlinear unsteady compressible boundary-region equations and appropriate upstream and far-field conditions, is presented to study the formation and evolution of the streaks. It is shown that nonlinear interactions inside the boundary layer generate higher harmonics and a significant mean-flow distortion. Kinematic and thermal streaks arise, which represent an unsteady spanwise modulation of the velocity and temperature superimposed onto the Blasius boundary layer. Near the wall the new mean streamwise velocity is higher than the local Blasius value, while the temperature profile exhibits a deficit with respect to the Blasius solution. At the edge of the boundary layer the flow is instead decelerated and heated. Nonlinearity attenuates the fluctuations of the streamwise velocity, and a similar stabilizing effect on the temperature is identified. The effect of the free-stream Mach number is also investigated: as the Mach number increases, the streamwise velocity fluctuations are inhibited, while the temperature ones are enhanced. At supersonic speeds a sharp deviation of the nonlinear solution from its linearized counterpart is observed when a sufficiently small streamwise wavenumber is combined with a high turbulence level. The present investigation provides an accurate signature of nonlinear compressible streaks which is indispensable for the secondary instability analysis of the unsteady streaky boundary layer.

3. NONLINEAR UNSTEADY GÖRTLER VORTICES EXCITED BY FREE-STREAM VORTICAL DISTURBANCES

In the previous chapter the nonlinear boundary-region equations have been employed to describe the nonlinear response of a compressible boundary layer to free-stream vortical fluctuations. Wu *et al.* (2011) showed that in the boundary-layer over a concave wall with a suitable curvature unsteady streaks acquire the character of Görtler rolls. The mathematical framework of the boundary-region equations was employed by Wu *et al.* (2011) to study both the receptivity process and the linear evolution of the induced disturbance. When the free-stream turbulence level is high, Görtler vortices evolve nonlinearly. The focus of this chapter is on the generation and nonlinear development of unsteady Görtler rolls in an incompressible boundary layer subject to medium-intensity free-stream vorticity. The analyses of Ricco *et al.* (2011) and Wu *et al.* (2011) are extended to account for both the centrifugal forces due to the concavity of the wall and the nonlinear effects. In §3.1 we formulate the boundary-region problem through the relevant governing equations (§3.1.1) and boundary conditions (§3.1.2), and outline the numerical procedures. The results are presented in §3.2 for the set of parameters described in §3.2.1. A low free-stream turbulence-intensity case is first considered (§3.2.2), for which the effects of turbulence level, frequency and Görtler number are studied. In §3.2.3 results are presented for an increased free-stream disturbance amplitude. The growth rates and the wall-normal profiles of the induced boundary-layer perturbations are discussed in §3.2.4 and §3.2.5, respectively. A comparison with experimental data and DNS is carried out in §3.2.6. A brief summary and concluding remarks are provided in §3.3.

3.1 Mathematical formulation and numerical procedures

The boundary-layer flow over a longitudinally concave wall is considered. The radius of curvature r_0^* is assumed to be constant. Hereinafter the superscript * indicates dimensional quantities. An incompressible flow with mean uniform speed U_∞^* encounters the curved surface. The oncoming mean flow is perturbed by unsteady vortical fluctuations of the convected-gust type.

The fluid motion is described in an orthogonal curvilinear coordinate system $\{x^*, y^*, z^*\}$, where x^* represents the distance from the leading edge, y^* measures the normal distance to the wall and z^* is the spanwise coordinate normal to the plane formed by x^* and y^*. The problem is formulated in non-dimensional terms by introducing a suitable reference length scale $\lambda^*{=}1/k_z^*$, where k_z is the spanwise wavenumber of the oncoming gust. It follows that $k_z{=}1$, but, for clarity, the dependence on k_z will be expressed explicitly henceforth, unless otherwise specified. The velocity components are scaled with U_∞^*. The time t^* and the pressure p^* are normalized by λ^*/U_∞^* and $\rho_\infty^* U_\infty^{*2}$, respectively, where ρ^* is the (constant) density of the fluid.

As in §2.1.1, we consider the simplified case where the boundary layer is forced only by a pair of vortical modes with the same frequency f^* (and hence streamwise wavenumber k_x^*), but opposite spanwise wavenumber $\pm k_z^*$. The free-stream perturbation $\mathbf{u}_\infty$ is passively convected by the mean flow and is represented by (2.3). The Reynolds number is defined as $R_\lambda{\equiv}U_\infty^*\lambda^*/\nu^*$, where ν^* is the kinematic viscosity of the fluid, and it is assumed to be asymptotically large.

In the case of a flat plate, experiments have confirmed that the low-frequency components of the free-stream perturbation (i.e. $k_x{\ll}1$) penetrate into the boundary layer to form Klebanoff modes. Wu *et al.* (2011) showed that in the case of a concave plate with a suitable curvature, streaks develop into Görtler vortices at $x^*=\mathcal{O}(\lambda_x^*)$, after attaining their maximum amplitude. Therefore, the slowly varying streamwise and time variables $\bar{x}=k_x x=\mathcal{O}(1)$ and $\bar{t}=k_x t=\mathcal{O}(1)$ are introduced. At $x=\mathcal{O}(R_\lambda)$, the local boundary-layer thickness δ^* becomes comparable with λ^*. It follows that $k_x R_\lambda=\mathcal{O}(1)$, or, equivalently, $\kappa\equiv k_z/(k_x R_\lambda)=\mathcal{O}(1)$. In the analysis of Wu *et al.* (2011), the streamwise coordinate and the time are scaled with R_λ^{-1}, i.e. $\hat{x}=R_\lambda^{-1}x$ and $\hat{t}=R_\lambda^{-1}t$ which are of the same order as $\bar{x}$ and $\bar{t}$ and are well defined in the limit $k_x\to 0$. Since our formulation closely follows that of Ricco *et al.* (2011) and the steady limit is not considered, it is convenient to adopt the scaling with the variables $\bar{x}$ and $\bar{t}$. In the flat-plate case, the disturbance in the downstream viscous region where $\bar{x}=\mathcal{O}(1)$ is governed by the boundary-region equations. In the limit $\kappa\to 0$ the pressure disturbance vanishes from the equations, so that the wall-normal momentum equation is no longer needed and the boundary-layer equations are recovered. For a curved plate, the terms which account for the centrifugal effects appear in the y-momentum equation. Therefore, we assume $\kappa=\mathcal{O}(1)$ throughout the chapter and the limit $\kappa\to 0$ is not considered.

The free-stream perturbation is taken to be sufficiently high to produce $\mathcal{O}(1)$ streamwise velocity fluctuations within the boundary layer at $\bar{x}=\mathcal{O}(1)$. It follows that the turbulent Reynolds number $r_t\equiv\epsilon R_\lambda=\mathcal{O}(1)$ and the induced disturbance undergoes nonlinear evolution. The asymptotic structure of the flow domain shown in figure 2.1 for the flat-plate case holds for the flow over concave wall.

3.1.1 Governing equations

The equations of motions are derived from the Navier-Stokes equations written in curvilinear coordinates with Lamé coefficients (Floryan and Saric, 1982) $h_1=(r_0-y)/r_0$, $h_2=h_3=1$. The velocity and pressure fields are rescaled as $\{u,v,w,p\}=\{\tilde{u},\sqrt{k_x/R_\lambda}\tilde{v},k_x\tilde{w},k_x\tilde{p}/R_\lambda\}$, and the change of variable $(x,t)\to$

$(\bar{x},\bar{t})$ is performed. By taking the limit $k_x^{-1}, R_\lambda \to \infty$ with $k_x R_\lambda = \mathcal{O}(1)$, at the leading order we obtain

$$\frac{\partial \tilde{u}}{\partial \bar{x}} + \frac{\kappa}{k_z}\frac{\partial \tilde{v}}{\partial y} + \frac{\partial \tilde{w}}{\partial z} = 0, \tag{3.1a}$$

$$\frac{\partial \tilde{u}}{\partial \bar{t}} + \tilde{u}\frac{\partial \tilde{u}}{\partial \bar{x}} + \frac{\kappa}{k_z}\tilde{v}\frac{\partial \tilde{u}}{\partial y} + \tilde{w}\frac{\partial \tilde{u}}{\partial z} = \frac{\kappa^2}{k_z^2}\left(\frac{\partial^2 \tilde{u}}{\partial y^2} + \frac{\partial^2 \tilde{u}}{\partial z^2}\right), \tag{3.1b}$$

$$\frac{\partial \tilde{v}}{\partial \bar{t}} + \tilde{u}\frac{\partial \tilde{v}}{\partial \bar{x}} + \frac{\kappa}{k_z}\tilde{v}\frac{\partial \tilde{v}}{\partial y} + \tilde{w}\frac{\partial \tilde{v}}{\partial z} + \mathcal{G}\tilde{u}^2 = \frac{\kappa^2}{k_z^2}\left(-\frac{\partial \tilde{p}}{\partial y} + \frac{\partial^2 \tilde{v}}{\partial y^2} + \frac{\partial^2 \tilde{v}}{\partial z^2}\right), \tag{3.1c}$$

$$\frac{\partial \tilde{w}}{\partial \bar{t}} + \tilde{u}\frac{\partial \tilde{w}}{\partial \bar{x}} + \frac{\kappa}{k_z}\tilde{v}\frac{\partial \tilde{w}}{\partial y} + \tilde{w}\frac{\partial \tilde{w}}{\partial z} = \frac{\kappa^2}{k_z^2}\left(-\frac{\partial \tilde{p}}{\partial z} + \frac{\partial^2 \tilde{w}}{\partial y^2} + \frac{\partial^2 \tilde{w}}{\partial z^2}\right), \tag{3.1d}$$

where

$$\mathcal{G} = \frac{R_\lambda^{1/2}}{k_x^{3/2} r_0} \tag{3.2}$$

is the Görtler number, which takes into account the effect of the wall curvature. As $\mathcal{G} \to 0$ the incompressible unsteady boundary-region equations for a flat plate are recovered (Kemp, 1951). Due to the different scaling of the streamwise and time variables, our definition of Görtler number differs from that of Wu *et al.* (2011), i.e.

$$G_\lambda = R_\lambda^2 / r_0 = \mathcal{O}(1). \tag{3.3}$$

The relation between $\mathcal{G}$ and G_λ is:

$$\mathcal{G} = \frac{G_\lambda}{\hat{k}_x^{3/2}} = \left(\frac{\kappa}{k_z}\right)^3 G_\lambda. \tag{3.4}$$

As in §2.1.2, the boundary-layer solution is expressed as a superimposition of the perturbation induced by the free-stream disturbance on the Blasius flow, namely

$$\{\tilde{u}, \tilde{v}, \tilde{w}, \tilde{p}\} = \left\{F', \frac{\eta F' - F}{\sqrt{2\bar{x}}}, 0, -\frac{1}{2}\right\} + r_t \left\{\bar{u}\left(\bar{x},\eta,z,\bar{t}\right), \sqrt{2\bar{x}}\bar{v}\left(\bar{x},\eta,z,\bar{t}\right),\right.$$
$$\left. k_z^{-1}\bar{w}\left(\bar{x},\eta,z,\bar{t}\right), \bar{p}\left(\bar{x},\eta,z,\bar{t}\right)\right\}, \tag{3.5}$$

where $\eta \equiv y\sqrt{k_x R_\lambda/(2\bar{x})}$ is the similarity variable and $F(\eta)$ is the Blasius solution (refer to Ricco *et al.*, 2011). The boundary-layer perturbation is decomposed as a Fourier series in time and z,

$$\{\bar{u}, \bar{v}, \bar{w}, \bar{p}\} = \sum_{m,n} \{\hat{u}_{m,n}, \hat{v}_{m,n}, \hat{w}_{m,n}, \hat{p}_{m,n}\}\, e^{im\bar{t}+ink_z z}, \tag{3.6}$$

where $\{\hat{u}_{m,n}, \hat{v}_{m,n}, \hat{w}_{m,n}, \hat{p}_{m,n}\}$ are functions of $\bar{x}$ and η and are real quantities.

By substituting (3.5) and (3.6) into (3.1) and performing the change of variable $(\bar{x}, y) \to (\bar{x}, \eta(\bar{x}, y))$ the nonlinear perturbation equations are derived as

Continuity equation

$$\frac{\partial \hat{u}_{m,n}}{\partial \bar{x}} - \frac{\eta}{2\bar{x}}\frac{\partial \hat{u}_{m,n}}{\partial \eta} + \frac{\partial \hat{v}_{m,n}}{\partial \eta} + in\hat{w}_{m,n} = 0, \tag{3.7}$$

x-momentum equation

$$\begin{aligned} &\left(im - \frac{\eta}{2\bar{x}}F'' + \kappa^2 n^2\right)\hat{u}_{m,n} + F'\frac{\partial \hat{u}_{m,n}}{\partial \bar{x}} - \frac{F}{2\bar{x}}\frac{\partial \hat{u}_{m,n}}{\partial \eta} - \frac{1}{2\bar{x}}\frac{\partial^2 \hat{u}_{m,n}}{\partial \eta^2} + F''\hat{v}_{m,n} \\ &= r_t\hat{\mathcal{X}}_{m,n}, \end{aligned} \tag{3.8}$$

y-momentum equation

$$\begin{aligned} &\left[\frac{1}{4\bar{x}^2}\left(F - \eta F' - \eta^2 F''\right) + \frac{2\mathcal{G}F'}{\sqrt{2\bar{x}}}\right]\hat{u}_{m,n} + \left(im + \frac{\eta}{2\bar{x}}F'' + \frac{F'}{2\bar{x}} + \kappa^2 n^2\right)\hat{v}_{m,n} + \\ &F'\frac{\partial \hat{v}_{m,n}}{\partial \bar{x}} - \frac{F}{2\bar{x}}\frac{\partial \hat{v}_{m,n}}{\partial \eta} - \frac{1}{2\bar{x}}\frac{\partial^2 \hat{v}_{m,n}}{\partial \eta^2} + \frac{1}{2\bar{x}}\frac{\partial \hat{p}_{m,n}}{\partial \eta} = r_t\hat{\mathcal{Y}}_{m,n}, \end{aligned} \tag{3.9}$$

z-momentum equation

$$\left(im + n^2\kappa^2\right)\hat{w}_{m,n} + F'\frac{\partial \hat{w}_{m,n}}{\partial \bar{x}} - \frac{F}{2\bar{x}}\frac{\partial \hat{w}_{m,n}}{\partial \eta} - \frac{1}{2\bar{x}}\frac{\partial^2 \hat{w}_{m,n}}{\partial \eta^2} + in\kappa^2\hat{p}_{m,n} = r_t\hat{\mathcal{Z}}_{m,n}, \tag{3.10}$$

where the nonlinear terms $\hat{\mathcal{X}}_{m,n}$, $\hat{\mathcal{Y}}_{m,n}$ and $\hat{\mathcal{Z}}_{m,n}$ are given by

$$\hat{\mathcal{X}}_{m,n} = \left[-\frac{\partial \widehat{\bar{u}\bar{u}}}{\partial \bar{x}} + \frac{\eta}{2\bar{x}} \frac{\partial \widehat{\bar{u}\bar{u}}}{\partial \bar{\eta}} - \frac{\partial \widehat{\bar{u}\bar{v}}}{\partial \bar{\eta}} - ni\widehat{\bar{u}\bar{w}} \right]_{m,n}, \tag{3.11a}$$

$$\hat{\mathcal{Y}}_{m,n} = \left[-\frac{\widehat{\bar{u}\bar{v}}}{2\bar{x}} - \frac{\partial \widehat{\bar{u}\bar{v}}}{\partial \bar{x}} + \frac{\eta}{2\bar{x}} \frac{\partial \widehat{\bar{u}\bar{v}}}{\partial \bar{\eta}} - \frac{\partial \widehat{\bar{v}\bar{v}}}{\partial \bar{\eta}} - ni\widehat{\bar{v}\bar{w}} - \frac{\mathcal{G}}{\sqrt{2\bar{x}}}\widehat{\bar{u}\bar{u}} \right]_{m,n}, \tag{3.11b}$$

$$\hat{\mathcal{Z}}_{m,n} = \left[-\frac{\partial \widehat{\bar{u}\bar{w}}}{\partial \bar{x}} + \frac{\eta}{2\bar{x}} \frac{\partial \widehat{\bar{u}\bar{w}}}{\partial \bar{\eta}} - \frac{\partial \widehat{\bar{v}\bar{w}}}{\partial \bar{\eta}} - ni\widehat{\bar{w}\bar{w}} \right]_{m,n}. \tag{3.11c}$$

As $\mathcal{G} \to 0$ the unsteady nonlinear boundary-region equations of Ricco *et al.* (2011) are recovered.

Leib *et al.* (1999) showed that for large κ (i.e. $k_x \ll R_\lambda^{-1}$) the linearized unsteady boundary-region (LUBR) equations for a flat plate possess an asymptotic solution of the form:

$$\{\bar{u}, \bar{v}, \bar{w}, \bar{p}\} = \left\{ \kappa^{-2}\hat{u}(\kappa^2\bar{x}, \eta), \hat{v}(\kappa^2\bar{x}, \eta), \hat{w}(\kappa^2\bar{x}, \eta), \hat{p}(\kappa^2\bar{x}, \eta) \right\}. \tag{3.12}$$

This scaling is also valid in the case of a curved plate and is adopted by Wu *et al.* (2011), whose framework holds in the steady limit $k_x \to 0$. By rescaling the velocity and pressure fields as:

$$\{\bar{u}, \bar{v}, \bar{w}, \bar{p}\} = \left\{ u^\dagger(\hat{x}, \eta), \hat{k}_x^{-1} v^\dagger(\hat{x}, \eta), \hat{k}_x^{-1} w^\dagger(\hat{x}, \eta), \hat{k}_x^{-1} p^\dagger(\hat{x}, \eta) \right\}, \tag{3.13}$$

where $\hat{k}_x {=} k_x R_\lambda$ and $\hat{x} {=} \bar{x}/\hat{k}_x {=} x/R_\lambda$, the linear parts of (3.7)-(3.10) are recast into equations (2.15)-(2.18) of Wu *et al.* (2011). In the limit $\kappa \to \infty$, the disturbance field $\left\{u^\dagger, v^\dagger, w^\dagger, p^\dagger\right\}$ is governed by the steady boundary-regions equations. Through the scaling (3.12) the definition of Görtler number (3.3) used in Wu *et al.* (2011) is recovered. Note that $\mathcal{G}{=}\mathcal{O}(1)$ only if $\kappa{=}\mathcal{O}(1)$, which is always the case in the present analysis.

3.1.2 The upstream and outer boundary conditions

The perturbation equations (3.7)-(3.10) must be solved subject to appropriate upstream and free-stream boundary conditions. The latter are obtained by matching the solution inside the boundary layer with the outer solution as $\eta \to \infty$. For the case of a flat plate, the outer-flow solution is derived by Ricco *et al.* (2011). It is shown that the free-stream cross-flow velocity components exert the leading-order forcing on the boundary layer, while the forcing due to the streamwise velocity is of higher order. Far from the plate $\hat{u}_{m,n} \to 0$ and the centrifugal effects due to the wall curvature become negligible. Therefore, the outer boundary conditions are the same as those employed by Ricco *et al.* (2011), namely

$$\{\hat{u}_{m,n}, \hat{v}_{m,n}, \hat{w}_{m,n}, \hat{p}_{m,n}\} \to \left\{0, \frac{\kappa}{k_z\sqrt{2\bar{x}}} v^{\dagger}_{m,n}, \frac{\kappa^2}{k_z} w^{\dagger}_{m,n}, \frac{\epsilon}{k_x} p^{\dagger}_{m,n}\right\} \tag{3.14}$$

as $\eta \to \infty$ for $\bar{x}=\mathcal{O}(1)$, with

$$v^{\dagger}_{m,\pm 1} = -\frac{\kappa}{\kappa_y} e^{-(\kappa_y^2+\kappa_z^2)\bar{x}} \left[\hat{\phi}_m e^{-i(\bar{x}+\kappa_y\sqrt{2\bar{x}}\eta)} + \hat{\phi}^{\star}_{-m} e^{i(\bar{x}+\kappa_y\sqrt{2\bar{x}}\eta)}\right], \tag{3.15a}$$

$$w^{\dagger}_{m,\pm 1} = \pm e^{-(\kappa_y^2+\kappa_z^2)\bar{x}} \left[\hat{\phi}_m e^{-i(\bar{x}+\kappa_y\sqrt{2\bar{x}}\eta)} - \hat{\phi}^{\star}_{-m} e^{i(\bar{x}+\kappa_y\sqrt{2\bar{x}}\eta)}\right], \tag{3.15b}$$

$$p^{\dagger}_{0,\pm 2} = 2e^{-2(\kappa_y^2+\kappa_z^2)\bar{x}}, \tag{3.15c}$$

$$p^{\dagger}_{m,0} = -\frac{2\kappa^2}{\kappa_y^2} e^{-2(\kappa_y^2+\kappa_z^2)\bar{x}} \left[\hat{\pi}_m e^{-2i(\bar{x}+\kappa_y\sqrt{2\bar{x}}\eta)} + \hat{\pi}^{\star}_{-m} e^{2i(\bar{x}+\kappa_y\sqrt{2\bar{x}}\eta)}\right], \tag{3.15d}$$

where $\kappa_y = k_y/\sqrt{k_x R_\lambda}$ and $v^{\dagger}_{m,n} = w^{\dagger}_{m,n} = 0$ if $n \neq \pm 1$, $p^{\dagger}_{m,n} = 0$ if $n \neq 0, \pm 2$. The coefficients $\hat{\phi}_m$ and $\hat{\pi}_m$ are given by equation (2.26) of Ricco *et al.* (2011) and depend on the displacement thickness. The condition on $\hat{v}_{m,n}$ in (3.14) holds only for $n \neq 0$ (refer to §2.1.4 for a brief discussion on this point).

The perturbation equations (3.7)-(3.10) are subject to initial conditions for $\bar{x} \to 0$. As elucidated by Ricco *et al.* (2011) for the flat-plate case, the velocity fluctuations are of small amplitude for $\bar{x} \ll 1$ and hence the perturbation evolves linearly near the leading edge. By applying the same argument to the case of a curved wall, it follows that the forced modes (m,n)=$(1,\pm1)$ are subject to the same upstream conditions employed in the linear analysis of Wu *et al.* (2011). In the latter paper it was shown that since $\bar{u}$→0 as $\bar{x}$→0, the centrifugal terms drop out of the small-$\bar{x}$ equations and hence the initial condition of Leib *et al.* (1999) are recovered, namely

$$\{\hat{u},\hat{v},\hat{w},\hat{p}\}_{-1,\pm1} \rightarrow \frac{i\kappa^2}{k_z}\left(\pm\hat{u}^{\infty}_{z,\pm} + \frac{ik_z}{\sqrt{k_x^2+k_z^2}}\hat{u}^{\infty}_{y,\pm}\right)\{U_{in}, V_{in}, \mp iW_{in}\} \qquad (3.16)$$

as $\bar{x}$→0, where $\{U_{in}, V_{in}, W_{in}\}$ correspond to the right-hand sides of equations (5.25)-(5.27) in Leib *et al.* (1999). For all the other harmonics induced by non-linear effects, the velocity fluctuations are required to vanish upstream. At the wall, the no-slip condition is imposed on the velocity components.

The numerical scheme employed to solve the perturbation equations (3.7)-(3.10) with the far-field boundary conditions (3.14) and the initial conditions (3.16) is analogous to that outlined in §2.2 for the computation of the streaks. The typical grid sizes in the wall-normal and streamwise directions are $\Delta\eta$=0.015 and $\Delta\bar{x}$=0.01 and the transverse domain extends to η_{max}=30. Since Görtler vortices undergo an exponential growth and their amplitude becomes much larger than that of the free-stream disturbances, a higher number of Fourier modes is needed as compared to the study of streaks. It has been verified, through careful resolutions checks, that the non linear effects are accurately captured with N_t=N_z=37 modes. In the linearized case the code has been validated against the results of Wu *et al.* (2011) (refer to Appendix E).

3.2 Results

3.2.1 Parameters

Following Wu *et al.* (2011), the flow parameters are chosen to correspond to those in the experiments of Boiko *et al.* (2010b). Two cases with different frequency, $F_b = 2\pi f^*/U^*_\infty \cdot 10^6$=5.67 (case 1), 12.48 (case 2), and same spanwise wavelength, $\Lambda_b = U^*_\infty \lambda_z^{*^{3/2}}/(\nu^* r_0^{*^{1/2}})$=149, are selected from the latter experiments. The relevant parameters are summarized in table 3.1. The values of G_λ and $\hat{k}_x$ are also reported to facilitate the comparison with the work of Wu *et al.* (2011).

Case	U^*_∞ [ms^{-1}]	λ^*_z [m] $\times 10^3$	r^*_0 [m]	f^* [Hz]	λ^*_x [m]	R_λ	G_λ	$\hat{k}_x$	k_x $\times 10^3$	κ	$\mathcal{G}$
1	9.18	8	8.37	5	1.84	767	89.5	3.336	4.35	0.547	14.7
2	9.18	8	8.37	11	0.83	767	89.5	7.342	9.57	0.369	4.5

Tab. 3.1: Parameters from the experiments of Boiko *et al.* (2010b).

Unless otherwise specified, the scaled amplitudes of the free-stream velocity components are $\hat{u}^\infty_{x,\pm}$=$\hat{u}^\infty_{y,\pm}$=1 and $\hat{u}^\infty_{z,\pm}$=$\mp$1. With this choice of $\hat{\mathbf{u}}^\infty_\pm$, the continuity relation (2.4) becomes $k_x + k_y$=1 and the turbulence level is $Tu(\%)$=$100 \times 2\epsilon\sqrt{(\hat{u}^\infty_{x,+})^2 + (\hat{u}^\infty_{x,-})^2}$=$100 \times 2\sqrt{2}\epsilon$. The experiments of Boiko *et al.* (2010b) were performed at extremely low disturbance amplitudes to guarantee a linear dynamics. We start from a weak free-stream perturbation case and gradually increase the turbulence level to study the dynamics of the unsteady nonlinear Görtler vortices.

3.2.2 Low free-stream turbulence intensity

Effect of turbulence level

The overall intensity of the disturbance inside the boundary layer is measured by the r.m.s. of the streamwise velocity $u_{rms}(\bar{x}, \eta)$, defined in (2.63). The down-

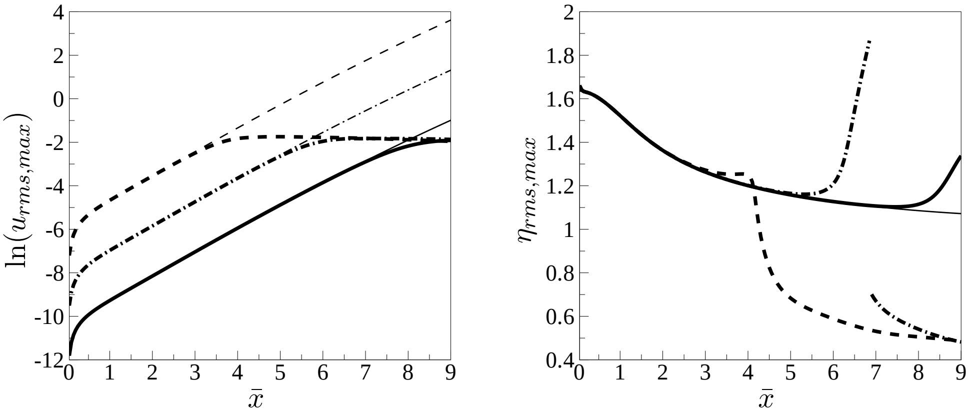

Fig. 3.1: Downstream development of $\ln(u_{rms,max})$ and its associated wall-normal peak $\eta_{rms,max}$ for different turbulent Reynolds numbers: r_t=0.001 (solid line), 0.01 (dash-dotted line), 0.1 (dashed line) at fixed $\mathcal{G}$=14.7 (refer to case 1 in table 3.1). Thin lines: linearized solutions, thick lines: nonlinear solutions.

stream development of $u_{rms,max}(\bar{x})=\max_\eta u_{rms}(\bar{x},\eta)$ is shown in the left graph of figure 3.1 for the parameters of case 1 (refer to table 3.1) at low turbulence intensities, i.e. r_t=0.001, 0.01, 0.1. The nonlinear solutions coincide with the corresponding linearized solutions for a considerable downstream distance from the leading edge. Exponential growth is experienced when the Görtler vortices evolve linearly. Due to the intense amplification of the disturbance, the nonlinear effects come into play quite abruptly to attenuate the velocity fluctuations inside the boundary layer. The nonlinear curves sharply deviate from the linearized counterparts and become almost flat, decreasing very slowly. For higher turbulence level the attenuation of the perturbation is enhanced and the deviation of the nonlinear solution occurs further upstream. The stabilizing effect of nonlinearity was already observed by Ricco *et al.* (2011) for laminar streaks developing over a flat plate and by Hall (1988) for steady Görtler vortices over a concave wall with variable curvature. Sufficiently downstream the nonlinear solutions for different r_t tend to reach the same plateau. Hall (1988) observed a similar phenomenon and suggested that, since the effective spanwise wavenumber is large at large downstream locations, the small-wavelength asymptotic theory of Hall (1982a) becomes valid, i.e. a unique final amplitude solution exists independent of the initial amplitude of the disturbance. This behavior was not detected in the study of the nonlinear Klebanoff modes (Ricco *et al.*, 2011) over a flat plate.

The downstream development of the wall-normal position $\eta_{rms,max}$ where the maximum of the streamwise velocity occurs is shown in figure 3.1 (right). In the linear case $\eta_{rms,max}$ monotonically decreases from 1.64 close to the leading edge to 1.1 at the furthest downstream distance considered. When the Görtler vortices evolve linearly, $\eta_{rms,max}$ moves towards the wall, in contrast to the edge-layer confinement observed for Klebanoff modes, i.e. the movement of the peak location closer to the boundary-layer edge (Leib *et al.*, 1999). Corresponding to the downstream positions where nonlinearity first exerts its influence, a rapid shift of $\eta_{rms,max}$ towards the free stream is observed. Surprisingly, this increase is larger for smaller r_t. When the flow starts saturating, $\eta_{rms,max}$ drops towards the wall and a transverse distance of approximately $\eta_{rms,max}$=0.5 is approached, regardless of the turbulence level. Therefore, as the nonlinear effects become more intense the boundary-layer perturbations are attenuated and concentrate in a near-wall region. This rapid shift of the vortices towards the wall, which is primarly due to the nonlinear distortion of the seeded mode, is not reported in other nonlinear analyses. More insight is provided in §3.2.5 by investigating the wall-normal profiles of the streamwise velocity.

For the case with $r_t = 0.01$ the downstream development of the maximum energy associated with the seeded mode and the higher harmonics, i.e.

$$E_{m,n}(\bar{x}) = \max_{\eta} |r_t \hat{u}_{m,n}(\bar{x},\eta)|^2, \tag{3.17}$$

is shown in figure 3.2. The wall-normal and spanwise disturbance velocity components are much smaller than the streamwise component and are therefore ne-

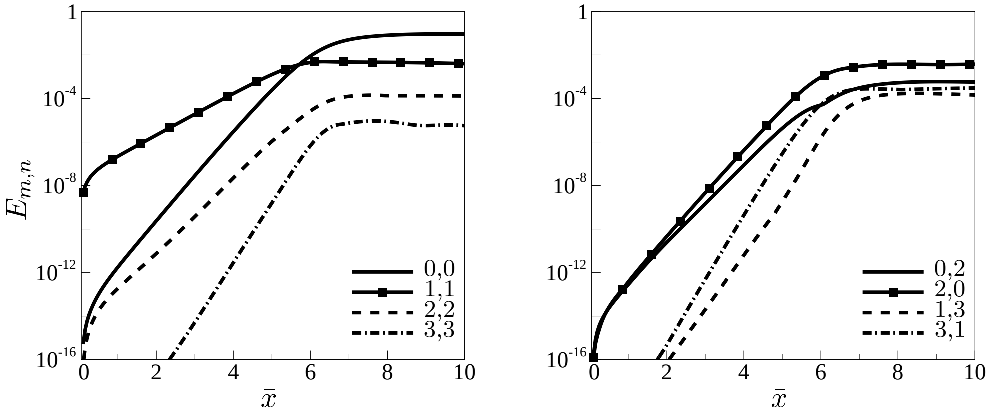

Fig. 3.2: Downstream development of maximum energy associated with the fundamental mode and nonlinearly generated harmonics at r_t=0.01. The parameters are $\mathcal{G}$=14.7, k_x=0.00435 (refer to case 1 in table 3.1).

glected in (3.17). For $\bar{x}$<5 the fundamental mode is dominant, but the other harmonics grow rapidly, all at a greater rate than the seeded mode. Further downstream, the mean-flow distortion acquires an amplitude which is one order of magnitude greater than that of the seeded mode and the second harmonic (2,0) become comparable with the fundamental mode (1,1), while the other harmonics remain of smaller amplitude. Sufficiently downstream the disturbance energy saturates. The steady analysis of Hall (1988) suggests that the disturbance energetics is dominated by the interaction between the mean-flow distortion and the fundamental (n=1) mode. In the unsteady case, in addition to the energy exchange between the modes $(0,0)$ and $(1,1)$, the contribution of the harmonic $(2,0)$ becomes important.

Effect of frequency

The effect of frequency is investigated by comparing the downstream development of $u_{rms,max}$ for the two cases in table 3.1, i.e. f^*=5 Hz (case 1) and 11 Hz (case 2). The turbulent Reynolds number is r_t=0.01. With our definition of Görtler number (3.2), $\mathcal{G}$ decreases with increasing k_x, while G_λ does not change. Figure 3.3(a)

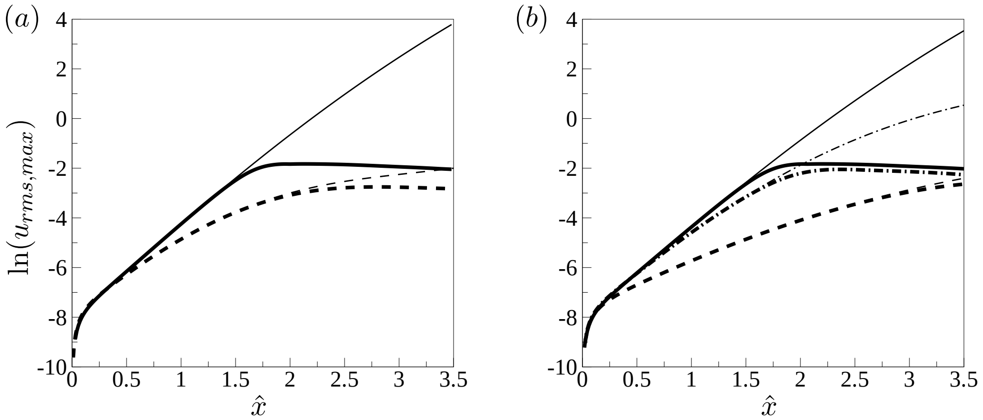

Fig. 3.3: Linear (thin lines) and nonlinear (thick lines) development of $\ln(u_{rms,max})$ for (a) different frequencies (refer to table 3.1): case 1, i.e. k_x=0.00435, (dashed line), case 2, i.e. k_x=0.00957, (solid line), and (b) different Görtler numbers (refer to table 3.2): case 1, i.e. $\mathcal{G}$=14.7 and k_x=0.00435, (solid line), case 1r, i.e. $\mathcal{G}$=7.3 and k_x=0.00435, (dashed line), case 1f, i.e. $\mathcal{G}$=7.3 and k_x=0.00693, (dash-dotted line). The turbulent Reynolds number is r_t=0.01.

shows that the lower the frequency, the more intensely the disturbance grows and the larger the signature becomes, consistently with the generally accepted theory that steady vortices are the most amplified. The stabilizing effect of nonlinearity is intensified for lower frequencies and the nonlinear effects start asserting their influence further upstream. This result is expected from the flat-plate calculations of Ricco *et al.* (2011). However, the effect of k_x is more pronounced for a curved wall as the centrifugal forces, which determine the exponential growth, are enhanced for longer wavelengths.

Effect of Görtler number

To study the effect of the Görtler number $\mathcal{G}$ independently from the other parameters, we compare two cases with different radius of curvature (case 1 and case 1r in table 3.2). Case 1 was already presented in table 3.1 and is reported here again for clarity.

In case 1r, r_0^* is double than that in case 1, i.e. the plate is less curved.

Case	U^*_∞ [ms^{-1}]	λ^*_z [m] $\times 10^3$	r^*_0 [m]	f^* [Hz]	R_λ	G_λ	$\hat{k}_x$	k_x $\times 10^3$	κ	$\mathcal{G}$	r_t
1	9.18	8	8.37	5	767	89.5	3.336	4.35	0.547	14.7	0.01
1r	9.18	8	**16.8**	5	767	44.5	3.336	4.35	0.547	7.3	0.01
1f	9.18	8	8.37	**8**	767	89.5	5.317	6.93	0.434	7.3	0.01

Tab. 3.2: Choice of parameters for the study on the Görtler number effect. The physical parameters that are varied with respect to case 1 are highlighted in bold.

This results in $\mathcal{G}$ and G_λ being halved, while all the other parameters are held constant. As shown in figure 3.3(*b*), the effect of increasing r^*_0 is analogous to that of increasing the frequency, i.e. the amplitude of the response and the growth rate are attenuated and the nonlinear effects become weaker. For the particular set of parameters corresponding to case 1r the linear and nonlinear solutions are almost indistinguishable in the range of $\bar{x}$ analyzed.

The same $\mathcal{G}$ used in case 1r is obtained from case 1 by varying the frequency, specifically by multiplying k_x by a factor $2^{2/3}$ (case 1f in table 3.2). The stabilizing effect on the disturbance signature that is obtained by halving $\mathcal{G}$ is less marked when the decrease of $\mathcal{G}$ is due to an increased frequency rather than an increased r^*_0 because in the former case other effects come into play, i.e. κ decreases as k_x increases. While in the steady limit (refer to Wu *et al.* (2011) for the linear case), the growth rate is affected only by the radius of curvature, in the unsteady case the response is determined by a combined effect of the frequency and of the radius of curvature.

3.2.3 High free-stream turbulence intensity

We now consider free-stream disturbances with $r_t>1$, at least i.e. ten times more intense than the highest r_t case in §3.2.2. The relevant range of turbulence level is typical of turbomachinery applications. The other parameters correspond to case 2 in table 3.1.

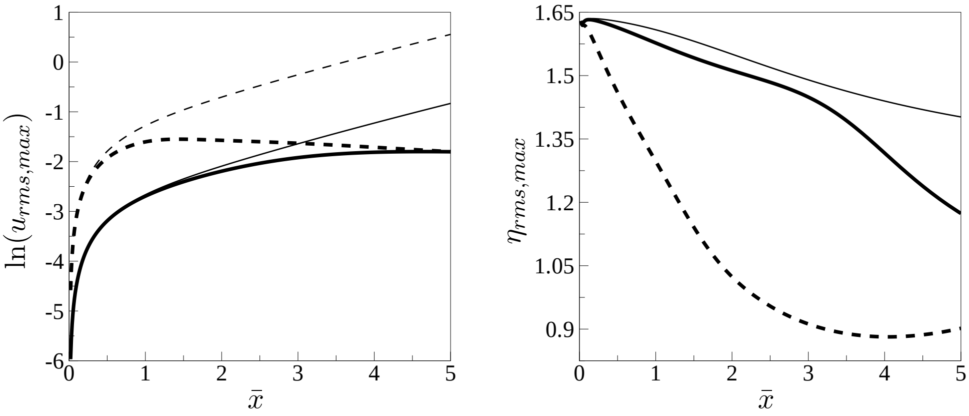

Fig. 3.4: Effect of high FSTI on the downstream evolution of the streamwise velocity signature and its wall-normal position: r_t=1.34 (solid line) and r_t=5.36 (dashed line). The thin/thick curves indicate the linearized/nonlinear solutions. The parameters are $\mathcal{G}$=4.5 and k_x=0.00957 (refer to case 2 in table 3.1).

The downstream development of the streamwise velocity signature for different turbulence intensities, Tu=0.5% and 2% (r_t=1.34 and 5.36), is shown in figure 3.4 (left). Even for a relatively low Görtler number, the nonlinear effects are very intense and start asserting their influence close to the leading edge. For similar values of r_t the nonlinear effects on the laminar streaks over a flat plate are very weak (refer to the case with r_t=2 in figure 2a of Ricco *et al.* (2011)).

The downstream development of $\eta_{rms,max}$ is displayed in figure 3.4 (right). In the low turbulence-intensity case (refer to figure 3.1) an overlapping of the linear and nonlinear curves was observed for most of the initial growth, followed by a shift of $\eta_{rms,max}$ towards the edge of the boundary layer. In enhanced disturbance environments, instead, the exponential growth where linear and nonlinear solutions coincide is absent. Furthermore, the wall-normal peak of $u_{rms,max}$ deviates from the linear behavior just downstream of the leading edge and continuously moves towards the wall as $\bar{x}$ increases. In the largest r_t case, $\eta_{rms,max}$ drops from 1.64 to 0.9 in a short downstream distance and no overlapping with the linear curve is detected, even at downstream locations where the nonlinear development of $u_{rms,max}$ is indistinguishable from the linearized approximation, i.e. $\bar{x}$=0.3 for r_t=5.36. Therefore, at high turbulence intensities the influence of nonlinearity is revealed first as a shift of the maximum perturbation toward to the wall and, further downstream, as the attenuation of the boundary-layer disturbances.

As in §3.2.2, two cases with different radius of curvature, i.e. case 2 and case 2r in table 3.3, are considered. The radius of curvature of case 2r is half that of case 2 and thus $\mathcal{G}$ and G_λ for case 2r are double those of case 2, while all the other parameters are unchanged.

Case	U_∞^* [ms^{-1}]	λ_z^* [m] $\times 10^3$	r_0^* [m]	f^* [Hz]	R_λ	G_λ	$\hat{k}_x$	k_x $\times 10^3$	κ	$\mathcal{G}$	r_t
2	9.18	8	8.37	11	767	89.5	7.342	9.57	0.369	4.5	2.68
2r	9.18	8	4.19	11	767	179	7.342	9.57	0.369	9	2.68

Tab. 3.3: Choice of parameters for the study on the Görtler number effect.

As shown in figure 3.5, the two nonlinear curves for case 2 and 2r are almost identical, while the linearized $u_{rms,max}$ of case 2r is more intense than that of case 2 because of the more pronounced centrifugal effects. At low turbulence intensities, the effect of Görtler number becomes evident at downstream locations where the perturbation exhibits a (quasi-)exponential growth (3.3). At elevated turbulence intensities, the nonlinear response is not influenced by the Görtler number if r_t is sufficiently high for the disturbance to saturates without undergoing an exponential growth.

3.2.4 Growth rate

As pointed out by Saric (1994), when the basic flow is nonparallel different disturbance quantities can be tracked to measure the growth or decay of the vortices (refer to eqs. 15-17 in Saric (1994)). To calculate the overall growth (or decay) of the disturbance due to all the harmonics inside the boundary layer, the following

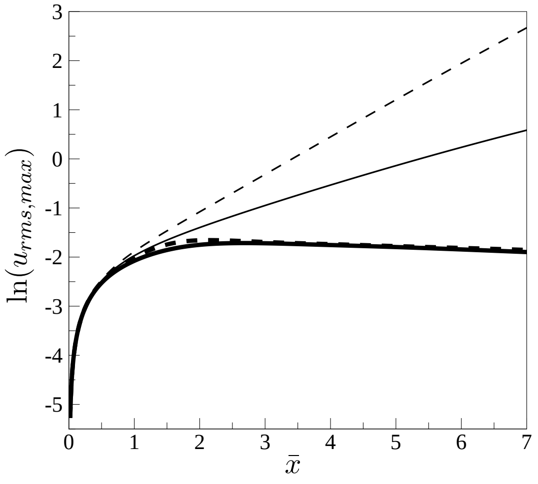

Fig. 3.5: The amplitude $\ln(u_{rms,max})$ versus $\hat{x}$ for different radius of curvature (refer to table 3.3): case 2, i.e. r_0^*=8.37 and $\mathcal{G}$=4.5 (solid line), case 2r, i.e. r_0^*=4.19 and $\mathcal{G}$=9 (dashed line), for r_t=2.68 and fixed frequency k_x=0.00957.

definition of growth rate based on $u_{rms,max}$ can be introduced

$$\bar{\alpha} = \frac{1}{u_{rms,max}} \frac{\mathrm{d}u_{rms,max}}{\mathrm{d}\bar{x}}. \tag{3.18}$$

As it was shown in figure 3.2 that sufficiently downstream the exchange of energy mainly occurs between the mean-flow distortion, the spanwise-averaged second harmonic and the seeded mode, we also calculate:

$$\alpha_{m,n} = \frac{1}{\hat{u}_{m,n,max}} \frac{\mathrm{d}\hat{u}_{m,n,max}}{\mathrm{d}\bar{x}}, \tag{3.19}$$

where $\hat{u}_{m,n,max}$ is the maximum along η of $\hat{u}_{m,n}$ and (m,n)=$(\pm1,1)$, $(0,0)$, $(\pm2,0)$. The real and imaginary parts of $\alpha_{\pm1,1}(\bar{x})$ represent the growth rate and the wavenumber of the seeded modes, respectively. Following Hall (1988), another way to study the growth or decay of the mean-flow distortion is to monitor

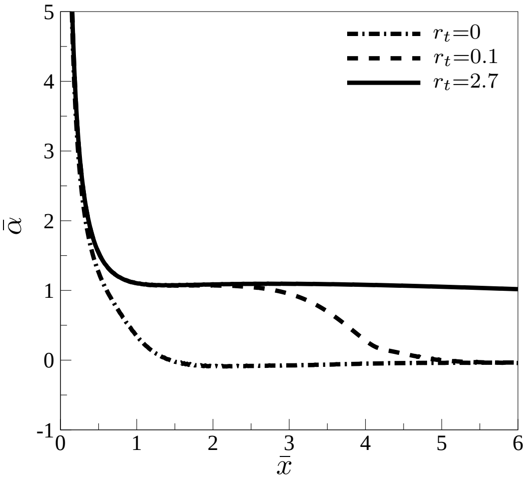

Fig. 3.6: Local growth rate $\bar{\alpha}$ versus $\bar{x}$ for different r_t. The parameters are $\mathcal{G}$=14.7, k_x=0.00435 (refer to case 1 in table 3.1)

the disturbance energy associated with the mode (0,0), i.e.

$$E_0 = \int_0^\infty \hat{u}_{0,0}^2(\bar{x}, y)\mathrm{d}y,$$

After rewriting the integral in E_0 in terms of η, the following expression for the growth rate of the mean-flow distortion is obtained (Hall, 1983)

$$\sigma_0 = \frac{1}{E_0}\frac{\mathrm{d}E_0}{\mathrm{d}\bar{x}} = \frac{1}{2\bar{x}} + \frac{1}{E_1}\frac{\mathrm{d}E_1}{\mathrm{d}\bar{x}}, \text{ with } E_1 = \int_0^\infty \hat{u}_{0,0}^2(\bar{x}, \eta)\mathrm{d}\eta.$$

Unless otherwise specified, the results presented in the following refer to case 1 of table 3.1.

Figure 3.6 shows the local growth rate $\bar{\alpha}$ for different r_t=0 (linear case), 0.1 (low FSTI case) and 2.7 (high FSTI case). In the linear case, the growth rate becomes a nearly constant function of $\bar{x}$ for $\bar{x} > 1$, thus confirming the conclusion of Wu *et al.* (2011) that the growth of the excited perturbation is (quasi-) exponential. For a low turbulence level, i.e. r_t=0.1, the disturbance first undergoes an exponential growth at the same rate as the linear solution. When the nonlinear effects become more intense, the growth rate drops and approaches zero as the saturation stage is reached. For a high turbulence level, i.e. r_t=2.7, the disturbance does not exhibit an exponential growth. The growth rate is slightly negative for $1.5<\bar{x}<5$ and null for $\bar{x}>5$ as the nonlinear effects saturate.

In the linear study of Wu *et al.* (2011) the wall-normal wavenumber k_y, which only appears in the outer boundary conditions at the first order, was shown to have a negligible effect on the boundary-layer response in the case of steady and low-frequency components of the free-stream perturbation. This is a further proof of the eigenvalue nature of the solution for sufficiently high Görtler numbers, i.e. the induced disturbance develops into an eigensolution excited by the free-stream vortical perturbation through a receptivity mechanism.

We herein study the effect of κ_y on the growth rate and wavenumber of the nonlinearly generated disturbance inside the boundary layer for r_t=0.1. A variation of κ_y from the value corresponding to case 1 in table 3.1 (κ_y=0.54) is obtained by only changing k_y, while k_x and k_z are kept fixed so that κ is constant. In the case with κ_y=0.54 the scaled amplitudes of the free-stream velocity components were $\hat{u}^{\infty}_{x,\pm}=\hat{u}^{\infty}_{y,\pm}=1$ and $\hat{u}^{\infty}_{z,\pm}=\mp 1$ (refer to section §3.2.1). Without loss of generality, it is convenient to keep $\hat{u}^{\infty}_{x,\pm}=1$ because our definition of turbulence intensity is based on the streamwise velocity component of the free-stream perturbation. It follows that $\hat{u}^{\infty}_{y,\pm}$ and $\hat{u}^{\infty}_{z,\pm}$ are determined from the continuity equation (2.4) and from the constraint of constant amplitude of the free-stream velocity vector, i.e. $\sqrt{(\hat{u}^{\infty}_{x,\pm})^2+(\hat{u}^{\infty}_{y,\pm})^2+(\hat{u}^{\infty}_{z,\pm})^2}=\sqrt{3}$.

Figure 3.7 displays the growth rate and wavenumber of the seeded mode for different κ_y. In the regions of quasi-exponential growth ($1.5<\bar{x}<3$) and of nonlinear saturation ($\bar{x}>5$), where the disturbance has a well-defined local wavenumber and growth rate, κ_y does not have an appreciable effect. In the interval between those two, where $\Re[\alpha_{-1,1}]$ and $\Im[\alpha_{-1,1}]$ vary rapidly with $\bar{x}$, and during the ini-

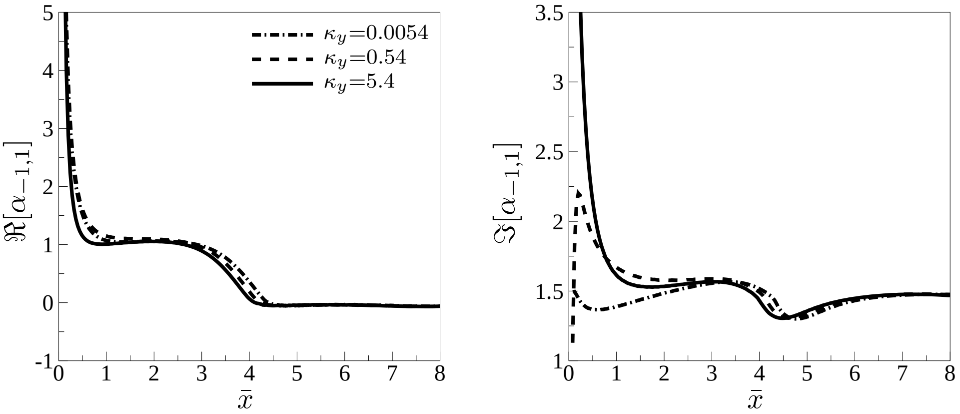

Fig. 3.7: Local growth rate $\Re[\alpha_{-1,1}]$ (left) and streamwise wavenumber $\Im[\alpha_{-1,1}]$ (right) of the seeded mode versus $\bar{x}$ for different κ_y at r_t=0.1. The case with κ_y=0.54 corresponds to case 1 in table 3.1.

tial growth from the leading edge, the effect of κ_y is more marked, especially for the lowest κ_y case. The growth rate decreases slightly as κ_y increases and the streamwise wavenumber shows a significant increase as κ_y grows for $\bar{x}<1$.

Analogous observations are drawn for the growth rate of the mean-flow distortion $\alpha_{0,0}$ and of the spanwise-averaged second harmonic $\Re[\alpha_{-2,0}]$ shown in figure 3.8. The growth rate of the mean-flow distortion is more than double that of the fundamental mode in the region of exponential growth and the nonlinear saturation occurs further downstream ($\bar{x}>6.5$). The growth rate $\Re[\alpha_{-2,0}]$ slowly increases with $\bar{x}$ in the region of exponential growth and the highest κ_y case shows a significant variation for $\bar{x}<1.5$.

3.2.5 Wall-normal profiles

The wall-normal profiles of the streamwise velocity are examined for case 1 of table 3.1, as this case features intense centrifugal effects. The turbulent Reynolds number is chosen as r_t=0.1 to allow sufficient linear growth in the initial stage of the flow evolution (i.e. the nonlinear solution undergoes an exponential growth before nonlinearity saturates). The profiles of the streamwise velocity of the fun-

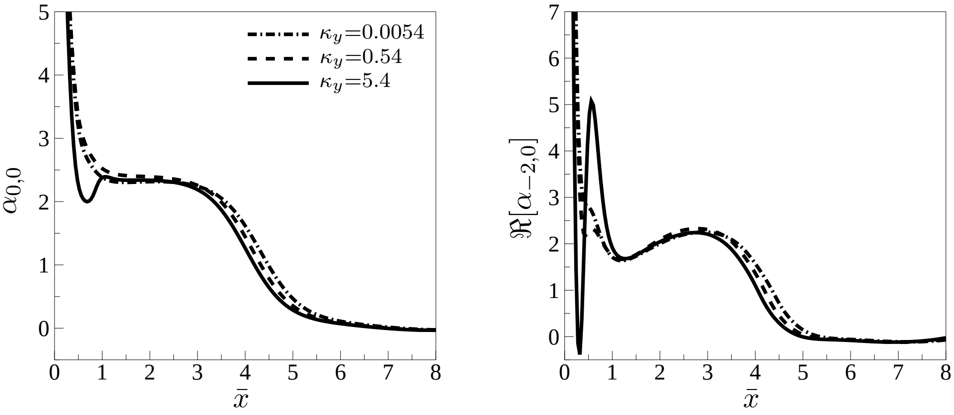

Fig. 3.8: Local growth rates of the mean-flow distortion $\alpha_{0,0}$ (left) and of the spanwise-averaged second harmonic $\alpha_{-2,0}$ (right) versus $\bar{x}$ for different κ_y at r_t=0.1. The case with κ_y=0.54 corresponds to case 1 in table 3.1.

damental mode and higher harmonics are displayed in figures 3.9 at $\bar{x}$=3 and $\bar{x}$=5 (the y-axis scale in the left graph ($\bar{x}$=3) is ten times smaller than in the right graph ($\bar{x}$=5)). The mean-flow distortion (mode $0,0$) grows by more than an order of magnitude from $\bar{x}$=3 and $\bar{x}$=5 and becomes larger than the fundamental mode. The crossover between the mean-flow distortion and the seeded mode was already observed in figure 3.2. The second harmonics exhibit an appreciable amplification, especially the spanwise-averaged mode (-2,0), which becomes comparable with the mode (-1,1) at $\bar{x}$=5. The linear profile is also shown in figure 3.9. At $\bar{x}$=3 the nonlinear profile of $r_t|\hat{u}_{1,1}|$ and its linear approximation are quite similar and have a peak at η=1.3. At $\bar{x}$=5 the linear profile has maintained its shape and increased its magnitude by nearly ten times. The nonlinear profile of $r_t|\hat{u}_{1,1}|$ has instead amplified far less than its linearized counterpart. Its shape has changed considerably as two maxima appear in the nonlinear profile of $r_t|\hat{u}_{1,1}|$ at $\bar{x}$=5: the first peak is slightly larger and is located at η=0.7, while the second one is less pronounced and is located in the outer portion of the boundary layer, at η=3. For η>2.5, the nonlinear profile of $r_t|\hat{u}_{1,1}|$ is larger than the linear solution. The enhancing effect of nonlinearity in the outer part of the boundary

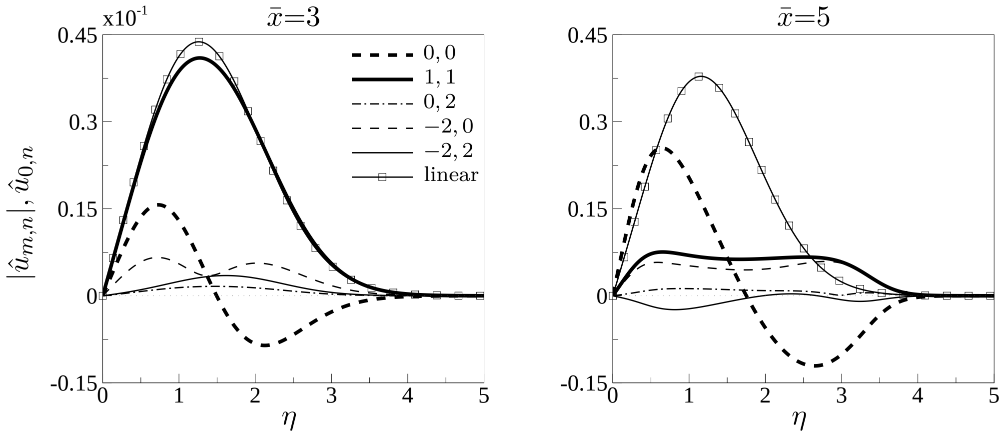

Fig. 3.9: Streamwise-velocity profiles of the fundamental mode, mean-flow distortion and second harmonics at $\bar{x}$=3 (left) and $\bar{x}$=5 (right).

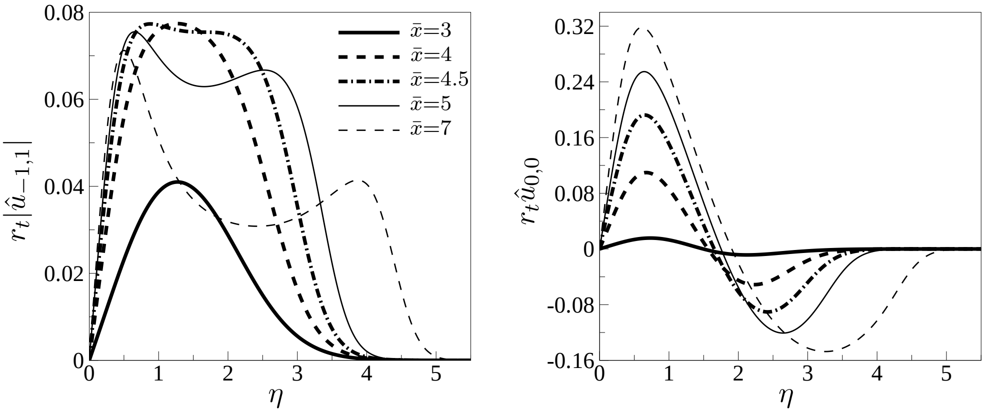

Fig. 3.10: Profiles of $r_t|\hat{u}_{-1,1}|$ (left) and $r_t\hat{u}_{0,0}$ (right) at different $\bar{x}$.

layer was already pointed out by Ricco *et al.* (2011) in the case of a flat plate, but it becomes more evident in the presence of centrifugal forces and leads to new features of the boundary-layer solution. For example, the appearance of an outer-flow peak in the profile of $r_t|\hat{u}_{1,1}|$ was not detected in the flat-plate case of Ricco *et al.* (2011).

The left graph of figure 3.10 displays the nonlinear profiles of $r_t|\hat{u}_{1,1}|$ at five different downstream locations. The single peak which appears in the core of the boundary layer at $\bar{x}$=3, moves towards the wall at $\bar{x}$=4.5 and, at the same time, another peak appears in the outer portion of the boundary layer. As the flow evolves downstream, the two maxima distance themselves, with a more intense peak moving closer to the wall and a less pronounced peak shifting towards the free stream. As a result, the streamwise-velocity perturbation in the nonlinear case persist further away from the wall as compared to the linearized counterpart. The profiles shown in figures 3.9 and 3.10 qualitatively agree with the results of Hall (1988). A physical explanation of the nonlinear mechanism that produces the distortion of the seeded mode could not be provided in the latter paper. The perturbation due to the base-flow distortion, $r_t\hat{u}_{0,0}$, shown in the right graph of figure 3.10, also moves towards the outer part of the boundary layer where backward jets form (Wu *et al.*, 1999). This suggests that the flow may become first inviscidly unstable in the upper region of the boundary layer (Jacobs and Durbin, 2001).

It is also interesting to study the wall-normal and spanwise velocity profiles, which are displayed in figure 3.11 for the same downstream locations shown in figure 3.9, i.e. $\bar{x}$=3 and 5. As implied by the boundary-region scaling (refer to §3.1.1), the cross-flow velocity components are much smaller than the streamwise velocity. The mean-flow distortion and the higher harmonics grow by nearly one order of magnitude from $\bar{x}$=3 to $\bar{x}$=5, while the amplification of the fundamental mode is not as intense as that of its linearized counterpart. At $\bar{x}$=5 the effect of nonlinearity is to reduce the amplitude of the seeded mode as compared to the linear profile and to move the peak towards the free stream, thus slightly enhancing the fluctuations in the outer part of the boundary layer. The stabilizing effect of nonlinearity on the wall-normal and spanwise velocity components is in contrast to the nonlinear steady results of Hall (1988), who showed enhanced nonlinear profiles of the fundamental mode as compared to the linear solutions (refer to figure 3(e,f) of Hall (1988)). Analogously to the steady case (Hall, 1983),

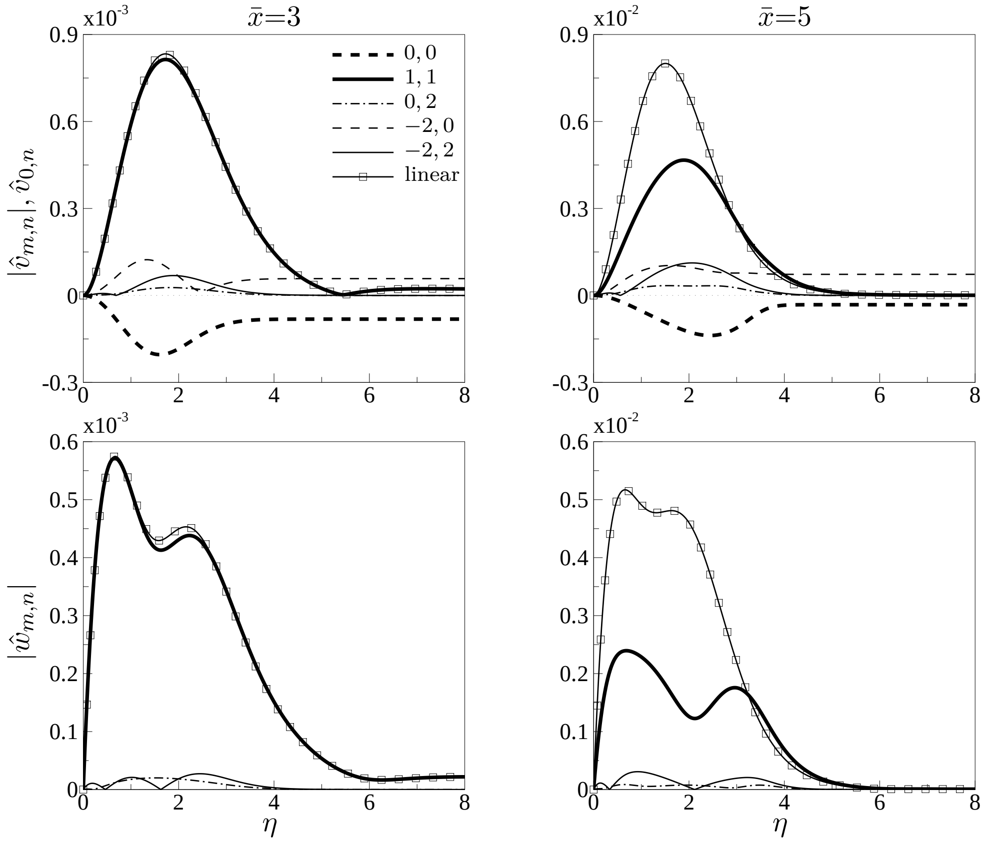

Fig. 3.11: Wall-normal (first row) and spanwise (second row) velocity profiles of the fundamental mode and higher harmonics at $\bar{x}$=3 (left) and $\bar{x}$=5 (right).

in the linear regime the shape of the three velocity components change little with increasing $\bar{x}$, while in the nonlinear case, a distortion of the velocity profile of the seeded mode is observed as the flow evolves downstream. This distortion is far more pronounced for the streamwise velocity than for the cross-flow velocities. At $\bar{x}$=5 both the wall-normal and spanwise velocity are no longer influenced by the free-stream forcing, indicating that the perturbation has evolved into an eigenmode (Wu *et al.*, 2011).

Figure 3.12 shows the contours of the total streamwise velocity u=$F' + r_t\bar{u}$ in the $\eta - z$ plane at $\bar{x}$=5 during different phases φ≡$k_x t$ of the time modulation. At φ=$11\pi/9$ the flow-field exhibits a mushroom-like structure which is associated with the upwelling of low-momentum fluid at z=π and downwelling of high momentum fluid at z=0, 2π. The mushroom-like shape is observed in experiments of steady Görtler vortices (Swearingen and Blackwelder, 1983; Tandiono *et al.*, 2008) and reproduced in numerical simulations of both steady (Hall and Horseman, 1991; Benmalek and Saric, 1994) and unsteady disturbances (Schrader *et al.*, 2011). The low-high momentum distribution shown in figure 3.12 produce inflectional profile in the wall-normal and spanwise directions, which are bound to support localized instability (Swearingen and Blackwelder, 1983; Li and Malik, 1995; Wu and Luo, 2003; Wu and Choudhari, 2003) .

3.2.6 Comparison with DNS and experiments

A comparison with the DNS results of Schrader *et al.* (2011) is carried out. Schrader *et al.* (2011) considered Görtler boundary layers subject to a broadband free-stream turbulence with different frequency spectra and intensities. The free-stream turbulence field denoted as FST3 in their table 4 is chosen for our comparison. This turbulence field is nearly isotropic in the crossflow plane and is characterized by low-frequency components f^*=$2.0 - 32.5$ Hz. The turbulence

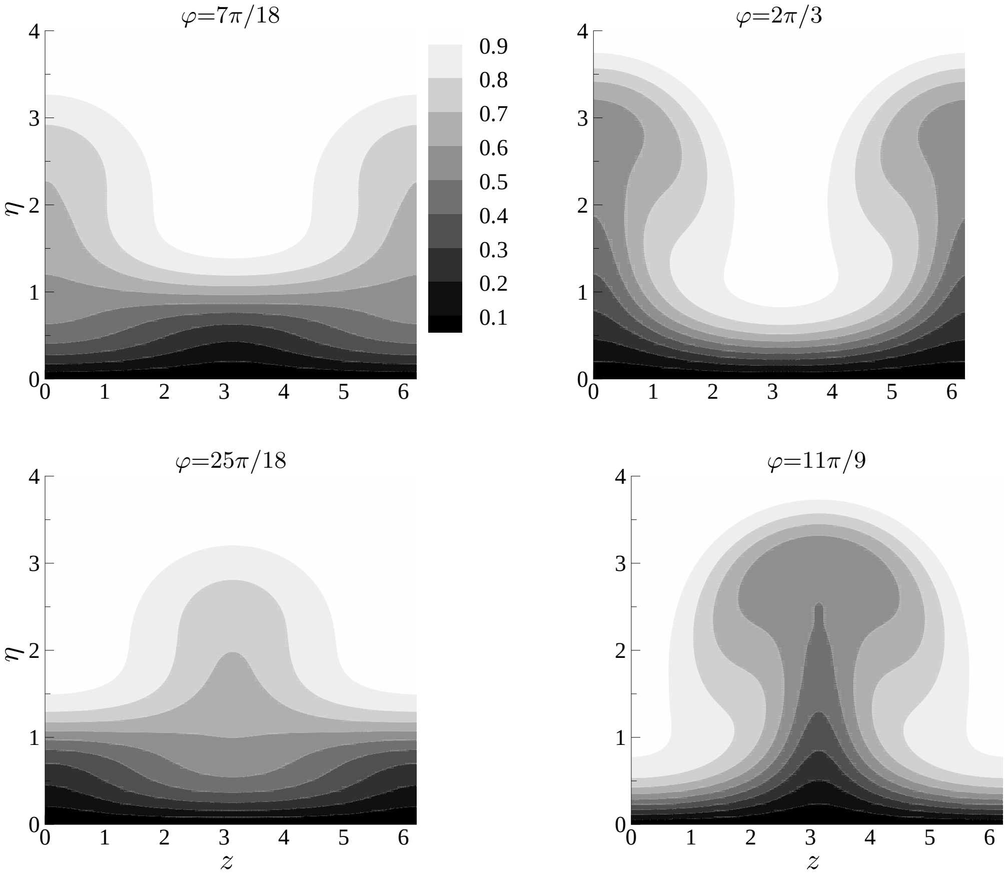

Fig. 3.12: Contour of total streamwise velocity in the $\eta - z$ plane at $\bar{x}$=5 for different time instants. The labels in each graph indicate the phases φ of the time modulation.

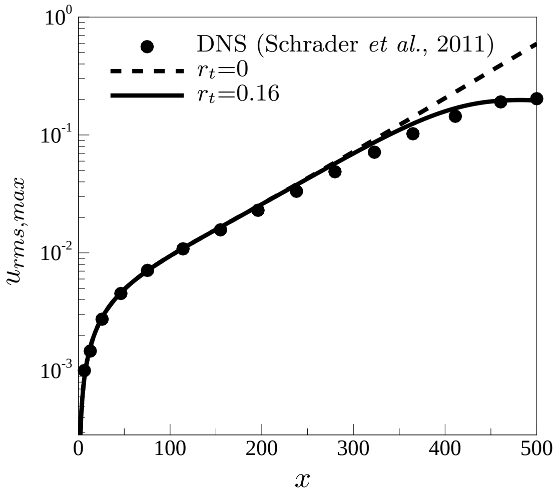

Fig. 3.13: Streamwise evolution of $u_{rms,max}$ for r_t=0 and r_t=0.16 and comparison of the latter case with DNS solution from figure 22 of Schrader *et al.* (2011).

level is Tu=0.1%. The relevant parameters used in our simulations are summarized in table 3.4.

U^*_∞ [ms^{-1}]	r^*_0 [m]	λ^*_z [m]	f^* [Hz]	λ^*_x [m]	F_b	R_λ	k_x	κ	$\mathcal{G}$	r_t
2.85	1	0.0149	4.14	0.689	48	450	0.0216	0.321	15.8	0.16

Tab. 3.4: Parameters from DNS of Schrader *et al.* (2011).

The spanwise wavenumber and frequency correspond to those of the most energetic unsteady disturbance present in the boundary layer, as shown in figure 23 of Schrader *et al.* (2011). In figure 3.13 the predicted streamwise velocity signature is compared to the results reported by Schrader *et al.* (2011). The linearized trend is also displayed to show that nonlinear effects are at work. Our nonlinear solution matches the DNS data very well up to x=300, after which the agreement slightly deteriorates because of a lower disturbance growth rate in the DNS as compared to our simulation. At this downstream location the transitional area of the plate is entered and small-scale fluctuations start affecting the disturbance signature, which may explain why a little discrepancy is found in this region.

It is worth pointing out that the boundary-region approach is computationally much cheaper than a DNS. For example, a typical simulation requires 12 hours clock time and less than 500 MB memory on a single Intel processor. Schrader *et al.* (2011) do not provide information on the computational cost of their simulations, but it can be assumed to be on the same order of magnitude as that of other DNS studies based on the Orr-Sommerfeld approach. For example the DNS of Jacobs and Durbin (2001) of bypass transition on a flat plate required approximately 500 CPU hours per processor with 128 processors. When the computational domain is extended further upstream to allow for realistic free-stream conditions, the computational cost becomes almost prohibitive. For example, the simulations performed by Ovchinnikov *et al.* (2008) required a month of CPU time on an 8-processor cluster.

Our results are also compared with the experimental data of Tandiono *et al.* (2008). In these experiments the wavelength of the Görtler vortices is preset by a series of vertical perturbation wires positioned between the turbulence-generating screens and the leading edge of the plate. The comparison is carried out with their case 1, i.e. U_∞^*=2.85 m/s and λ_z=12 mm. The frequency spectra in the pre-transitional area of the plate are not provided in Tandiono *et al.* (2008) because the boundary-layer disturbances are found to be quasi-steady. A time-averaging of the velocity profile is performed in order to cut wind-tunnel noise (T. Tandiono, 2016, personal communication). Schrader *et al.* (2011) showed that, in the case of roughness-induced Görtler vortices, the growth rate of the low-frequency ($F_b \leq 16$) and steady Görtler modes are almost identical. Therefore, we assume a sufficiently low frequency f^*=1 Hz (F_b=11.6) so that the results can be considered ‘quasi-steady’. The turbulence level is Tu=0.45%. Computations were performed employing the parameters given in table 3.5.

The predicted profiles of the total streamwise velocity at the upwash (z=π)

U^*_∞ [ms^{-1}]	r^*_0 [m]	λ^*_z [m]	f^* [Hz]	λ^*_x [m]	F_b	R_λ	k_x	κ	$\mathcal{G}$	r_t
2.85	1	0.012	1	2.85	11.6	362	0.0042	0.809	133	0.58

Tab. 3.5: Parameters from the experiments of Tandiono *et al.* (2008).

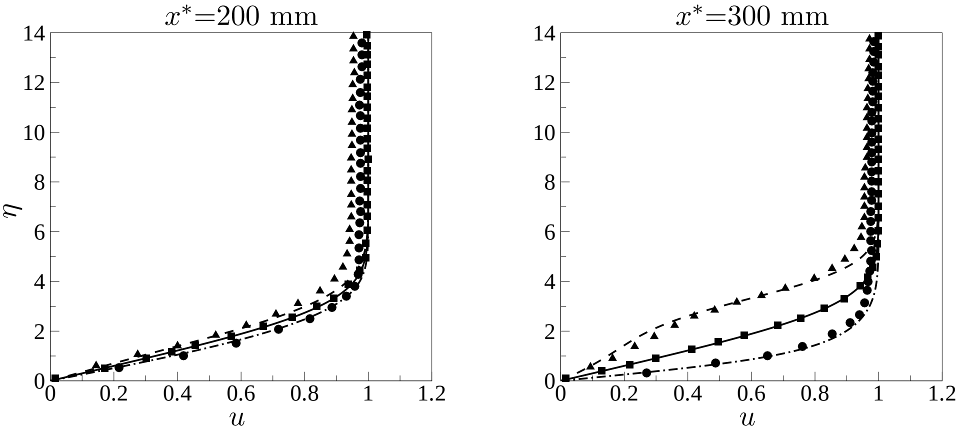

Fig. 3.14: Comparison between the streamwise-velocity profiles from figure 4 of Tandiono *et al.* (2008) (symbols) and our numerical solutions (lines): Blasius (solid line and squares), upwash (dashed line and triangles), downwash (dash-dotted line and circles). The wall-normal coordinate is $\tilde{\eta}$=$y^*\sqrt{U^*_\infty/(x^*\nu^*)}$, as in Tandiono *et al.* (2008)

and at the downswash (z=0) at t=0 are displayed in figure 3.14 for two different downstream locations. The Blasius solution is also shown, which perfectly matches the experimental data. Good agreement is obtained for the upwash and downwash profiles inside the boundary layer up to $\tilde{\eta}$=$y^*\sqrt{U^*_\infty/(x^*\nu^*)}\approx 5$, with the distortion of the upwash profile at x=300 mm being captured accurately by our numerical simulations. The profiles of Tandiono *et al.* (2008) do not approach unity in the free-stream because they are normalized with the local free-stream streamwise velocity which is different from the oncoming streamwise velocity because of a slight pressure gradient. This explains the discrepancy betwen our results and the experimental data for $\tilde{\eta}$>5.

3.3 Summary

This chapter has presented theoretical and numerical results on the generation and nonlinear development of unsteady Görtler vortices in an incompressible boundary layer over a concave plate. Görtler rolls are excited by free-stream vortical disturbances, whose amplitudes are large enough for the boundary-layer response to become nonlinear at downstream locations where the spanwise wavelength is comparable with the local boundary-layer thickness. Only the low-frequency components of the oncoming perturbation are of interest, as they are known from experiments to penetrate and amplify the most into the boundary layer. The present mathematical framework closely follows that of Ricco *et al.* (2011) for the nonlinear evolution of Klebanoff modes over a flat plate and extends it to account for centrifugal effects caused by the concavity of the wall. The formation and development of the induced disturbances are governed by the nonlinear unsteady boundary-region equations, with the centrifugal force included. The influence of the upstream and free-stream forcing is taken into account by imposing the appropriate initial and far-field boundary conditions, which are shown to be the same as those employed by Ricco *et al.* (2011).

As in the case of a flat plate, the nonlinear interactions inside the boundary layer have an attenuating impact on the boundary-layer signature, but this effect is significantly enhanced in the presence of a concave wall. Even at low free-stream turbulence intensities a sharp deviation of the nonlinear solution from its linearized approximation is observed. Furthermore, the wall-normal profiles of the streamwise velocity undergo a pronounced shape modification as the flow evolves downstream due to a shift of the perturbations towards the outer edge of the boundary layer.

Sufficiently downstream the nonlinear solutions obtained with different values of Tu are stabilized to the same level, suggesting that the initial amplitude of the disturbance becomes unimportant. At low turbulence intensities the perturbation exhibits a quasi-exponential growth with the growth rate being intensified for longer wavelengths and more curved plates. At enhanced turbulence levels, which are typical of turbomachinery applications, the Görtler vortices do not undergo an exponential growth because nonlinear effects come into play and saturate rapidly. As a result, for sufficiently high Tu the wall curvature, which only affects the exponentially growing part of the disturbance evolution, does no influence the boundary-layer response. While the majority of the studies on Görtler flow have focussed on steady vortices, unsteadiness is shown to have a significant effect on the overall disturbance energetics when the boundary layer is subject to free-stream turbulence. In the unsteady case, in addition to the energy exchange between the seeded mode and the mean-flow distortion which has been observed in steady analyses, the contribution of the spanwise-averaged harmonic with double the frequency of the fundamental mode becomes important.

The iso-contours of the instantaneous streamwise velocity in the cross-flow plane exhibit a mushroom-like structure which is attributed to the so-called lift-up effect. As a result, highly inflectional profiles of the streamwise velocity component in the wall-normal and spanwise directions form. These distorted profiles are bound to support inviscid secondary instability and lead to bypass transition to turbulence. Our results are shown to quantitatively agree with DNS and experimental data.

4. CONCLUSIONS AND FUTURE WORK

In this thesis the nonlinear response of a laminar boundary layer to unsteady free-stream vortical fluctuations of the convected-gust type has been investigated theoretically and numerically. The compressible boundary-layer over a flat plate is considered first, by assuming the free-stream Mach number M_∞ to be of $\mathcal{O}(1)$ and by including the effects of compressibility such as aerodynamic heating and heat transfer at the wall. In the second part of the thesis, attention is focussed on boundary-layer flows developing over concave plates in the incompressible regime. In the case of a flat plate, experimental evidence shows that low-frequency perturbations of the oncoming flow can penetrate into the core of the boundary layer to form streamwise-elongated components of the boundary-layer disturbances, known as Klebanoff modes or streaks. If the wall is concave with a suitable radius of curvature r_0, the streaks are expected to develop into unsteady Görtler vortices. In both cases, the amplitude of the fluctuations is sufficiently large for nonlinear interactions to occur within the boundary layer. The generation and nonlinear evolution of the induced disturbances are described using the mathematical framework of the nonlinear unsteady boundary-region equations, which arise in the rigorous asymptotic limit of the Navier-Stokes equations for low-frequency and long-wavelength perturbations. The two models for compressible streaks and incompressible Görtler vortices coincide with the analysis of Ricco *et al.* (2011) in the limits $M_\infty \to 0$ and $r_0 \to \infty$, respectively. The boundary-region equations are subject to appropriate initial (upstream) and far-field boundary conditions. The latter must account for the nonlinear interactions between the free-stream flow and the viscous boundary-layer flow, which occur through the displacement effect.

In the compressible regime, the spanwise-independent disturbance generated by the nonlinear interactions within the boundary layer is found to drive an unsteady two-dimensional flow of acoustic nature in the outer inviscid region. The analysis shows that the displacement-induced part of the outer perturbation assumes different forms depending on the regime being subsonic or supersonic. A close analogy with the flow over a thin oscillating airfoil is exploited to find analytical solutions. This analogy has been widely employed to investigate steady flows over boundary layers, but has been considered here for the first time for unsteady boundary layers. In the subsonic regime, the influence of the boundary-layer thickness pulsation is felt in all directions from the plate, while at supersonic speeds the fluid ahead of the body remains undisturbed and the perturbations are non zero only inside the Mach dihedron.

The signature of compressible nonlinear streaks inside the boundary layer is computed for carefully selected parameters that characterize three practical applications: turbomachinery systems, supersonic flight conditions and wind tunnel experiments. Nonlinearity is found to attenuate both kinematic and thermal streaks. At supersonic speeds, the stabilizing effect is more marked on the temperature than on the streamwise velocity. The results suggest that, even for a low-disturbance environment such as free flight, nonlinear effects must be taken into account to describe the formation and amplification of the streaks correctly. In the high-Mach number range, large-amplitude temperature fluctuations are detected, which are bound to be primarily responsible for the secondary instability of the streaky boundary layer. In the case pertaining to a supersonic wind tunnel, the nonlinear effects come into play abruptly by causing a sharp deviation of the nonlinear solution from the linear one. This phenomenon, together with the intense temperature fluctuations, is a new feature of supersonic flows.

In the second part of the thesis, the unsteady Görtler flow over a concave plate is investigated by including the centrifugal force in the incompressible nonlinear boundary-region equations. In the presence of a curved wall, the stabilizing effect of nonlinearity is noticeably enhanced as compared to the flat-plate case. The downstream amplification of the mean-flow distortion and the shape modification of the seeded mode profile are other two effects which are significantly intensified when the boundary-layer flow develops over a concave plate. Sufficiently downstream the nonlinear solutions obtained with different free-stream turbulence intensities Tu tend to reach the same plateau, suggesting that the initial amplitude of the disturbance becomes unimportant. At low Tu, the perturbation undergoes a quasi-exponential amplification with the growth rate being larger for disturbances with longer wavelengths and for more curved plates. The radius of curvature only influences the exponentially growing part of the disturbance evolution. At elevated Tu, in the typical range of turbomachinery applications, the nonlinear response is not affected by the wall curvature because nonlinear effects saturates rapidly and the boundary-layer disturbances do not exhibit an exponential growth. Although the available literature on Görtler flows is primarily devoted to steady vortices, our results reveal that unsteadiness may have a considerable effect on the overall disturbance energetics. In the steady case, the latter is dominated by the interaction between the mean-flow distortion and the seeded mode, while in the unsteady case the contribution of the spanwise-averaged harmonic with double the frequency of the fundamental mode becomes important. A comparison with DNS results and experimental data is performed and good quantitative agreement is obtained.

In both the studies carried out in this thesis, we have constructed the unsteady and three-dimensional base flow generated by the free-stream forcing and by the nonlinear interactions inside the boundary layer. This is the first step towards the formulation of the secondary-instability problem, which, in the compressible case, must account for both the velocity and thermal streaks. The secondary-instability analysis of the compressible streaky boundary layer is the subject of ongoing research. As the streaks are excited by physically-realizable free-stream disturbances rather than modelled by optimal perturbations, systematic secondary-instability calculations would yield, for instance, to a quantitative prediction of the relationship between Tu and the onset location of streak instability. Furthermore, the two analyses presented in this thesis can be combined to account for compressibility and curvature effects and, afterwards, the secondary instability of the compressible Görtler flow may be studied. Such investigation is of particular interest for turbomachinery applications as Görtler vortices are found to increase the heat transfer between the pressure surfaces of gas-turbine blades and the working fluid (Brown and Martin, 1982). Finally, the boundary-region approach may be employed in conjunction with DNS to simulate the entire process of bypass transition, including the entrainment of realistic free-stream disturbances into the boundary layer, without needing an excessively long computational domain. By combining the present methodology and solutions, which pertain to very low-frequency disturbances, with the analytical results of Wu and Dong (2016) for components of $\mathcal{O}(1)$ or higher frequency, it is now possible, for given broadband free-stream disturbances, to impose the appropriate inlet perturbations required by DNS of bypass transition in compressible and incompressible boundary layers. The correct inlet conditions cannot be provided by the Orr-Sommerfeld theory as nonparallel effects, which play a dominant role in the entrainment of FSVD into the boundary layer, are neglected.

APPENDIX

A. LINEAR/NONLINEAR BOUNDARY LAYER/REGION REGIMES

As stated in §2.1, the scaling (2.6) is assumed because this corresponds to the streamwise location where the strongest fluctuations are numerically observed. The appropriate scaling for the streamwise velocity fluctuation is $u{=}\epsilon\bar{u}/k_x$, where $\bar{u}{=}\mathcal{O}(1)$. It follows that $u{=}\mathcal{O}\left(\epsilon/k_x\right)$ or, using (2.6), $u{=}\mathcal{O}(\epsilon x)$. The latter condition is true also when $\bar{x}{\ll}1$ because in this case $\bar{u}$ grows linearly with $\bar{x}$.

The problem becomes nonlinear when the free-stream disturbance is strong enough for the streamwise velocity of the induced streaks to become $\mathcal{O}(1)$ in the boundary layer, that is:

$$u = \mathcal{O}\left(\frac{\epsilon}{k_x}\right) \rightarrow \begin{cases} \dfrac{\epsilon}{k_x} \ll 1 & \Longrightarrow \epsilon x \ll 1 \quad \Longrightarrow \quad \text{Linear,} \\ \dfrac{\epsilon}{k_x} = \mathcal{O}(1) & \Longrightarrow \epsilon x = \mathcal{O}(1) \Longrightarrow \quad \text{Nonlinear.} \end{cases}$$

The distinction between boundary layer (BL) and boundary region (BR) equations only depends on the ratio δ^*/λ^*, while it is independent of the order of magnitude of the velocity. If (2.6) is assumed, then $\kappa{=}\mathcal{O}(\delta^*/\lambda^*)$. The boundary-layer equations are valid as long as the local boundary-layer thickness is much smaller than spanwise length scale, that is:

$$\kappa = \mathcal{O}(\delta^*/\lambda^*) \rightarrow \begin{cases} \delta^* \ll \lambda^* \quad \text{ or } \kappa \ll 1 & \Longrightarrow x \ll R_\lambda \quad \Longrightarrow \quad \text{BL,} \\ \delta^* = \mathcal{O}(\lambda^*) \text{ or } \kappa = \mathcal{O}(1) & \Longrightarrow x = \mathcal{O}(R_\lambda) \Longrightarrow \quad \text{BR.} \end{cases}$$

These considerations are summarised in the figure A.1. Note that the cases $x{\gg}R_\lambda$ and $x{\gg}\epsilon^{-1}$ are not studied because they correspond to a downstream loca-

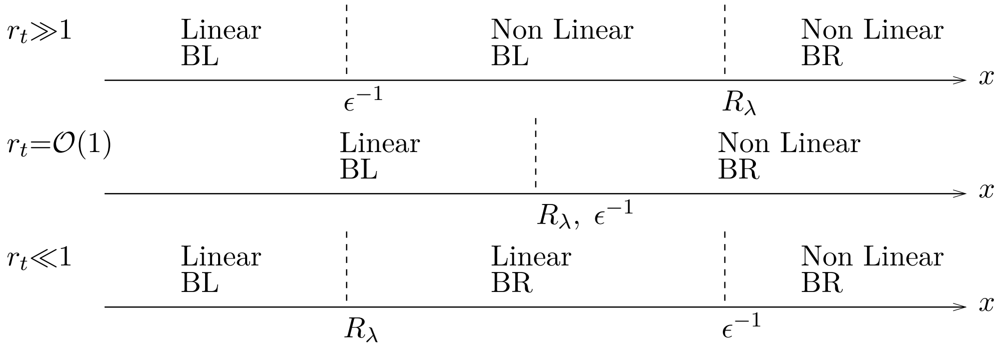

Fig. A.1: Schematic of the parameters distinguishing the linear/nonlinear boundary layer/region regimes.

tion where the disturbances have already decayed or where secondary instability has already occurred.

B. COMPRESSIBLE WALL-NORMAL VELOCITY COMPONENT OF THE BLASIUS FLOW

The wall-normal velocity component of the compressible Blasius boundary-layer flow is computed. Introducing the stream function $\psi(x,\eta)=\sqrt{2x/R_\lambda}F(\eta)$, the wall-normal velocity component is given by

$$V = -\frac{1}{\rho}\left.\frac{\partial\psi}{\partial x}\right|_y = -\frac{1}{\rho}\left.\frac{\partial\psi}{\partial x}\right|_\eta - \frac{1}{\rho}\left.\frac{\partial\psi}{\partial\eta}\right|_x \left.\frac{\partial\eta}{\partial x}\right|_y . \tag{B.1}$$

From (2.9) we derive

$$y(x,\eta) = \sqrt{\frac{2x}{R_\lambda}}\int_0^\eta T(\check{\eta})\mathrm{d}\check{\eta},$$

and thus

$$x(y,\eta) = \frac{R_\lambda y^2}{2\displaystyle\int_0^\eta T\mathrm{d}\check{\eta}}.$$

Taking the derivative of $x(y,\eta)$ with respect to η and then using the inverse function theorem, the term $\partial\eta/\partial x|_y$ in (B.1) is calculated as

$$\left.\frac{\partial\eta}{\partial x}\right|_y = -\frac{1}{2xT}\int_0^\eta T(\check{\eta})\mathrm{d}\check{\eta}. \tag{B.2}$$

The other two terms which appear in (B.1) are:

$$\left.\frac{\partial\psi}{\partial x}\right|_\eta = \sqrt{2xR_\lambda}F(\eta), \qquad \left.\frac{\partial\psi}{\partial\eta}\right|_x = \sqrt{\frac{2x}{R_\lambda}}F'(\eta). \tag{B.3}$$

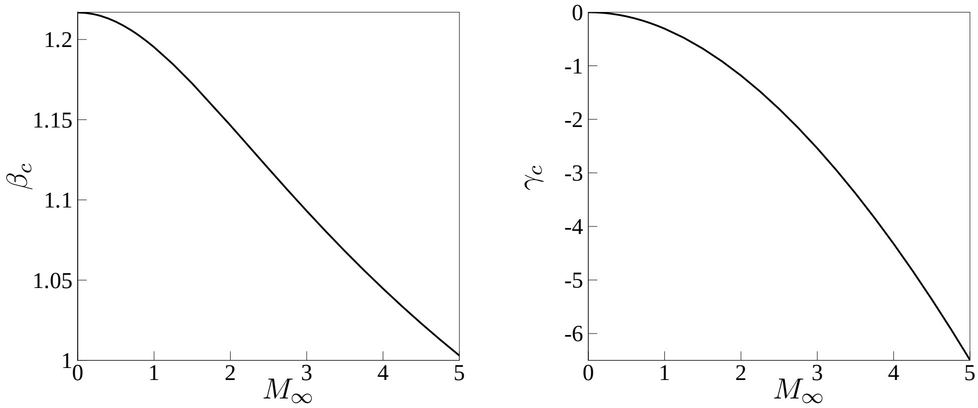

Fig. B.1: Profiles of β_c (left) and γ_c (right) as functions of Mach number.

By substitution of (B.2), (B.3) into (B.1), the Blasius wall-normal velocity component is obtained as

$$V = \sqrt{2xR_\lambda}T\left(\eta_c F' - F\right),$$

where η_c is given in §2.1.2. In the limit $\eta \to \infty$,

$$F \to \bar{\eta} \equiv \eta - \beta_c, \quad F' \to 1, \quad T \to 1, \quad \eta_c \to \eta + \gamma_c,$$

where β_c and γ_c depend on the Mach number, as shown in figure B.1. For M_∞=0, β_c corresponds to the incompressible value β=1.2168... and γ_c=0. Therefore

$$V \to \frac{\beta_c + \gamma_c}{\sqrt{2xR_\lambda}} \quad \text{as } \eta \to \infty.$$

C. INCOMPRESSIBLE LIMIT OF THE SUBSONIC INVISCID OUTER-FLOW SOLUTION

Ricco *et al.* (2011) showed that the two dimensional outer flow $\{\bar{u}_0, \bar{v}_0, \bar{p}_0\}$ is irrotational. Therefore,the stream function $\bar{\psi}_0(\bar{x}, \bar{y}, \bar{t})$ and its Fourier components $\hat{\psi}_m(\bar{x}, \bar{y})$ satisfy the Laplace equation. Taking the limit of (2.31) as $M_\infty \to 0$, the Laplace equation is obtained also for the Fourier coefficients of the potential $\hat{\phi}_m(\bar{x}, \bar{y})$:

$$\nabla^2_{\bar{x}\bar{y}} \hat{\phi}_m = 0.$$

As $M_\infty \to 0$ the boundary condition (2.29) becomes

$$\bar{v}_0(\bar{x}, 0) = \frac{k_x}{\epsilon} \frac{\partial \bar{\delta}(\bar{x}, \bar{t})}{\partial \bar{x}}, \quad \text{with } \bar{\delta}(\bar{x}, \bar{t}) = \frac{1}{\lambda_z} \int_0^{\lambda_z} \int_0^{\infty} \left[1 - u_{tot}\left(\bar{x}, y, z, \bar{t}\right)\right] \mathrm{d}y \mathrm{d}z,$$

which corresponds to (2.10) of Ricco *et al.* (2011). In terms of the Fourier coefficients, the following boundary value problems are formulated for the stream function

$$\begin{aligned} &\nabla^2_{\bar{x}\bar{y}} \hat{\psi}_m(\bar{x}, \bar{y}) = 0, && \bar{y} > 0,\ -\infty < \bar{x} < \infty, \\ &\hat{\psi}_m = \begin{cases} 0, & \bar{y} = 0,\ \bar{x} \le 0, \\ -\dfrac{k_x}{\epsilon} \hat{\delta}_m(\bar{x}), & \bar{y} = 0,\ \bar{x} > 0, \end{cases} \end{aligned}$$

and for the potential

$$\nabla^2_{\bar{x}\bar{y}} \hat{\phi}_m(\bar{x}, \bar{y}) = 0, \qquad \bar{y} > 0,\ -\infty < \bar{x} < \infty,$$

$$\frac{\partial \hat{\phi}_m}{\partial \bar{y}} = \begin{cases} 0, & \bar{y}=0,\ \bar{x}\leq 0, \\ \dfrac{k_x}{\epsilon}\hat{\delta}'_m(\bar{x}), & \bar{y}=0,\ \bar{x}>0, \end{cases}$$

The relevant solution is obtained by using complex variable theory:

$$\hat{\psi}_m(\bar{x},\bar{y}) = -\frac{k_x}{\epsilon}\Re[\hat{\delta}_m(\bar{\xi})], \quad \hat{\phi}_m(\bar{x},\bar{y}) = \frac{k_x}{\epsilon}\Im[\hat{\delta}_m(\bar{\xi})], \tag{C.1}$$

where $\hat{\delta}_m(\bar{\xi})$ is the analytic continuation of $\hat{\delta}_m(\bar{x})$ to the complex plane $\bar{\xi}=\bar{x}+i\bar{y}$.

Introducing the complex potential $W_m(\bar{\xi})=\hat{\phi}_m(\bar{\xi})+i\hat{\psi}_m(\bar{\xi})$, it follows from (C.1) that $W_m(\bar{\xi})=-i(k_x/\epsilon)\hat{\delta}_m(\bar{\xi})$. Using the relations

$$\frac{\partial \hat{\phi}_m}{\partial \bar{x}} = \frac{\partial \hat{\psi}_m}{\partial \bar{y}} = \hat{u}_m, \quad \frac{\partial \hat{\phi}_m}{\partial \bar{y}} = -\frac{\partial \hat{\psi}_m}{\partial \bar{x}} = \hat{v}_m,$$

or, analogously,

$$\frac{\mathrm{d}W_m}{\mathrm{d}\bar{\xi}} = \hat{u}_m - i\hat{v}_m = -\frac{ik_x}{\epsilon}\hat{\delta}'_m(\bar{\xi}),$$

the velocity components are obtained as

$$\{\hat{u}_m(\bar{x},\bar{y}),\hat{v}_m(\bar{x},\bar{y})\} = \frac{k_x}{\epsilon}\left\{\Im[\hat{\delta}'_m(\bar{\xi})],\Re[\hat{\delta}'_m(\bar{\xi})]\right\}.$$

The limit of (2.38) as $M_\infty\to 0$ is:

$$\begin{aligned}\lim_{M_\infty\to 0}\hat{\phi}_m(\bar{x},\bar{y}) &= -\frac{i}{2}\frac{k_x}{\epsilon}\int\limits_{\bar{x}-i\bar{y}}^{\bar{x}+i\bar{y}}\hat{\delta}'_m(\xi)\mathrm{d}\xi = -\frac{i}{2}\frac{k_x}{\epsilon}\left[\hat{\delta}_m(\bar{x}+i\bar{y})-\hat{\delta}_m(\bar{x}-i\bar{y})\right] \\ &= \frac{k_x}{\epsilon}\Im[\hat{\delta}_m(\bar{\xi})],\end{aligned}$$

where the property of holomorphic function $\hat{\delta}_m(\bar{\xi}^\star)=\hat{\delta}_m(\bar{\xi})^\star$ has been employed.

D. UPSTREAM LIMITS OF THE LARGE-η ASYMPTOTIC SOLUTION AND THE OUTER DIRICHLET BOUNDARY CONDITION

The following analysis shows that the approaches employed by Leib *et al.* (1999) and Ricco *et al.* (2011) to find the outer boundary conditions are consistent. First consider equation (5.22) in Leib *et al.* (1999), which represents the large-η asymptotic solution of the spanwise velocity that matches with the outer solution:

$$\bar{w} = \frac{e^{i\bar{x}}}{\kappa_y - i|\kappa|} \left\{ \kappa_y e^{i\kappa_y y^{(0)} - \left(\kappa^2 + \kappa_y^2\right)\bar{x}} - i|\kappa| e^{-|\kappa| y^{(0)}} \right\} + \kappa^2 e^{i\bar{x} - |\kappa| y^{(0)}} \int_0^{\bar{x}} g(\check{x}) e^{-i\check{x}} d\check{x}, \tag{D.1}$$

where the function $g(\check{x})$ is unknown and $y^{(0)} {\equiv} \sqrt{2\bar{x}}(\eta - \beta) {=} y\sqrt{k_x R_\lambda} - \beta\sqrt{2\bar{x}}$. The limit of (D.1) as $\bar{x} \to 0$ with $y {=} \mathcal{O}(1)$ is calculated as:

$$\lim_{\bar{x} \to 0} \bar{w} = \frac{\kappa_y e^{ik_y y} - i|\kappa| e^{-|k_z| y}}{\kappa_y - i|\kappa|}, \tag{D.2}$$

which, in the large-y limit, becomes

$$\lim_{y \to \infty} \bar{w}_{|\bar{x} \to 0} = \frac{\kappa_y e^{ik_y y}}{\kappa_y - i|\kappa|}. \tag{D.3}$$

The physical spanwise velocity is defined in Leib *et al.* (1999) as:

$$w = \epsilon \left(\hat{u}_z^\infty + \frac{ik_z}{\gamma} \hat{u}_y^\infty \right) \bar{w} e^{i(k_z z - k_x t)}, \tag{D.4}$$

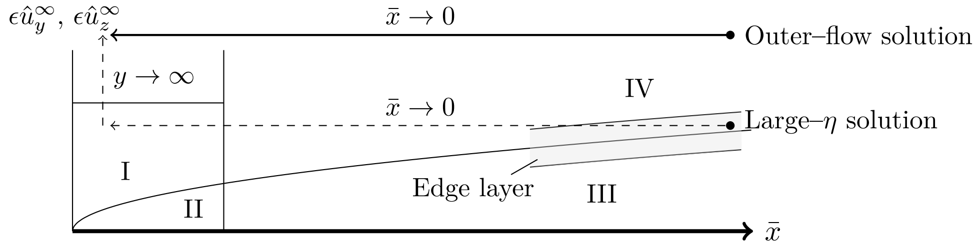

Fig. D.1: Schematic of the analysis carried out to show the consistency between the approaches of Leib *et al.* (1999) and Ricco *et al.* (2011). The tick arrow represents the upstream limit of the outer-flow solution of Ricco *et al.* (2011), while the dashed arrows denote the upstream and large-y limits of the edge boundary condition of Leib *et al.* (1999). The shaded area indicates the so-called 'edge layer' where $\eta \gg 1$ and $y = \mathcal{O}(1)$ (Leib *et al.*, 1999; Goldstein, 2014).

where $\gamma = \sqrt{k_x^2 + k_z^2}$. Therefore, by inserting (D.3) in (D.4), the following relation is obtained:

$$w \to \epsilon \left(\hat{u}_z^\infty + i\hat{u}_y^\infty \right) \frac{\kappa_y e^{ik_y y}}{\kappa_y - i|\kappa|} e^{i(k_z z - k_x t)}, \quad \text{as } \bar{x} \to 0 \text{ and } y^{(0)} \to \infty, \tag{D.5}$$

where γ has been approximated with $k_z > 0$ because $k_x \ll k_z$. By dropping out the term $k_x \hat{u}_x^\infty \ll k_y \hat{u}_y^\infty, k_z \hat{u}_z^\infty$ in the free-stream continuity equation (refer to (2.4) in Leib *et al.* (1999)) and dividing everything by $\sqrt{k_x R_\lambda}$, the following expression is obtained:

$$\hat{u}_y^\infty = -\frac{\kappa}{\kappa_y} \hat{u}_z^\infty. \tag{D.6}$$

Inserting (D.6) in (D.5), it follows that the amplitude of the spanwise velocity tends to $\epsilon \hat{u}_z^\infty$ as $\bar{x} \to 0$ and $y \to \infty$.

The same value is obtained by taking the limit $\bar{x} \to 0$ of $\hat{w}_0$ given in equation (2.24) of Ricco *et al.* (2011), and multiplying by ϵ to obtain the physical quantity and by $\hat{u}_z^\infty$ to match the amplitude of the upstream incoming disturbance. The constant $c_\infty = 1/k_y$ was chosen so that $|\hat{w}_0| = 1$. A schematic of the limits that have been taken to show the consistency between the approaches of Leib *et al.* (1999) and Ricco *et al.* (2011) is illustrated in figure D.1.

The same procedure applies to the wall-normal velocity component. By taking the limits $\bar{x}\to 0$ and $y\to\infty$ of the large-η asymptotic solution of $\bar{v}$ (refer to (5.21) in Leib *et al.* (1999)) and using the continuity equation, it follows that the physical amplitude $|v|\to -\epsilon\kappa/\kappa_y\hat{u}_z^{\infty}$, which corresponds to $\epsilon\hat{u}_y^{\infty}$, according to (D.6). In Ricco *et al.* (2011) the limit $\bar{x}\to 0$ of $\hat{v}_0$ given in equation (2.24) leads to $-k_z/k_y$, which is then multiplied by ϵ and $\hat{u}_z^{\infty}$, thus giving the same result as Leib *et al.* (1999).

E. VALIDATION OF THE GÖRTLER-FLOW SOLVER IN THE LINEARIZED CASE

As a validation of our code, we have checked that the solution obtained with the nonlinear boundary-region solver for r_t=0 matches that of Wu *et al.* (2011). The parameters correspond to case 1 in table 3.1 ($\mathcal{G}$=14.7). The comparison is carried out by calculating the downstream development of the maximum streamwise velocity fluctuation $|\bar{u}|_{max}$=$C^{-1}\max_\eta|\hat{u}_{-1,1}|$, where the coefficient C=$|k_z(\hat{u}_z^\infty + ik_z\hat{u}_y^\infty/|k_z|)|$=$\sqrt{2}$ takes into account the different formulation of Wu *et al.* (2011) (refer to their equations (2.13)-(2.14) and to our (3.5)). Figure E.1 shows the excellent agreement between the results of Wu *et al.* (2011) and ours.

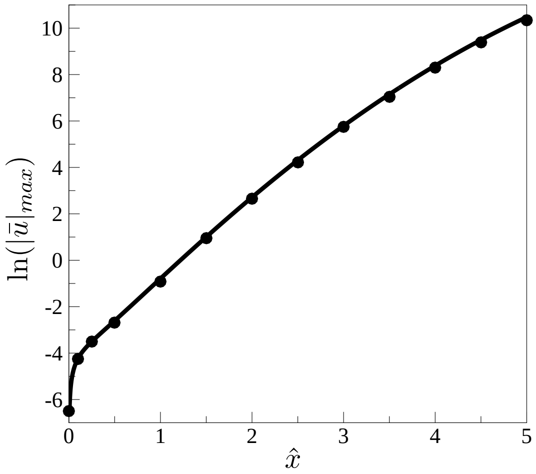

Fig. E.1: Validation of the linearized solution (solid line) against numerical data of Wu *et al.* (2011) (filled circles) for $\mathcal{G}$=14.7.

BIBLIOGRAPHY

Abramowitz, M., Stegun, I., 1964. Handbook of Mathematical Functions. Nat. Bureau Stand. Appl. Math. Ser. 55.

Aihara, Y., 1962. Transition in an incompressible boundary layer along a concave wall. Bull. Aerospace Res. Inst. Univ. Tokyo 3, 195–240.

Anderson, J. J., 2006. Hypersonic and high-temperature gas dynamics, 2nd Edition. AIAA.

Anderson, J. J., 2007. Fundamentals of aerodynamics, 4th Edition. McGraw Hill.

Andersson, P., Berggren, M., Henningson, D., 1999. Optimal disturbances and bypass transition in boundary layers. Phys. Fluids 11 (1), 134–150.

Arnal, D., Juillen, J., 1978. Contribution expérimentale à l'étude de la reptivité d'une couche limite laminaire à la turbulence de l'écoulement général. CERT RT 1/5018 AYD - ONERA.

Asai, M., Minagawa, M., Nishioka, M., 2002. The instability and breakdown of a near-wall low-speed streak. J. Fluid Mech. 455, 289–314.

Bassom, A., Hall, P., 1994. The receptivity problem for $\mathcal{O}(1)$ wavelength Görtler vortices. Proc. R. Soc. Lond. A 446 (1928), 499–516.

Bassom, A., Seddougui, S., 1995. Receptivity mechanisms for Görtler vortex modes. Theor. Comp. Fluid Dyn. 7 (5), 317–339.

Beckwith, I., Miller III, C., 1990. Aerothermodynamics and transition in high-speed wind tunnels at NASA Langley. Ann. Rev. Fluid Mech. 22, 419–439.

Benmalek, A., Saric, W., 1994. Effects of curvature variations on the nonlinear evolution of Görtler vortices. Phys. Fluids 6 (10), 3353–3367.

Bertolotti, F., 1993. Vortex generation and wave-vortex interaction over a concave plate with roughness and suction. ICASE, 93–101.

Bertolotti, F., 1997. Response of the Blasius boundary layer to free-stream vorticity. Phys. Fluids 9 (8), 2286–2299.

Bippes, H., 1972. Experimentelle untersuchung des laminar-turbulenten umschlags an einer parallel angestroemten konkaven wand. Sitzungsberichte der Heidelberger Akademie der Wissenschaften Mathematischnaturwissenschaftliche Klasse, 103-180, Jahrgang 1972, 3 Abhand-lung (also NASA-TM-72243, 1978).

Bippes, H., Görtler, H., 1972. Dreidimensionale störungen in der grenzschicht an einer konkaven wand. Acta Mech. 14 (4), 251–267.

Boiko, A., Ivanov, A., Kachanov, Y., Mischenko, D., 2010a. Investigation of weakly-nonlinear development of unsteady Görtler vortices. Thermophys. Aeromech. 17 (4), 455–481.

Boiko, A., Ivanov, A., Kachanov, Y., Mischenko, D., 2010b. Steady and unsteady Görtler boundary-layer instability on concave wall. Europ. J. Mech. B/Fluids 29 (2), 61–83.

Bottaro, A., Luchini, P., 1999. Görtler vortices: Are they amenable to local eigenvalue analysis? Europ. J. Mech. B/Fluids 18 (1), 47–65.

Brandt, L., Schlatter, P., Henningson, D., 2004. Transition in boundary layers subject to free-stream turbulence. J. Fluid Mech. 517, 167–198.

Brinkerhoff, J., Yaras, M., 2015. Numerical investigation of transition in a boundary layer subjected to favourable and adverse streamwise pressure gradients and elevated free stream turbulence. J. Fluid Mech. 781, 52–86.

Brown, A., Martin, B., 1982. Flow transition phenomena and heat transfer over the pressure surfaces of gas turbine blades. J. Eng. Power Trans. ASME 104 (2), 360–367.

Camci, C., Arts, T., 1990. An Experimental Convective Heat Transfer Investigation Around a Film-Cooled Gas Turbine Blade. J. Turbom. 112 (3), 497–503.

Canuto, C., Hussaini, M., Quarteroni, A., Zang, T., 1988. Spectral Methods in Fluid Dynamics. Springer-Verlag, New York.

Cebeci, T., 2002. Convective Heat Transfer. Springer-Verlag.

Champion, K. W., Cole, A., Kantor, A., 1985. Standard and Reference Atmospheres. Handbook of Geophysics and the Space Environment 14.

Chang, C.-L., Malik, M., 1994. Oblique-mode breakdown and secondary instability in supersonic boundary layers. J. Fluid Mech. 273, 323–360.

Chang, C.-L., Malik, M., Erlebacher, M., M.Y., H., 1991. Compressible stability of growing boundary layers using parabolized stability equations. AIAA Paper 1636.

Chang, C.-L., Malik, M., Hussaini, M., 1990. Effects of shock on the stability of hypersonic boundary layers. AIAA Paper 1448.

Choudhari, M., 1996. Boundary layer receptivity to three-dimensional unsteady vortical disturbances in the free stream. AIAA Paper 0181.

Choudhari, M., Streett, C. L., 1990. Boundary layer receptivity phenomena in three-dimensional and high-speed boundary layers. AIAA Paper 5258.

Coleman, T., Steiner, R., 1960. Atmospheric turbulence measurements obtained from airplane operations at altitudes between 20,000 and 75,000 feet for several areas in the northern hemisphere. Tech. Rep. NASA/TN D-548, NASA.

Cossu, C., Chomaz, J.-M., Huerre, P., Costa, M., 2000. Maximum spatial growth of Görtler vortices. Flow, Turb. and Comb. 65 (3-4), 369–392.

Cowley, S., Hall, P., 1990. On the instability of hypersonic flow past a wedge. J. Fluid Mech. 214, 17–42.

Day, H., Herbert, T., Saric, W., 1990. Comparing local and marching analyses of Görtler instability. AIAA J. 28 (6), 1010–1015.

Demetriades, A., 1989. Growth of disturbances in a laminar boundary layer at Mach 3. Phys. Fluids A 1 (2), 312–317.

Denier, J., Hall, P., Seddougui, S., 1991. On the receptivity problem for Görtler vortices: vortex motions induced by wall roughness. Phil. Trans. R. Soc. Lond. A 335 (1636), 51–85.

Diprima, R., Stuart, J., 1972. Non-local effects in the stability of flow between eccentric rotating cylinders. J. Fluid Mech. 54 (3), 393–415.

Dong, M., Wu, X., 2013. On continuous spectra of the Orr-Sommerfeld/Squire equations and entrainment of free-stream vortical disturbances. J. Fluid Mech. 732, 616–659.

Dongarra, J., Lumsdaine, A., Pozo, R., Remington, K., 2006. IML++ v. 1.2 Iterative Method Library. "`http://http://math.nist.gov/iml++/`".

Dowell, E., 2014. A modern course in aeroelasticity. Vol. 217. Springer.

Dragos, L., 2004. Mathematical methods in aerodynamics. Springer Science & Business Media.

Dryden, H., 1955. Transition from laminar to turbulent flow at subsonic and supersonic speeds. Conference on High-Speed Aeronautics, 41, Polytechnic of Brooklyn, New York.

Ehernberger, L., Love, B., 1975. High altitude gust acceleration environment as experienced by a supersonic airplane. Tech. Rep. NASA/TN D-7868, NASA.

Fasel, H., 2002. Numerical investigation of the interaction of the Klebanoff-mode with a Tollmien-Schlichting wave. J. Fluid Mech. 450, 1–33.

Fedorov, A., Khokhlov, A., 2001. Prehistory of instability in a hypersonic boundary layer. Theor. Comp. Fluid Dyn. 14, 359–375.

Fedorov, A., Khokhlov, A., 2003. Receptivity of a high-speed boundary layer to acoustic disturbances. J. Fluid Mech. 491, 101–129.

Fedorov, A., Shiplyuk, A., Maslov, A., Burov, E., Malmuth, N., 2003. Stabilization of a hypersonic boundary layer using an ultrasonically absorptive coating. J. Fluid Mech. 479, 99–124.

Finnis, M., Brown, A., 1989. Stability of a laminar boundary layer flowing along a concave surface. J. Turbomach. 111 (4), 376–386.

Finnis, M., Brown, A., 1997. The linear growth of Görtler vortices. Int. J. Heat Fluid Flow 18 (4), 389–399.

Floryan, J., 1991. On the Görtler instability of boundary layers. Prog. Aerosp. Sci. 28 (3), 235–271.

Floryan, J., Saric, W., 1982. Stability of Görtler vortices in boundary layers. AIAA J. 20 (3), 316–324.

Fransson, J., Matsubara, M., Alfredsson, P., 2005. Transition induced by free-stream turbulence. J. Fluid Mech. 527, 1–25.

Girgis, I., Liu, J., 2006. Nonlinear mechanics of wavy instability of steady longitudinal vortices and its effect on skin friction rise in boundary layer flow. Phys. Fluids 18, 024102.

Goldstein, M., 1997. Response of the pre-transitional laminar boundary layer to free-stream turbulence - Otto Laporte Lecture. Bull. Am. Phys. Soc. 42, 2150.

Goldstein, M., 2014. Effect of free-stream turbulence on boundary layer transition. Phil. Trans. Royal Soc. 372 (2020), 20130354.

Goldstein, M., Leib, S., 1993. Three-dimensional boundary layer instability and separation induced by small-amplitude streamwise vorticity in the upstream flow. J. Fluid Mech. 246, 21–41.

Goldstein, M., Leib, S., Cowley, S., 1992. Distortion of a flat plate boundary layer by free stream vorticity normal to the plate. J. Fluid Mech. 237, 231–260.

Goldstein, M., Sescu, A., 2008. Boundary-layer transition at high free-stream disturbance levels - beyond Klebanoff modes. J. Fluid Mech. 613, 95 – 124.

Görtler, H., 1940. Uber eine dreidimensionale instabilitat laminarer grenzschichten an konkaven wanden. Ges. d. Wiss. Gottingen, Nachr. ad Math 2 (1).

Graziosi, P., Brown, G., 2002. Experiments on stability and transition at Mach 3. J. Fluid Mech. 472, 83–124.

Gulyaev, A., Kozlov, V., Kuzenetsov, V., Mineev, B., Sekundov, A., 1989. Interaction of a laminar boundary layer with external turbulence. Fluid Dynamics.

Translated from Izv, Akad. Navk. SSSR Mekh. Zhid. Gaza 6, vol. 5, pp. 55-65. 24 (5), 700–710.

Gustavsson, L., 1991. Energy growth of three-dimensional disturbances in plane Poiseuille flow. J. Fluid Mech. 224, 241.

Hall, P., 1982a. On the non-linear evolution of Görtler vortices in non-parallel boundary layers. IMA J. Appl. Math. 29 (2), 173–196.

Hall, P., 1982b. Taylor-Görtler vortices in fully developed or boundary-layer flows: linear theory. J. Fluid Mech. 124, 475–494.

Hall, P., 1983. The linear development of Görtler vortices in growing boundary layers. J. Fluid Mech. 130, 41–58.

Hall, P., 1988. The nonlinear development of Görtler vortices in growing boundary layers. J. Fluid Mech. 193, 243–266.

Hall, P., 1990. Görtler vortices in growing boundary layers: the leading edge receptivity problem, linear growth and the nonlinear breakdown stage. Mathematika 37 (74), 151–189.

Hall, P., Horseman, N. J., 1991. The linear inviscid secondary instability of longitudinal vortex structures in boundary layers. J. Fluid Mech. 232, 357–375.

Hämmerlin, G., 1956. Zur theorie der dreidimensionalen instabilität laminarer grenzschichten. Z. Angew. Math. Phys. 7 (2), 156–164.

Herbert, T., 1976. On the stability of the boundary layer along a concave wall. Arch. Mech. Stosowanej 28, 1039–1055.

Hocking, W., 1985. Measurement of turbulent energy dissipation rates in the middle atmosphere by radar techniques: A review. Radio Science 20 (6), 1403–1422.

Ivanov, A., Kachanov, Y., Mischenko, D., 2011. On excitation of Görtler vortices due to scattering of free-stream vortices on surface non-uniformities. In: J. Phys.: Conf. Series. Vol. 318. IOP Publishing, p. 032029.

Ivanov, A., Kachanov, Y., Mischenko, D., 2012. Generation of nonstationary Görtler vortices by localized surface nonuniformities. Receptivity coefficients. Thermophys. Aeromech. 19 (4), 523–539.

Ivanov, A., Kachanov, Y., Mischenko, D., 2014. Mechanisms of distributed and localized excitation of unsteady Görtler modes by free-stream vortices. Thermophys. Aeromech. 21 (6), 663–678.

Jacobs, R., Durbin, P., 2001. Simulation of bypass transition. J. Fluid Mech. 428, 185–212.

Joo, J., Durbin, P., 2012. Continuous mode transition in high-speed boundary-layers. Flow Turb. Comb. 88, 407–430.

Kalburgi, V., Mangalam, S., Dagenhart, J., 1988. A comparative study of theoretical methods on Görtler instability. AIAA Paper 0407.

Kemp, N., 1951. The laminar three-dimensional boundary layer and a study of the flow past a side edge. Ph.D. thesis, MSc Thesis, Cornell University.

Kendall, J., 1967. Supersonic boundary layer stability experiments. Tech. rep., Air force report BSD-TR-67-213, Vol. II.

Kendall, J., 1975. Wind tunnel experiments relating to supersonic and hypersonic boundary-layer transition. AIAA J. 13 (3), 290–299.

Kendall, J., 1985. Experimental study of disturbances produced in a pre-transitional laminar boundary layer by weak freestream turbulence. AIAA Paper 1695.

Kestoras, M., Simon, T., 1993. Effects of free-stream turbulence intensity on a boundary layer recovering from concave curvature effects. In: ASME 1993 International Gas Turbine and Aeroengine Congress and Exposition. American Society of Mechanical Engineers, pp. V002T08A001–V002T08A001.

Kim, J., Simon, T., Russ, S., 1992. Free-stream turbulence and concave curvature effects on heated, transitional boundary layers. J. Heat Transf. 114 (2), 338–347.

Klebanoff, P., 1971. Effect of free-stream turbulence on a laminar boundary layer. Bull. Am. Phys. Soc. 16, 1323.

Kottke, V., 1988. On the instability of laminar boundary layers along concave walls towards Görtler vortices. In: Propagation in Systems Far from Equilibrium. Springer, pp. 390–398.

Kottke, V., Mpourdis, B., 1987. On the existence of Taylor-Görtler vortices on concave walls. In: Flow Visualization IV. Vol. 1. pp. 475–480.

Lam, S. H., Rott, N., 1960. Theory of linearized time-dependent boundary layers. Cornell University Grad. School of Aero. Engineering Dept. - AFOSR TN-60-1100.

Landahl, M., 1980. A note on an algebraic instability of inviscid parallel shear flows. J. Fluid Mech. 98, 243–251.

Landahl, M., 1989. Unsteady transonic flow. Cambridge Univ. Press.

Laufer, J., 1954. Factors affecting transition Reynolds numbers on models in supersonic wind tunnels. J. Aero. Sc. 21, 497–498.

Laufer, J., 1961. Aerodynamic noise in supersonic wind tunnels. J. Aero. Sc. 28 (9), 685–692.

Lees, L., 1947. The stability of the laminar boundary layer in a compressible fluid. NACA TN 876.

Leib, S., Wundrow, D., Goldstein, M., 1999. Effect of free-stream turbulence and other vortical disturbances on a laminar boundary layer. J. Fluid Mech. 380, 169–203.

Leoutsakos, G., Crane, R., 1990. Three-dimensional boundary layer transition on a concave surface. Int. J. Heat Fluid Flow 11 (1), 2–9.

Li, F., Malik, M., 1995. Fundamental and subharmonic secondary instabilities of Görtler vortices. J. Fluid Mech. 297, 77–100.

Li, F., Malik, M., 1996. On the nature of pse approximation. Theor. Comp. Fluid Dyn. 8 (4), 253–273.

Liepmann, H., 1945. Investigation of boundary layer transition on concave walls. NACA Wartime Rep. W87.

Lighthill, M., 1958. On displacement thickness. J. Fluid Mech. 4 (04), 383–392.

Liu, W., Domaradzki, J., 1993. Direct numerical simulation of transition to turbulence in Görtler flow. J. Fluid Mech. 246, 267–299.

Luchini, P., 2000. Reynolds-number-independent instability of the boundary layer over a flat surface: optimal perturbations. J. Fluid Mech. 404, 289–309.

Luchini, P., Bottaro, A., 1998. Gortler vortices: a backward-in-time approach to the receptivity problem. J. Fluid Mech. 363, 1–23.

Mack, L., 1975. Linear stability theory and the problem of supersonic boundary-layer transition. AIAA J. 13 (3), 278–289.

Mack, L., 1984. Boundary-layer linear stability theory. Special Course on Stability and Transition of Laminar flow. AGARD Report 709, 1–81.

Mandal, A., Venkatakrishnan, L., Dey, J., 2010. A study on boundary-layer transition induced by free-stream turbulence. J. Fluid Mech. 660, 114–146.

Mangalam, S., Dagenhart, J., Hepner, T., Meyers, J., 1985. The Görtler instability on an airfoil. AIAA Paper 0491.

Matsubara, M., Alfredsson, P., 2001. Disturbance growth in boundary layers subjected to free-stream turbulence. J. Fluid Mech. 430, 149–168.

Mayer, C., Von Terzi, D., Fasel, H., 2011. Direct numerical simulation of complete transition to turbulence via oblique breakdown at Mach 3. J. Fluid Mech. 674, 5–42.

McKenzie, J., Westphal, K., 1968. Interaction of linear waves with oblique shock waves. Phys. Fluids 11 (11), 2350–2362.

Morkovin, M., 1984. Bypass transition to turbulence and research desiderata. In: Transition in Turbines Symposium. NASA CP-2386.

Nagarajan, S., Lele, S. K., Ferziger, J., 2007. Leading-edge effects in bypass transition. J. Fluid Mech. 572, 471–504.

Ovchinnikov, V., Choudhari, M., Piomelli, U., 2008. Numerical simulations of boundary-layer bypass transition due to high-amplitude free-stream turbulence. J. Fluid Mech. 613, 135–169.

Pate, S., Schueler, C., 1969. Radiated aerodynamic noise effects on boundary-layer transition in supersonic and hypersonic wind tunnels. AIAA J. 7 (3), 450–457.

Qin, F., Wu, X., 2016. Response and receptivity of the hypersonic boundary layer past a wedge to free-stream acoustic, vortical and entropy disturbances. J. Fluid Mech. 797, 874–915.

Ragab, S., Nayfeh, A., 1981. Görtler instability. Phys. Fluids 24 (8), 1405–1417.

Rai, M., Moin, P., 1993. Direct numerical simulation of transition and turbulence in a spatially evolving boundary layer. J. Comp. Phys. 109 (2), 169–192.

Reed, H. L., Reshotko, E., Saric, W. S., 2015. Receptivity: The inspiration of Mark Morkovin. In: 45th AIAA Fluid Dynamics Conference. Vol. 2471.

Ricco, P., 2006. Response of a compressible laminar boundary layer to free-stream turbulence. PhD Thesis, University of London.

Ricco, P., 2009. The pre-transitional Klebanoff modes and other boundary layer disturbances induced by small-wavelength free-stream vorticity. J. Fluid Mech. 638, 267–303.

Ricco, P., Luo, J., Wu, X., 2011. Evolution and instability of unsteady nonlinear streaks generated by free-stream vortical disturbances. J. Fluid Mech. 677, 1–38.

Ricco, P., Shah, D., Hicks, P., 2013. Compressible laminar streaks with wall suction. Phys. Fluids 25 (5), 054110.

Ricco, P., Tran, D.-L., Ye, G., 2009. Wall heat transfer effects on Klebanoff modes and Tollmien-Schlichting waves in a compressible boundary layer. Phys. Fluids 21 (2), 024106.

Ricco, P., Walsh, E., Brighenti, F., McEligot, D., 2016. Growth of boundar-layer streaks due to free-stream turbulence. To appear in Int. J. Heat Fluid Flow.

Ricco, P., Wu, X., 2007. Response of a compressible laminar boundary layer to free-stream vortical disturbances. J. Fluid Mech. 587, 97–138.

Riedel, H., Sitzmann, M., 1998. In-flight investigations of atmospheric turbulence. Aero. Sc. Technol. 2 (5), 301–319.

Riley, S., Johnson, M. W., Gibbings, J., 1989. Boundary layer transition of strongly concave surfaces. In: ASME 1989 International Gas Turbine and Aeroengine Congress and Exposition. American Society of Mechanical Engineers, pp. V001T01A112–V001T01A112.

Saad, Y., Schultz, M., 1986. GMRES: A generalized minimal residual algorithm for solving nonsymmetric linear systems. SIAM J. Scient. Statist. Comput. 7 (3), 856–869.

Saric, W., 1994. Görtler vortices. Annu. Rev. Fluid Mech. 26 (1), 379–409.

Saric, W. S., 2008. Flight experiments on local and global effects of surface roughness on 2-D and 3-D boundary-layer stability and transition. Tech. rep., DTIC Document.

Schlichting, H., Gersten, K., 2000. Boundary-Layer Theory. Springer.

Schneider, S., 1999. Flight data for boundary-layer transition at hypersonic and supersonic speeds. J. Spacecr. Rockets 36 (1), 8–20.

Schneider, S., 2001. Effect of high-speed tunnel noise on laminar-turbulent transition. J. Spacecr. Rockets 38-3, 323–333.

Schrader, L.-U., Brandt, L., Zaki, T., 2011. Receptivity, instability and breakdown of Görtler flow. J. Fluid Mech. 682, 362–396.

Schultz, M., Volino, R., 2003. Effects of concave curvature on boundary layer transition under high freestream turbulence conditions. J. Fluids Eng. 125 (1), 18–27.

Sescu, A., Yassir, S., Visbal, M., 2016. Compressible boundary layer receptivity to free-stream disturbances and step excrescences. In: 46th AIAA Fluid Dynamics Conference. pp. 1–23.

Smith, A., 1955. On the growth of Taylor-Görtler vortices along highly concave walls. Quart. J. Math. 13 (3), 233–262.

Stainback, P., 1971. Hypersonic boundary-layer transition in the presence of wind tunnel noise. AIAA J. 9, 2475–2476.

Stewartson, K., 1950. On the linearized potential theory of unsteady supersonic motion. Quart. J. Mech. Appl. Math. 3 (2), 182–199.

Stewartson, K., 1964. The theory of laminar boundary layers in compressible fluids. Oxford, Claredon Press.

Swearingen, J., Blackwelder, R., 1983. Parameters controlling the spacing of streamwise vortices on concave walls. AIAA Paper 0380.

Swearingen, J., Blackwelder, R., 1987. The growth and breakdown of streamwise vortices in the presence of a wall. J. Fluid Mech. 182, 255–290.

Tandiono, T., Winoto, S., Shah, D., 2008. On the linear and nonlinear development of Görtler vortices. Phys. Fluids 20 (9), 094103.

Tandiono, T., Winoto, S., Shah, D., 2013. Spanwise velocity component in nonlinear region of Görtler vortices. Phys. Fluids 25 (10), 104104.

Tani, I., 1962. Production of longitudinal vortices in the boundary layer along a concave wall. J. Geophys. Res. 67 (8), 3075–3080.

Tani, I., Aihara, Y., 1969. Görtler vortices and boundary-layer transition. Z. Angew. Math. Phys. 20 (5), 609–618.

Tani, I., Sakagami, J., 1962. Boundary-layer instability at subsonic speeds. In: Proc. ICAS, Third Congress, Stockholm. pp. 391–403.

Taylor, G., 1939. Some recent developments in the study of turbulence. Fifth Intl. Congr. for Appl. Mech., 294–310.

Timoshin, S., 1990. Asymptotic analysis of a spatially unstable Görtler vortex spectrum. Fluid Dynamics. Translated from Izv, Akad. Nauk. SSSR, Mekh. Zhid. i Gaza, No. 1, pp. 32-41 25 (1), 25–33.

Tsuji, Y., Fransson, J., Alfredsson, P., Johansson, A., 2007. Pressure statistics and their scaling in high-Reynolds-number turbulent boundary layers. J. Fluid Mech. 585, 1–40.

Van Dyke, M., 1975. Perturbation Methods in Fluid Mechanics. The Parabolic Press - Stanford, California.

Volino, R., Simon, T., 1995. Bypass transition in boundary layers including curvature and favorable pressure gradient effects. J. Turbomach. 117 (1), 166–174.

Volino, R., Simon, T., 1996. Measurements in a transitional boundary layer with Görtler vortices. In: ASME 1996 International Gas Turbine and Aeroengine Congress and Exhibition. American Society of Mechanical Engineers, pp. V001T01A058–V001T01A058.

Volino, R., Simon, T., 2000. Spectral measurements in transitional boundary layers on a concave wall under high and low free-stream turbulence conditions. J. Turbomach. 122, 450–457.

Westin, K., Bakchinov, A., Kozlov, V., Alfredsson, P., 1998. Experiments on localized disturbances in a flat plate boundary layer. Part 1. The receptivity and the evolution of a localized free-stream disturbance. Europ. J. Mech. B/Fluids 17, 823–846.

Westin, K., Boiko, A., Klingmann, B., Kozlov, V., Alfredsson, P., 1994. Experiments in a boundary layer subjected to free stream turbulence. Part 1. Boundary layer structure and receptivity. J. Fluid Mech. 281, 193–218.

Wilson, R., Love, B., Larson, R., 1971. Evaluation of effects of high-altitude turbulence encounters on the XB-70 airplane. Tech. Rep. NASA/TN D-6457, NASA.

Winoto, S., Crane, R., 1980. Vortex structure in laminar boundary layers on a concave wall. Int. J. Heat Fluid Flow 2 (4), 221–231.

Wortmann, F., 1964. Experimental investigations of vortex occurrence at transition in unstable laminar boundary. Tech. rep., DTIC Document.

Wortmann, F., 1969. Visualization of transition. J. Fluid Mech. 38 (3), 473–480.

Wu, X., Choudhari, M., 2003. Linear and non-linear instabilities of a Blasius boundary layer perturbed by streamwise vortices. Part 2. Intermittent instability induced by long-wavelength Klebanoff modes. J. Fluid Mech. 483, 249–286.

Wu, X., Dong, M., 2016. Entrainment of short-wavelength free-stream vortical disturbances in compressible and incompressible boundary layers. J. Fluid Mech. 797, 683–728.

Wu, X., Jacobs, R., Hunt, J., Durbin, P., 1999. Simulation of boundary layer transition induced by periodically passing wakes. J. Fluid Mech. 398, 109–153.

Wu, X., Luo, J., 2003. Linear and non-linear instabilities of a Blasius boundary layer perturbed by streamwise vortices. Part 1. Steady streaks. J. Fluid Mech. 483, 225–248.

Wu, X., Zhao, D., Luo, J., 2011. Excitation of steady and unsteady Görtler vortices by free-stream vortical disturbances. J. Fluid Mech. 682, 66–100.

Wundrow, D., Goldstein, M., 2001. Effect on a laminar boundary layer of small-amplitude streamwise vorticity in the upstream flow. J. Fluid Mech. 426, 229–262.

Yu, X., Liu, J., 1994. On the mechanism of sinuous and varicose modes in three-dimensional viscous secondary instability of nonlinear Görtler rolls. Phys. Fluids 6 (2), 736–750.

Zaki, T., Durbin, P., 2005. Mode interaction and the bypass route to transition. J. Fluid Mech. 531, 85–111.

Zanin, B., 1985. Transition at natural conditions and comparison with the results of wind tunnel studies. In: Laminar-Turbulent Transition. Springer, pp. 541–546.

Zhang, Q., He, L., 2014. Impact of wall temperature on turbine blade tip aerothermal performance. J. Eng. Gas Turb. Power 136 (5), 052602.

Zhang, Y., Zaki, T., Sherwin, S., Wu, X., 2011. Nonlinear response of a laminar boundary layer to isotropic and spanwise localized free-stream turbulence. In: The 6th AIAA Theoretical Fluid Mechanics Conference. Vol. 3292.

Zhong, X., Wang, X., 2012. Direct numerical simulation on the receptivity, instability, and transition of hypersonic boundary layers. Ann. Rev. Fluid Mech. 44, 527–561.

Zuccher, S., Bottaro, A., Luchini, P., 2006. Algebraic growth in a Blasius boundary layer: Nonlinear optimal disturbances. Europ. J. Mech. - B/Fluids 25 (1), 1–17.